

SIGNATURES OF PLANETS IN CIRCUMSTELLAR DEBRIS DISKS

by

María Amaya Moro-Martín

A Dissertation Submitted to the Faculty of the
DEPARTMENT OF ASTRONOMY
In Partial Fulfillment of the Requirements
For the Degree of
DOCTOR OF PHILOSOPHY
In the Graduate College
THE UNIVERSITY OF ARIZONA

2004

UMI Number: 3145104

INFORMATION TO USERS

The quality of this reproduction is dependent upon the quality of the copy submitted. Broken or indistinct print, colored or poor quality illustrations and photographs, print bleed-through, substandard margins, and improper alignment can adversely affect reproduction.

In the unlikely event that the author did not send a complete manuscript and there are missing pages, these will be noted. Also, if unauthorized copyright material had to be removed, a note will indicate the deletion.

UMI[®]

UMI Microform 3145104

Copyright 2004 by ProQuest Information and Learning Company.

All rights reserved. This microform edition is protected against unauthorized copying under Title 17, United States Code.

ProQuest Information and Learning Company
300 North Zeeb Road
P.O. Box 1346
Ann Arbor, MI 48106-1346

The University of Arizona ®
Graduate College

As members of the Final Examination Committee, we certify that we have read the

dissertation prepared by Maria Amaya Moro-Martin

entitled Signatures of Planets in Circumstellar Debris Disks

and recommend that it be accepted as fulfilling the dissertation requirement for the

Degree of Doctor of Philosophy

Renu Malhotra

Renu Malhotra

4/27/04
date

Michael R. Meyer

Michael R. Meyer

4-29-04
date

George Rieke

George Rieke

date

Jonathan I. Lunine

Jonathan I. Lunine

date

Mark Vicent Sykes

Mark Vicent Sykes

4/29/04

date

4/29/04
date

Final approval and acceptance of this dissertation is contingent upon the candidate's submission of the final copies of the dissertation to the Graduate College.

I hereby certify that I have read this dissertation prepared under my direction and recommend that it be accepted as fulfilling the dissertation requirement.

Renu Malhotra

Dissertation Director:

Renu Malhotra

Michael R. Meyer 4-29-04

Michael R. Meyer

date

STATEMENT BY AUTHOR

This dissertation has been submitted in partial fulfillment of requirements for an advanced degree at The University of Arizona and is deposited in the University Library to be made available to borrowers under rules of the library.

Brief quotations from this dissertation are allowable without special permission, provided that accurate acknowledgment of source is made. Requests for permission for extended quotation from or reproduction of this manuscript in whole or in part may be granted by the head of the major department or the Dean of the Graduate College when in his or her judgment the proposed use of the material is in the interests of scholarship. In all other instances, however, permission must be obtained from the author.

SIGNED: _____

A handwritten signature in black ink, appearing to be 'M. J. ...', is written over a horizontal line that extends to the right of the 'SIGNED:' label.

ACKNOWLEDGEMENTS

Entre broma y broma mi padre dice a menudo que yo siempre he hecho lo que me ha dado la gana. Pero no lo dice como reproche, ni mucho menos, ya que sus palabras vienen acompañadas de una sonrisa, una sonrisa llena de satisfacción. El y mi madre saben que siempre me han dado toda la libertad para decidir qué camino seguir en la vida...aunque algunos de esos caminos implicaran vivir al otro lado del mundo. Y no sólo me han dado la libertad de elegir, sino que ellos me han abierto muchas puertas y me han animado a cruzar sus umbrales. Papá y Mamá, quiero agradecerlos de todo corazón todas esas oportunidades que siempre me habeis brindado, y el apoyo que incondicionalmente me habeis dado durante toda mi vida. Mamá, quiero agradecerte todos esos discursos sobre lo importante que es ser una mujer independiente, tener una carrera y trabajar en algo que a uno realmente le entusiasme. Papá, quiero agradecerte todas esas horas que desde muy pequeña, y hasta bien entrada en la universidad, me dedicaste para enseñarme pacientemente “maticáticas”, física, química...Y especialmente quiero agradecerlos a vosotros, a María y a Marisa el haberme ayudado a conservar mi entereza cuando uno de mis pilares se derrumbaba...el haberme rescatado del abismo cuando me sentía naufraga en un mar de lágrimas.

Miro atrás y veo a un niño de 13 años. Ahora de repente tiene 19 y ya no es un niño. Si hay algo de lo que realmente me arrepiento es el haber estado lejos de mi hermano mientras crecía. Alvaro, quiero pedirte disculpas por ello y agradecerte todo el cariño que me has dado, y el haberme hecho sentir cerca de tí a pesar de la distancia.

En el teatro de mi vida, Alberto ha sido el actor que mas papeles ha representado. Fue mi tutor, mi viajero aturdido, mi “no-obvio”, mi novio, mi marido, y sobre todo mi mejor amigo. Fue él quien de la mano me introdujo al mundo de la astronomía (y a muchos otros mundos!), y quien contestó pacientemente mis frecuentes preguntas. Fue él la razón principal por la cual decidí cruzar el Atlántico para hacerme astrónoma, y de él fue la idea de elegir para ello este desierto de saguaros y atardeceres rosados. Como tutor y colaborador, quiero agradecerte Alberto todo tu apoyo y las infinitas cosas que me has enseñado. Como amigo, quiero agradecerte el haber compartido tu vida conmigo...el haber sido mi compañero durante este trecho del camino...el haber estado a mi lado...el haber compartido atardeceres...caminatas...poemas de amor...juegos...viajes...rutina...risas y lágrimas. Contigo he sentido los momentos más alegres...y las penas más profundas...y esa montaña rusa de emociones me ha hecho sentirme más humana...y sobre todo me ha hecho crecer.

I feel I just met her, but it has been three years since I started working with her. They say that time flies when one is having fun. And these three years working in my thesis have certainly been fun. The main reason was Renu. I have truly enjoyed working with her. I want to thank her for having her door always open, for spending long hours talking to me on the phone, for reviewing carefully all my manuscripts, for teaching me how to be critical (with everything) and giving me wise advice, and in few words, for being such a wonderful, wonderful advisor. She has taught me many things...but I'm not done yet!...I truly hope I can keep learning from her in the future.

I want to thank my friends Nadya, Almudena, Doug, Philip, Robin, Audra, Maggie, Serena, Catalina, Michelle and Carmen, for being there when I needed them; Sebastian, Mike, Lynne and Dana, for very useful conversations during all these years; Mike, George, Jonathan and Mark, for making the defense of the thesis a really nice and enjoyable experience; and Allan and Jeff for helping me fight with my little computer problems. And finally, I want to thank Suzanne for opening me the door to the Dance department shortly after I arrive to Tucson, and Susan for being such a wonderful dance teacher.

DEDICATION

*Después de un tiempo
 uno aprende la sutil diferencia
 entre sostener una mano y encadenar un alma...
 Y uno aprende que el amor no significa acostarse
 y una compañía no significa seguridad
 y uno empieza a aprender...
 Que los besos no son contratos
 y los regalos no son promesas
 y uno empieza a aceptar sus derrotas
 con la cabeza alta y los ojos abiertos...
 y uno aprende a construir
 todos sus caminos en el hoy,
 porque el terreno de mañana
 es demasiado inseguro para planes...
 y los futuros tienen una forma
 de caerse a la mitad.
 Y después de un tiempo
 que sí es demasiado,
 hasta el calorcito del sol quema,
 así que uno planta su propio jardín
 y decora su propia alma
 en lugar de esperar que alguien le traiga flores.
 Y uno aprende que realmente se puede aguantar,
 que uno realmente es fuerte,
 que uno realmente vale,
 y uno aprende y aprende...
 Y con cada día uno aprende.*

– J.L. Borges.

*Para Mamá y Papá, por todo su amor y por enseñarme a plantar mi propio jardín.
 Para Alvaro, la alegría de mi vida, y de quien en la distancia me siento tan cerca.
 Para Abuelita Leo, por sus dulces cuidados, y su presencia siempre tranquilizadora.
 Para Alberto, el hombre que sostuvo mi mano y encadenó mi alma durante un tercio mi vida... quien me relagó besos, flores y promesas... por quien construí caminos en el mañana... y por quien podría escribir los versos más tristes esta noche...
 Y para mí misma, de la triste figura, que como el olmo viejo mi corazón espera,
 también hacia la luz y hacia la vida, otro milagro de la primavera. Con ♡, Amaya*

TABLE OF CONTENTS

LIST OF FIGURES	9
LIST OF TABLES	11
ABSTRACT	12
CHAPTER 1 Introduction	14
1.1 Overview of Star Formation	15
1.2 Debris Disks as Evidence of Planetary Formation	16
1.3 Do Debris Disks and Giant Planets Coexist?	19
1.4 Overview of Dust Dynamics: How Planets Sculpt Debris Disks	20
1.5 Motivation of This Study	22
CHAPTER 2 Modeling Spatial Density Distributions	26
2.1 Introduction	26
2.2 The Numerical Method	27
2.2.1 The Multiple Time Step Symplectic Integrator SKEEL	28
2.2.2 Radiation Pressure, Poynting-Robertson and Solar Wind Drag	31
2.2.3 Comparison with Analytical Results	34
2.3 Equilibrium Distribution	37
2.3.1 Distribution of Particle Lifetimes	39
2.3.2 Spatial Distribution	43
2.4 Conclusions	43
CHAPTER 3 The Kuiper Belt Dust Disk: a Study Case of a Debris Disk with Giant Planets	49
3.1 Introduction	49
3.2 Distribution of Parent Bodies and Orbital Evolution of Dust Particles	53
3.3 Structure Formation: the Giant Planets Reshape the Debris Disk	54
3.4 Radial Distribution and Mass of the Kuiper Belt Dust Disk	62
3.4.1 Radial Distribution	64
3.4.2 Size Distribution	66
3.4.3 Total Dust Mass	69
3.5 Is the Kuiper Belt a Significant Source of Interplanetary Dust Particles?	71
3.6 Velocities of Kuiper Belt Dust Grains	79
3.7 Other Physical Processes	79
3.7.1 Effect of Heliospheric Magnetic Fields	82
3.7.2 Collisions	84
3.7.3 Sublimation	85

TABLE OF CONTENTS — *Continued*

3.7.4	Sputtering	87
3.8	Conclusions	89
CHAPTER 4 Dust Outflows from Planetary Systems		93
4.1	Introduction	93
4.2	Dependence on Planetary Architecture	94
4.3	Discussion	104
4.3.1	Exo-Planetary Debris Disks and Planet Formation Environment	104
4.3.2	Interpretation of <i>in situ</i> Dust Detections Made by Space Probes	107
CHAPTER 5 Model Spectral Energy Distributions of Circumstellar Debris Disks. Belt of Planetesimals with Interior Giant Planets . .		110
5.1	Introduction	110
5.2	Dust Spatial Density Distributions	112
5.2.1	Radial Density Distributions: Output from the Dynamical Models	116
5.2.2	Radial Density Distributions: Input for the Radiative Trans- fer Models	118
5.3	Correspondence between β and Particle Size	134
5.4	Spectral Energy Distributions	136
5.5	Predicted <i>Spitzer</i> Broadband Colors	165
5.6	Conclusions	166
CHAPTER 6 Future Work		183
6.1	Study of Debris Disk Structure over a Wide Range of Planetary Ar- chitectures.	184
6.2	SEDs: Looking for Planets in Spatially Unresolved Debris Disks. . .	185
6.3	Detailed Modeling of Individual Spatially Resolved Disks.	186
6.4	Intermediate Age Disks: Effect of Gas Drag.	187
REFERENCES		189

LIST OF FIGURES

1.1	Disk evolution	17
1.2	High resolution observations of debris disks	21
2.1	Evolution of semi major axis and eccentricity	36
2.2	Comparison between numerical and analytical results for the evolution of the orbital elements	38
2.3	Lifetimes of (100) test particles	41
2.4	Lifetimes of (300) test particles	42
2.5	Equilibrium number density distribution for three different sets of initial conditions	44
2.6	Radial and azimuthal distributions	45
2.7	Dependence of the equilibrium number density distribution with time and number of longest lived particles	46
3.1	Distribution of eccentricities and inclinations	55
3.2	Initial orbital elements	56
3.3	Equilibrium semimajor axis distribution	58
3.4	Equilibrium number density distributions with planets	59
3.5	Equilibrium number density distributions without planets	60
3.6	Radial density distributions	61
3.7	Composite disk SEDs	63
3.8	Radial profiles of number density in the ecliptic	67
3.9	Particle size distributions	70
3.10	Eccentricities and inclinations of dust grains in Earth-crossing orbits	74
3.11	Example of collected interplanetary dust particle	76
3.12	Non-circular velocity field of KB dust	80
3.13	Ratio of non-circular and the circular velocity of KB dust	81
4.1	Trajectories of the particles that reach 1000 AU after scattering by Jupiter.	98
4.2	Velocities of the dust particles that reach 1000 AU projected in the XY and XZ planes.	100
4.3	Scaling of the average ejection velocity (\bar{v}_∞) with the mass and semi major axis of the planet.	102
5.1	Schematic diagram showing the steps of the modeling approach	113
5.2	Surface density distributions	119
5.3	“Equilibrium” semimajor axis distributions	128
5.4	Correspondence between β and particle radius	137
5.5	SEDs of single particle size disks from the Solar System models	141

LIST OF FIGURES — Continued

5.6	SEDs of disks composed of 1 μm and 40 μm grains from the Solar System models	147
5.7	Effect of the particle size distribution on the SED	150
5.8	SEDs of dust disks with Solar System-like planets, for different grain chemical compositions and particle size distributions	155
5.9	SEDs of dust disks with a $1M_{Jup}$ planet at 1 AU	156
5.10	SEDs of dust disks with a $3M_{Jup}$ planet at 1 AU	157
5.11	SEDs of dust disks with a $10M_{Jup}$ planet at 1 AU	158
5.12	SEDs of dust disks with a $1M_{Jup}$ planet at 5 AU	159
5.13	SEDs of dust disks with a $3M_{Jup}$ planet at 5 AU	160
5.14	SEDs of dust disks with a $10M_{Jup}$ planet at 5 AU	161
5.15	SEDs of dust disks with a $1M_{Jup}$ planet at 30 AU	162
5.16	SEDs of dust disks with a $3M_{Jup}$ planet at 30 AU	163
5.17	SEDs of dust disks with a $10M_{Jup}$ planet at 30 AU	164
5.18	Predicted <i>Spitzer</i> broadband colors	169
5.19	Possible degeneracy between the grain chemical composition and the location of the planet clearing the gap	181

LIST OF TABLES

3.1	Earth-crossing dust grains	73
3.2	Final fate of Kuiper Belt dust grains	78
4.1	Average ejection velocities	96
4.2	Average ejection velocities (cont.)	97
5.1	Final fate of Kuiper Belt dust grains - Estimate of uncertainties	129
5.2	Final Fate of Dust Grains	130
5.3	β -particle radius (μm) relation.	138
5.4	Planetary Systems with Distinct Colors	167

ABSTRACT

Main sequence stars are commonly surrounded by debris disks, composed of cold dust continuously replenished by a reservoir of undetected dust-producing planetesimals. In the outer Solar System, Kuiper Belt (KB) objects produce dust by mutual or interstellar grain collisions.

The orbital evolution of KB dust has been numerically modeled. Its equilibrium radial density distribution can be accurately estimated even though there are inherent uncertainties in the prediction of structure, owing to the chaotic dynamics of dust orbital evolution imposed by resonant gravitational perturbations of the planets. The particle size distribution of dust is greatly changed from the distribution at production, as a result of radiation forces and the perturbations of the planets. The contribution of KB dust to the population of interplanetary dust particles collected at Earth may be as low as a few percent.

Gravitational scattering by giant planets creates an outflow of large grains. We quantify the characteristics of this large-particle outflow in different planetary architectures, discuss its implications for exo-planetary debris disks, and for the interpretation of in-situ dust detection experiments in space probes traveling in the outer Solar System. These outflows may contribute to the clearing of circumstellar debris in planetary systems, affecting the particle size distribution of their local ISM.

In anticipation of future observations of unresolved debris disks with *Spitzer*, we are interested in studying how the structure carved by planets affects the shape of the disk's spectral energy distribution (SED), and consequently if the SED can be used to infer the presence of planets. We numerically calculate the

equilibrium spatial density distributions and SEDs of dust disks originated by an outer belt of planetesimals (35–50 AU) in the presence of different planetary configurations, and for a representative sample of chemical compositions. The dynamical models are needed to estimate the enhancement of particles near the mean motion resonances with the planets, and to determine how many particles drift inside the planet's orbit. Based on the SEDs and predicted *Spitzer* colors we discuss what types of planetary systems can be distinguishable from one another.

CHAPTER 1

Introduction

The search for extra-solar planets is one of the most exciting adventures in science. It addresses a fundamental question that has occupied the human mind for millennia: are there other potential sites for life, far beyond our Earth?

Optical, infrared and millimeter observations have revealed that most newly born stars are surrounded by circumstellar accretion disks of gas and dust, like the hypothetical solar nebula from which the planets in our Solar System once formed. This leads to the idea that potential planetary material is a by-product of star formation. The last decade has witnessed significant progress in this field and we now know that at least some of these circumstellar disks have formed planets, as stellar radial velocity surveys indicate that about 7% of the FGK main sequence stars have a Saturn or Jupiter-mass planet orbiting within 3 AU (Marcy, 2003). But long before planets were discovered by the Doppler technique in the mid 90's, there was indirect evidence of planet building from observations of *debris disks* around several main sequence stars (Backman & Paresce, 1993 and reference therein). These Solar System-sized disks of micron-sized grains are thought to be the result of mutual collisions between asteroid-like bodies or the evaporation of comets close to the star. All these observations indicate that planet formation is indeed a common by-product of the star formation process. But how common? And is our Solar System unique or rare in its configuration? The study of debris disks can help us answer these questions.

1.1 Overview of Star Formation

Most stars are born in molecular clouds. These clouds fragment by some unknown process into denser cores, with molecular hydrogen number densities of 10^3 – 10^4 cm^{-3} , masses of a few $\times M_{Sun}$ and scales of a few $\times 0.1$ pc. Molecular clouds and cloud fragments are roughly consistent with being gravitationally bound, with thermal pressure ($T=10$ – 100 K), turbulent motions, and magnetic fields providing the primary support against gravity. For a star to form, gravity needs to overcome these other forces. This happens in the densest regions, where there is small turbulent motions and substantial dust extinction, shielding the gas from the heating effects of luminous stars (therefore keeping the temperature and the thermal pressure low), and keeping the photoionization level low (reducing the effect of magnetic fields). At this point, the cores reach a critical configuration where they cannot support themselves against gravity, collapsing at nearly free-fall, with expected timescales of only a few hundred thousand years [Hartmann (2000), and references therein].

Typical molecular gas clouds must contract by a factor of a million in linear dimensions to form a star. Because the collapse is so rapid, any angular momentum transfer is inefficient, and therefore any small initial rotation of the star-forming cloud is magnified by conservation of angular momentum, resulting in a rapidly-rotating disk (containing most of the mass) and a smaller, stellar core. About 50% of pre-main-sequence stars have disks at 10^6 years, with disk masses of $(1-10) \times 10^{-2} M_{Sun}$, comparable to the minimum mass solar nebula (the total mass of solar composition material needed to produce the observed condensed material in the Solar System planets).

Disks formation is followed by a longer phase of disk accretion, during which angular momentum is transferred to a small fraction of disk particles at large radial distances, permitting the accretion of most of the disk mass onto the central star. Disk accretion appears to produce the highly-collimated atomic jets (with velocities

of several hundred of km/s and collimation angles of only a few degrees) and slower and less collimated molecular outflows that commonly emanate from young stellar objects. These outflows may play an important role in the energetics and angular momentum transport of inner disk regions. Their collimation mechanism is not fully understood but is thought to result from the magnetic acceleration from the surface of the rotating keplerian disk.

Eventually, infall to the disk stops and the disk becomes depleted in mass: most of the disk mass is accreted onto the central star; some material may be blown away by stellar wind ablation or by photo-evaporation by high-energy stellar photons; and the material that is left behind might coagulate or accrete to form planets. After $\sim 10^7$ years, most of the primordial gas and dust have disappeared (Hartmann, 2000). But in many main sequence stars older than $\sim 10^7$ years ($\sim 15\%$ within ~ 25 pc of the Sun, Habing et al., 2001), a second generation of dust appears forming what is known as a “debris disk” (Aumann et al., 1984). Figure 1.1 shows a schematic representation of disk evolution.

1.2 Debris Disks as Evidence of Planetary Formation

Why called “debris disk”? Stars harboring debris disks are too old to have remnants of the primordial disk from which the star itself once formed. The timescale of dust grain removal due to Poynting-Robertson (P-R) drag for a solar type star is $t_{PR} \sim 400 \times R^2 / \beta$ years $\sim 10^5$ years, where R is the grain distance to the central star in AU, and β is the ratio of the radiation pressure force to the gravitational force (in the range 0–0.5). Grain removal due to radiation pressure is much faster, as the particles escape quickly on hyperbolic orbits. Grain removal timescales are therefore much shorter than the age of main sequence stars, $> 10^7$ years, indicating that these dust disks are not primordial but are produced by a reservoir of undetected kilometer-sized planetesimals producing dust by mutual collisions or by evaporation of comets

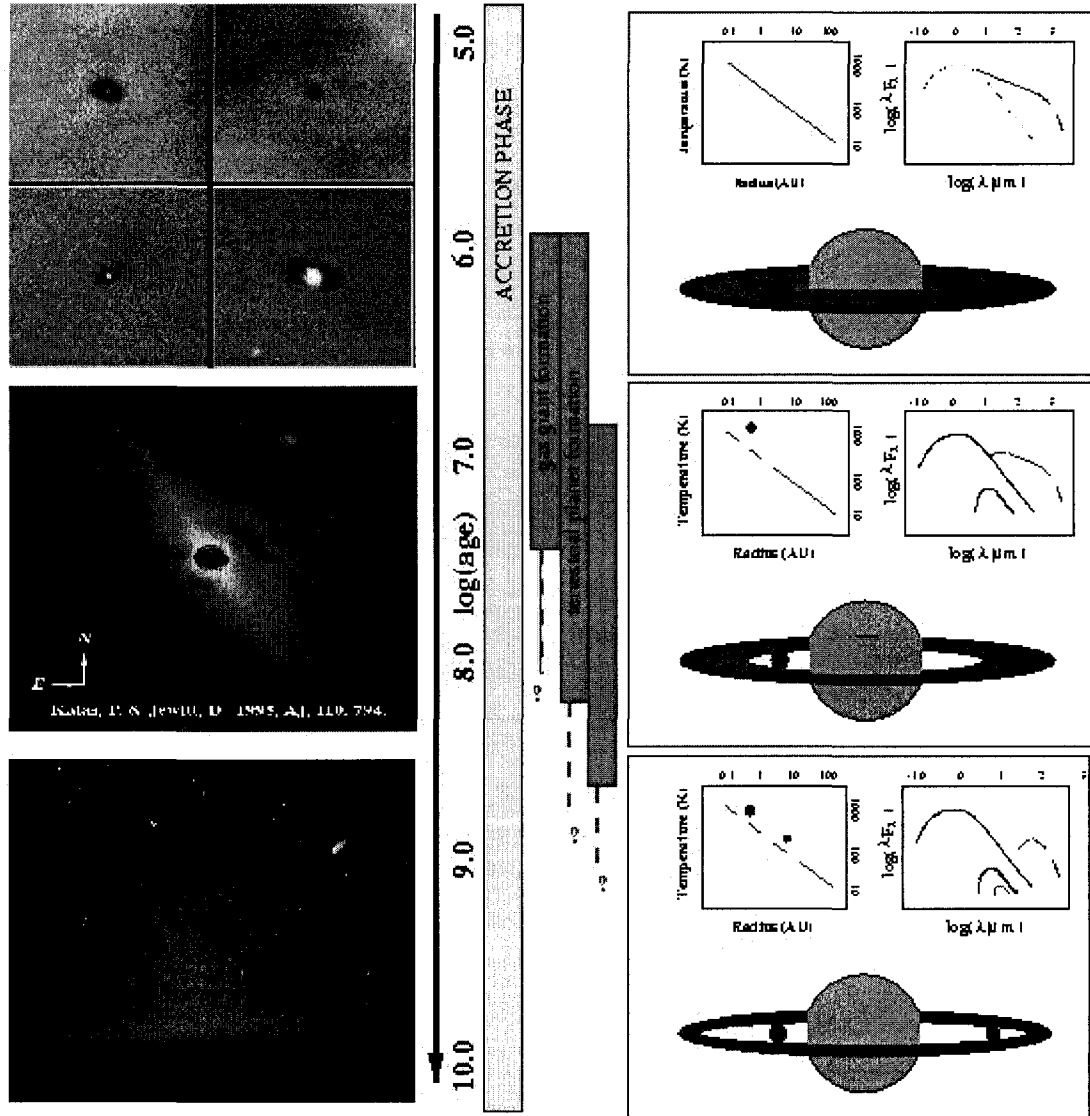


Figure 1.1: (left): Direct images of circumstellar disks at distinct evolutionary stages: (top) *HST* images of silhouette disks seen in projection against the bright background of the Orion Nebula (McCaughrean and O'Dell, 1996); (middle) coronagraphic image of the disks surrounding β -Pictoris seen in scattered light (Kalas and Jewitt, 1995); (bottom) our own zodiacal dust disk (with comet Hale-Bopp) seen from the summit of Mauna Kea (courtesy of Paul Kalas). (right) Schematic SEDs representing early optically thick and later optically thin disks. This study is focused on the last evolutionary stage. This composed figure is a courtesy of Michael Meyer.

scattered close to the star (Backman and Paresce, 1993). Furthermore, in order to induce frequent mutual collisions or infall of comets, the planetesimal orbits must be dynamically perturbed by unseen massive planetary bodies. The spectroscopy of systems like β -Pictoris supports this interpretation (Knacke et al., 1993; Pantin et al., 1997). In the standard scenario, debris disks are generated mainly at early times when planetesimals are forming and colliding frequently; this period would coincide with the heavy bombardment in the early Solar System. In agreement with this scenario, far-infrared surveys with *ISO* indicate that disk detection drops abruptly at ~ 0.4 Gyr (Habing et al., 2001) and that the mass decline in the disks is proportional to t^{-2} between stellar ages of 10 Myr and 1 Gyr (Spangler et al., 2001). The processes responsible for the clearing of dust are stellar winds, radiation pressure, sublimation, collisions (reducing the size of the dust particles until they are small enough to be blown away by radiation pressure) and, as suggested in Chapter 4, gravitational scattering by giant planets.

However, Greaves and Wyatt (2003) found recently that a small number of stars with an age of a few Gyr do have disks, in disagreement with the standard scenario. They claim that Habing et al. (2001) and Spangler et al. (2001) results are biased toward younger ages, as they were preferentially detecting A (younger) stars. These new results indicate that debris disk duration is ~ 0.5 Gyr, and may occur at any time during the main sequence, and that the disk mass decline in time is slow, not steeper than $t^{-1/2}$. It is suggested that the disks have “on” and “off” stages with large differences in dust mass. Furthermore, recent observations by *Spitzer* (Gorlova et al., 2004; Rieke et al., 2004) may suggest that in some cases the debris disk phenomena may be the result of stochastic catastrophic collisional events, rather than a continuous generation of dust for long periods of time. In the study presented in the following chapters we adopt the standard scenario, where dust is produced continuously and a steady state is reached. However, this scenario may need to be revised as it is expected that *Spitzer*, with much higher sensitivity and

better spatial resolution than *ISO* and *IRAS*, will revolutionize our understanding of debris disks.

1.3 Do Debris Disks and Giant Planets Coexist?

We know that at least 15% of A-K main sequence stars are surrounded by debris disks (Zuckerman, 2001), and this percentage could be higher because surveys are sensitivity-limited. We also know from radial velocity surveys that $\sim 7\%$ of FGK main sequence stars have Saturn-to-Jupiter-mass planets within 3 AU (Marcy, 2003). We are still trying to understand the correlation between debris disks and planets. Greaves et al. (2004) carried out a small submillimeter survey of 8 stars with known giant planet companions and found no debris disks down to a dust mass limit of $0.02 M_{Earth}$. Conversely, only $<5\%$ of 20 solar-like stars with debris disks have giant planets inside a few AU, while the majority are inferred to have cavity-clearing planets on large orbits.

High-resolution images of few debris disks have revealed the presence of density structure that suggests that debris disks and planets do coexist. Dynamical models have shown that planets can sculpt the disks, creating gaps, arcs, rings, warps and clumps of dust (Roques et al., 1994; Liou and Zook, 1999; Mouillet et al., 1997; Wyatt et al., 1999; Moro-Martín and Malhotra, 2002; Kuchner and Holman, 2003). The combination of very high resolution imaging at long wavelengths and theoretical dynamical models can provide interpretation of the disks' structure in terms of planetary architectures. Figure 1.2 shows some of these observations. JCMT submillimeter observations of ϵ Eridani show a 60 AU ring with four peculiar peaks of emission (Greaves et al., 1998), that have been interpreted as dust particles captured into the 5:3 and 3:2 exterior resonances with a $0.3 M_{\odot}$ planet at 40 AU and with 0.3 eccentricity (Quillen and Thorndike, 2002); an alternative model suggests a $0.2 M_{Jup}$ planet at a distance of 55–65 AU (Ozernoy et al., 2000). *HST* NICMOS

coronagraphic observations at $1.6\ \mu\text{m}$ of HR 4796A show a ring 70 AU in radius and <14 AU wide, with an abrupt truncation and a clearing inside 50 AU. It is suggested that the dynamical confinement of the dust particles may be due to the influence of one or more unseen planetary bodies (Schneider et al., 1999). High resolution millimeter interferometry observations of the Vega system show two dust concentrations interpreted as dust trapped in the strongest of the distant resonances of a $3\ M_{Jup}$ mass planet at 40 AU and with 0.6 eccentricity (Wilner et al., 2002).

1.4 Overview of Dust Dynamics: How Planets Sculpt Debris Disks

Dust particles are small enough to experience the effect of radiation and stellar wind forces. Radiation pressure makes their orbital elements and specific orbital energy change immediately upon release from parent bodies. If their orbital energy becomes positive, the dust particles escape on hyperbolic orbits. In the Solar System, these particles are known as β -meteoroids (Zook and Berg, 1975). If their orbital energy remains negative, the dust particles stay on bound orbits. P-R and solar wind drag subsequently tend to circularize and decrease the semimajor axis of these orbits, forcing these particles to slowly drift in toward the central star (Burns et al., 1979). Assuming that the dust particles are constantly being produced, this inward drift creates a dust disk of wide radial extent, that is referred to as a *debris disk*. Debris disks are systems that satisfy the following conditions (Backman, 2002): (1) their inferred lifetime is longer than the P-R and collisional lifetimes; (2) they are optically thin to stellar radiation, even along the mid plane; and (3) they have little or no gas, so that the dust dynamics is controlled by gravitation and radiation forces only. [When the gas-to-dust ratio is ~ 1 , i.e. 100 times smaller than the solar nebula, 1 cm-size particles are still affected by gas drag; when the gas-to-dust ratio is $\sim 10^{-4}$, 1 μm -size particles are still affected (Weidenschilling, 2003)].

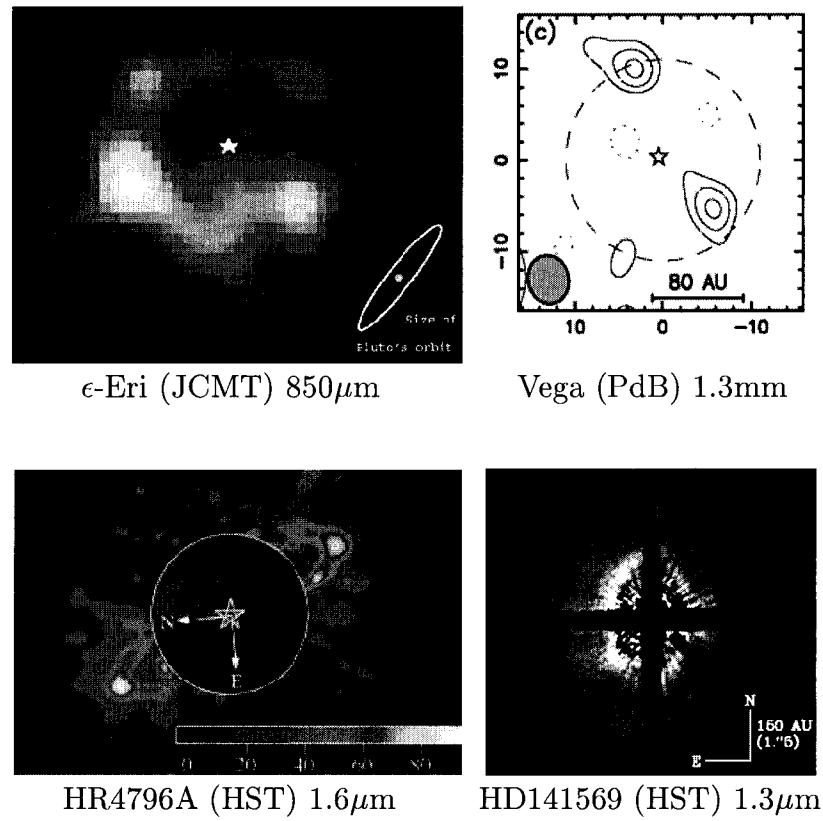


Figure 1.2: High resolution images of debris disks: (top) in thermal emission for ϵ Eridani (Greaves et al., 1998) and Vega (Wilner et al., 2002); and (bottom) in scattered light for HR 4796A (Schneider et al., 1999) and HD141569 (Weinberger et al., 1999).

When planets are present, the journey of the dust particle toward the central star is temporarily interrupted by the trapping of the particle in Mean Motion Resonances (MMRs). MMRs occur when the orbital period of the particle is in a ratio of small integers to that of the perturbing planet. [The $p:q$ MMR means that the orbital period of the particle is p/q times that of the planet, where p and q are integers.] In an MMR, the inward drift is halted because the energy loss due to P-R drag is balanced by the resonant interaction with the planet's gravitational field. This resonance trapping can potentially create structure in debris disks, as the particles accumulate at certain semimajor axes. Sufficiently massive planets may also scatter and eject dust particles out of a planetary system, creating dust free or depleted zones. Such structures, if observed, can be used to infer the presence of planets. Liou and Zook (1999) (hereafter LZ99) found that the presence of the Giant Planets has an important effect on the structure of the debris disk that is presumably generated in the KB: Neptune creates a ring-like structure between 35 and 50 AU, due to the trapping of particles in exterior MMRs, and Jupiter and Saturn are responsible for the ejection of about 80% of particles from the Solar System (Liou et al., 1996) (hereafter LZD96). The latter effect creates a clearing in the inner 10 AU that resembles the inner gap in the β -Pictoris disk. If observed from afar, the KB disk would be the brightest extended feature in the Solar System, and its structure, if spatially resolved, could be recognized as harboring at least two giant planets: an inner planet (Jupiter plus Saturn) responsible for the gap and an outer planet (Neptune) that creates the ring-like structure (LZD96).

1.5 Motivation of This Study

An understanding of the orbits of giant planets in mature planetary systems is fundamental for the study of the stability of orbits in habitable zones, where terrestrial planets could form and survive. One step toward the detection of habitable planets

is the identification of systems in which giant planets orbit well beyond the habitable zone, so that the chaotic regions created near the strongest inner resonances with the planets, and where terrestrial planet orbits could not survive, all lie outside the habitable zone. But the current extra-solar planet detection techniques are not efficient in detecting and characterizing long period planets, so we do not yet have an unbiased and statistically complete census of planetary systems. The study of structure in debris disks may serve as an unbiased (but rough) complementary method to find extra-solar planets, that will allow us to learn about the diversity of planetary systems.

High-resolution space-based optical and near-infrared images of disks in scattered light and ground-based mid-IR, submillimeter and millimeter observations of disks in thermal emission are beginning to probe structures on scales relevant to planetary system formation. Observations of gaps, warps, waves and holes in debris disks serve as indirect evidence for the presence of planetary bodies in these systems, and the combination of these very high resolution images and theoretical dynamical models can provide the interpretation of the disks' structure in terms of planetary architectures (see e.g. Ozernoy et al. (2000), Wilner et al. (2002) and Quillen and Thorndike (2002)). Nevertheless, I find that the current approach for the modeling of these observations is unsatisfactory for two reasons: (1) Numerical models are obtained for only one particle size, even though we know that the structure is significantly different depending on the particle size under consideration. The structure is more pronounced for larger particle sizes because the trapping in resonances is more efficient when the drag forces are small. The modeling of debris disk structure should take into consideration an appropriate range of particle sizes. (2) Either particles are carefully placed in individual resonances or they are restricted to regions containing the main resonances. This is problematic for two reasons: (a) in the presence of giant planet with small eccentricity, the azimuthal structure of the dust disk is not predictable in detail because it depends sensitively

on the times of residence in the various resonances and these are highly variable and unpredictable (for large eccentricity planets this may not be the case); and (b) the relative “strength” of the dominant resonances depends quite strongly on the initial conditions (Moro-Martín and Malhotra, 2002). Therefore, one must be cautious about placing the dust particles *ad hoc*. A better approach, that will give us a more complete physical understanding of the system, would be to consider where the dust-producing planetesimals may be and to release the dust particles from these dust sources.

In the future, ALMA will be able to image the dust in debris disks with an order of magnitude higher spatial resolution (10 milliarcseconds) than VLA and the Hubble Space Telescope, in systems which are more than an order of magnitude fainter; i.e. it will be able to search for analogs of the Kuiper Belt dust disk. Careful modeling of the dust density distributions, like the approach taken here, will be essential to interpret these high resolution observational data. In the more immediate future, *Spitzer* will carry out spectrophotometric observations of hundreds of circumstellar disks that will likely be spatially unresolved. This is why we are interested in studying how the dust density structure affects the shape of the disk spectral energy distribution (SED) and consequently if the SED can be used to infer the presence of planets. About 15% of *Spitzer* guaranteed time observation and two out of its six legacy programs are focused on the detection and characterization of circumstellar disks around nearby stars. In these programs, imaging and spectroscopy will be used to study the spatial structure and composition of the disks, the frequency and duration of the protoplanetary disk phase (constraining the probabilities and timescales for the formation of the major planetary bodies), and the frequency and nature of planetary systems outside our own. Using the type of models presented here, we can interpret some of these observations of unprecedented sensitivity in terms of planetary architectures. The discovery and characterization of planetary systems are two of the eight objectives that define the roadmap of

NASA’s *Origins* program. *Spitzer* is the first of its new space-based missions and its observations will serve to design exo-planet search programs for *SOFIA*, *SIM*, *JWST* and *TPF*. NASA *Origins* objectives, however, cannot be achieved only by the development of advanced technology. To make significant progress, this needs to go hand by hand with a substantial theory/modeling effort. This is the context in which we have carried out the research presented here.

In Chapter 2, we describe the numerical integration method, the method for deriving the equilibrium spatial distributions of dust in debris disks harboring giant planets, and the tests performed to check the suitability of these methods. In Chapter 3, we apply this numerical approach to the study of the Kuiper Belt dust disk, as an example of a debris disks generated by an outer belt of planetesimals with embedded giant planets. In Chapter 4, we describe an effect by which the gravitational scattering of the dust grains by massive planets launches a “wind” of large dust grains. We explore the characteristics of this large-particle outflow in different planetary architectures, and its implications for exo-planetary debris disks and for the interpretation of in-situ dust detection experiments in space probes traveling in the outer Solar System. In Chapter 5, we explore how the structure carved by the planets affects the shape of the disk’s spectral energy distribution (SED), and consequently if the SED can be used to infer the presence of planets in spatially unresolved debris disks. Finally, Chapter 6 describes our plans for the future.

CHAPTER 2

Modeling Spatial Density Distributions

2.1 Introduction

The modeling of the spatial density distribution of dust in debris disks requires the study of the dynamical evolution of the grains. We numerically solve the equations of motion of hundreds of dust particles, in the size range from 1 to 40 μm (for $\rho=2.7 \text{ g/cm}^3$), or from 3 to 120 μm (for $\rho=1 \text{ g/cm}^3$), generated in a debris disk analogous to the Solar System's Kuiper Belt. For the orbit integrations, we use a modified version of the multiple time step symplectic method SyMBA (Duncan et al., 1998; Moro-Martín and Malhotra, 2002). Our models include the combined effects of solar gravity, solar radiation pressure, the P-R effect and solar wind drag, and the gravitational forces of planets. We model the Solar System with 7 planets (excluding Mercury and Pluto, and including the mutual perturbations of the planets), and we model hypothetical systems without planets. In each model system, the parent bodies of the dust particles are assumed to be uniformly distributed in orbits with semimajor axis between 35 and 50 AU, eccentricities such that the perihelion distances are between 35 and 50 AU, and inclinations between 0° and 17° , in approximate accord with current estimates of the orbital distribution of the classical Kuiper Belt (Malhotra et al., 2000; Brown, 2001). On all our models, the initial values of mean anomaly (M), longitude of ascending node (Ω) and argument of perihelion (ω) were randomly distributed between 0 and 2π . The sinks of dust included in our numerical simulations are (1) ejection into unbound orbits, (2) accretion into the planets, and (3) orbital decay to less than 0.5 AU heliocentric

distance.

In §2.2 we describe our numerical integration method and the tests performed to check the suitability of the code; §2.3 describes our methods for deriving the equilibrium spatial distribution of the dust disk; and §2.4 summarizes our results.

2.2 The Numerical Method

In order to study the dynamics of dust from the KB we need to solve the problem of the dynamical evolution of micron-sized particles, under the effect of gravitational forces of the Sun and the planets and radiation and solar wind forces. This has been solved in the past using the adaptive step size Runge-Kutta integrator RADAU (Liou and Zook, 1997; Kortenkamp and Dermott, 1998; Liou and Zook, 1999; Liou et al., 1999). Another possible choice is the standard mixed variable symplectic (MVS) integrator, developed by Wisdom and Holman (1991). Its advantage over implicit Runge-Kutta integrators is its speed, about an order of magnitude faster (Wisdom and Holman, 1991). This is why the MVS method is now used in long-term studies of the Solar System, allowing us to reach integration times approaching the age of the system. Its disadvantage, however, is that it cannot handle close encounters amongst bodies. Since the outcome of close encounters between the dust particle and the planets is critical for the study of the dynamical evolution of dust grains, previous researchers have chosen RADAU as their numerical integrator. But recently, Duncan et al. (1998) (hereafter DLL98) have developed a new multiple time step symplectic algorithm, SyMBA, that can handle close encounters in a symplectic way, thus retaining the speed of the MVS method while being able to overcome its main disadvantage.

The equations of motion of the N-body system are integrated using a variation of SyMBA called SKEEL, which we have modified to include radiation forces.

In this section, we summarize the main features of SKEEL as described in DLL98, followed by a description of how radiation forces were introduced and the tests that we have performed to check the validity of our results.

2.2.1 The Multiple Time Step Symplectic Integrator SKEEL

The MVS method solves the Newtonian gravitational N-body problem by separating its Hamiltonian,

$$H = \sum_{i=0}^n \frac{|\mathbf{p}_i|^2}{2m_i} - \sum_{i=0}^{n-1} \sum_{j=i+1}^n \frac{Gm_i m_j}{r_{ij}}, \quad (2.1)$$

into two integrable components,

$$H = H_0 + H_1 = H_{kep} + H_{int}, \quad (2.2)$$

where H_{Kep} is the dominant Keplearian Hamiltonian,

$$H_{Kep} = \sum_{i=1}^n \left(\frac{|\mathbf{p}_i'|^2}{2m_i'} - \frac{Gm_i m_0}{r_i'} \right), \quad (2.3)$$

and H_{int} is the interaction Hamiltonian,

$$H_{int} = \sum_{i=1}^n \left(\frac{Gm_i m_0}{r_i'} - \frac{Gm_i m_0}{r_{i0}} \right) - \sum_{i=1}^{n-1} \sum_{j=i+1}^n \frac{Gm_i m_j}{r_{ij}}. \quad (2.4)$$

$r_{ij} = |\mathbf{q}_i - \mathbf{q}_j|$ is the distance between particles i and j , \mathbf{p}_i is the momentum of particle i , \mathbf{q}_i is its conjugate phase space coordinate and m_i is its mass, with $i=0$ corresponding to the Sun. The separation into two integrable Hamiltonians is possible using jacobian coordinates, denoted by the primed variables. In the jacobian framework, the coordinates and momenta of each body are referred to a system whose origin is at the center of mass of all the bodies with lower indices (Wisdom and Holman, 1991).

The time evolution of the N-body system can be expressed by

$$\mathbf{w}(\tau) = e^{\tau\{H\}}\mathbf{w}(0) = e^{\tau\{H_0+H_1\}}\mathbf{w}(0), \quad (2.5)$$

where the curly braces refer to the Poisson bracket operator and $\mathbf{w} = (\mathbf{q}, \mathbf{p})$ is the phase space coordinate. A second order symplectic integrator consists in approximating the time evolution by

$$e^{\tau\{,H_0+H_1\}} \approx e^{(\tau/2)\{,H_0\}} e^{\tau\{,H_1\}} e^{(\tau/2)\{,H_0\}}, \quad (2.6)$$

also denoted by

$$E_0\left(\frac{\tau}{2}\right) E_1(\tau) E_0\left(\frac{\tau}{2}\right), \quad (2.7)$$

where $E_i(\tau)$ is the evolution under H_i for time τ . Note that during close encounters, r_{ij} becomes small, the second term in H_{int} grows, and since the speed of the MVS method relies on having $H_{kep} \gg H_{int}$, the MVS method fails (DLL98). To overcome this problem, Duncan, Levison & Lee developed SKEEL, a multiple time step symplectic method applied to a Hamiltonian equivalent to (2.1),

$$H(Q_i, P_i) = \sum_{i=1}^n \left(\frac{|P_i|^2}{2m_i} - \frac{Gm_i m_0}{|Q_i|} \right) + \frac{|P_0|^2}{2m_{tot}} + \frac{1}{2m_0} \left| \sum_{i=1}^n P_i \right|^2 - \sum_{i=1}^{n-1} \sum_{j=i+1}^n \frac{Gm_i m_j}{|Q_i - Q_j|} \quad (2.8)$$

where,

$$Q_i = \begin{cases} q_i - q_0 & \text{if } i \neq 0 \\ \frac{1}{m_{tot}} \sum_{j=0}^n m_j q_j & \text{if } i = 0 \end{cases}$$

and

$$P_i = \begin{cases} p_i - \frac{m_i}{m_{tot}} \sum_{j=0}^n p_j & \text{if } i \neq 0 \\ \sum_{j=0}^n p_j & \text{if } i = 0. \end{cases}$$

Q_i and P_i are respectively the heliocentric positions and barycentric momenta (if $i \neq 0$) and the position of the center of mass and the total momentum of the system (if $i = 0$). m_{tot} is the total mass of the system.

The separation into integrable parts now becomes,

$$H(Q_i, P_i) = H_{Kep} + H_{Sun} + H_{int}, \quad (2.9)$$

where

$$H_{Kep} = \sum_{i=1}^n \left(\frac{|P_i|^2}{2m_i} - \frac{Gm_i m_0}{|Q_i|} \right), \quad (2.10)$$

$$H_{Sun} = \frac{1}{2m_0} \left| \sum_{i=1}^n \mathbf{P}_i \right|^2, \quad (2.11)$$

$$H_{int} = - \sum_{i=1}^{n-1} \sum_{j=i+1}^n \frac{Gm_i m_j}{|\mathbf{Q}_i - \mathbf{Q}_j|}. \quad (2.12)$$

The contribution from the second term in the *rhs* of (2.8) is ignored because it corresponds to the center of mass that moves as a free particle. A second order symplectic integrator consists in approximating the time evolution by the following symmetrized sequence of steps,

$$E_{Sun} \left(\frac{\tau}{2} \right) E_{int} \left(\frac{\tau}{2} \right) E_{Kep}(\tau) E_{int} \left(\frac{\tau}{2} \right) E_{Sun} \left(\frac{\tau}{2} \right), \quad (2.13)$$

where $E_i(\tau)$ is the evolution under H_i for time τ . For each body there is: (1) a linear drift in position by $(\tau/2m_0) \sum \mathbf{P}_i$, to account for the motion of the Sun with respect to the barycenter; (2) a kick to its momentum for time $(\tau/2)$, to account for the gravitational forces of all the massive bodies except the Sun; (3) an evolution along a Kepler orbit for time τ ; (4) another kick like (2); (5) another linear drift like (1). During a close encounters between a particle and a planet, the contribution from the encountering planet is separated from the rest so that the time evolution becomes

$$E_{Sun} \left(\frac{\tau}{2} \right) E_{int}^{ne} \left(\frac{\tau}{2} \right) E_{int}^{enc} \left(\frac{\tau}{2} \right) E_{Kep}(\tau) E_{int}^{enc} \left(\frac{\tau}{2} \right) E_{int}^{ne} \left(\frac{\tau}{2} \right) E_{Sun} \left(\frac{\tau}{2} \right), \quad (2.14)$$

where E_{int}^{ne} refers to the contribution to H_{int} from all the planets except the one in the encounter, and E_{int}^{enc} is the same but for the planet in the encounter only. The close-encounter algorithm, represented by

$$E_{int}^{enc} \left(\frac{\tau}{2} \right) E_{Kep}(\tau) E_{int}^{enc} \left(\frac{\tau}{2} \right), \quad (2.15)$$

is as follows. The two-body potential terms in H_{int} , due to the encountering planet, are decomposed into

$$\frac{Gm_i m_j}{|\mathbf{Q}_i - \mathbf{Q}_j|} = \sum_{k=0}^{\infty} V_k. \quad (2.16)$$

For details about the conditions V_k need to satisfy and the particular functions used in SKEEL, see DLL98. The multiple time step method consists then in applying (2.15) recursively,

$$E_{\Sigma_0}(\tau) \approx E_0\left(\frac{\tau_0}{2}\right) E_{\Sigma_1}(\tau_0) E_0\left(\frac{\tau_0}{2}\right) \approx E_0\left(\frac{\tau_0}{2}\right) [E_1\left(\frac{\tau_1}{2}\right) E_{\Sigma_2}(\tau_1) E_1\left(\frac{\tau_1}{2}\right)]^M E_0\left(\frac{\tau_0}{2}\right) \quad (2.17)$$

where $E_i(\tau)$ and $E_{\Sigma_i}(\tau)$ are the evolution for time τ under V_i and $H_{Kep} + H_{Sun} + \sum_{k=i}^{\infty} V_k$ respectively. At each level of recursion, the evolution under $E_{\Sigma_i}(\tau)$, is approximated by: (1) evolution under V_i for $\tau/2$; (2) M second-order steps of length τ ; (3) evolution under V_i for $\tau/2$. This is equivalent to placing concentric shells around the massive body; the smaller the shell, the smaller the time step associated with it, allowing to resolve peri-planet passage. In particular, DLL98 uses $\tau_k/\tau_{k+1} = M$; for our runs, $M = 3$. Note that this multiple time step algorithm only activates during close encounters. When the bodies are farther apart, the algorithm reduces to (2.13); this is because $\{H_{Sun}, H_{Kep}\} = \{H_{Sun}, H_{int}\} = 0$, so that the pairs are interchangeable.

We use units in which $G=1$; the unit of mass is $1M_{\odot}$, the unit of length is 1 AU and the unit of time is the period of a massless particle at 1 AU divided by 2π .

2.2.2 Radiation Pressure, Poynting-Robertson and Solar Wind Drag

For simplicity, let's consider radiation forces in the 2-body problem. [The generalization to the N-body problem is trivial if we assume that the mass of the central body is dominant over the rest of the massive bodies]. A particle of mass μ , moving with velocity v with respect to a central body, which is the source of a radiation field of energy flux density $S=L/4\pi r^2$, feels a force due to the absorption and re-emission

of radiation that is given (to terms of order v/c) by Burns et al. (1979),

$$\mu \frac{d^2 \mathbf{r}}{dt^2} = \frac{SAQ_{pr}}{c} \left[\left(1 - \frac{\dot{r}}{c} \right) \hat{S} - \frac{\mathbf{v}}{c} \right], \quad (2.18)$$

where A is the geometric cross section of the particle, \mathbf{r} and \mathbf{v} are its heliocentric position and velocity and \hat{S} is the unit vector in the direction of the incident radiation. Q_{pr} is the radiation pressure coefficient, a measure of the fractional amount of energy scattered and/or absorbed by the grain. Q_{pr} is a function of the physical properties of the grain and the wavelength of the incoming radiation; the value we use is an average integrated over the solar spectrum. We will refer to the velocity dependent part of (2.18) as the *Poynting – Robertson* (P-R) *drag* and to the radial term as the *radiation pressure* force. The radiation pressure force arises from the interception by the particle of the momentum carried by the incident solar photons. The factor $(1-\dot{r}/c)$ is due to the Doppler effect that modifies the energy flux of the incident radiation by shifting its wavelength. The P-R drag arises from the motion of a particle of velocity \mathbf{v} through a radiation field with finite velocity c (Burns et al., 1979). In the inertial reference frame, it can be thought of as a *mass loading drag*: the re-emitted radiation emits more momentum into the forward direction of motion due to the Doppler effect, which means that the particle loses momentum; since the mass is conserved, the particle is decelerated (there is a drag force). In the particle's reference frame it originates from the aberration of the radiation, that generates a drag force.

We can define the dimensionless constant β as the ratio between the radiation pressure force, $F_r = SAQ_{pr}/c$, and the gravitational force, $F_g = Gm_0\mu/r^2$, so that $\beta = F_r/F_g = SAQ_{pr}r^2 / (Gm_0\mu c) = (3L/16\pi Gm_0 c)(Q_{pr}/\rho s)$. For the Sun, $\beta = 5.7 \times 10^{-5} Q_{pr}/\rho s$, where ρ and s are the density and radius of the grain in cgs units (Burns et al., 1979). The advantage of using the dimensionless parameter β is that it is independent of distance, being a function only of the particle size and

composition. Using this notation, the equation of motion for the 2-body problem is

$$\frac{d^2\mathbf{r}}{dt^2} = \frac{-Gm_0}{r^3}\mathbf{r} + \beta\frac{Gm_0}{r^2}\left[\left(1 - \frac{\dot{r}}{c}\right)\hat{\mathbf{S}} - \frac{\mathbf{v}}{c}\right], \quad (2.19)$$

and after rearranging some terms and using the fact that $\hat{\mathbf{S}}=\mathbf{r}/r$ becomes,

$$\frac{d^2\mathbf{r}}{dt^2} = \frac{-Gm_0(1 - \beta)}{r^3}\mathbf{r} - \frac{\beta}{c}\frac{Gm_0}{r^2}\left[\left(\frac{\dot{r}}{r}\right)\mathbf{r} + \mathbf{v}\right]. \quad (2.20)$$

Solar wind corpuscular forces also affect the motion of the particle. The *solar wind pressure*, equivalent to the radiation pressure, can be ignored because the momentum flux carried by the solar wind is about 2×10^{-4} that of the radiation (Burns et al., 1979), but the *solar wind drag*, equivalent to the P-R drag, may not be negligible. We can easily include this force by using the dimensionless parameter *sw*, ratio of the solar wind drag to the P-R drag. In this paper we use *sw*=0.35 (Gustafson, 1994). The equation of movement is then

$$\frac{d^2\mathbf{r}}{dt^2} = \frac{-Gm_0}{r^3}\mathbf{r} + \beta\frac{Gm_0}{r^2}\left[\left(1 - (1 + sw)\frac{\dot{r}}{c}\right)\hat{\mathbf{S}} - (1 + sw)\frac{\mathbf{v}}{c}\right], \quad (2.21)$$

and after rearranging,

$$\frac{d^2\mathbf{r}}{dt^2} = \frac{-Gm_0(1 - \beta)}{r^3}\mathbf{r} - \frac{\beta_{sw}}{c}\frac{Gm_0}{r^2}\left[\left(\frac{\dot{r}}{r}\right)\mathbf{r} + \mathbf{v}\right], \quad (2.22)$$

where $\beta_{sw} = (1+sw)\beta$. The Hamiltonian associated to the first term in the *rhs* of eq. (2.22) is H_{Kep} in eq.(2.10), with $m_0(1-\beta)$ instead of m_0 . Physically, this means that radiation pressure makes the dust grain *feel* a less massive Sun. In our numerical integrator, SKEEL-RAD, we introduce the second term in (2.22), the P-R and solar wind drag term, as an additional *kick* to the momentum of the particle. The algorithm thus becomes,

$$E_{Sun}\left(\frac{\tau}{2}\right) E_{int}^{rad}\left(\frac{\tau}{2}\right) E_{Kep}^{rad}(\tau) E_{int}^{rad}\left(\frac{\tau}{2}\right) E_{Sun}\left(\frac{\tau}{2}\right). \quad (2.23)$$

The radiation pressure force shifts the location of a MMR with a planet. For a planet at a_{pl} , the location of the the p:q MMR in the presence of radiation is,

$$a = a_{pl}(1 - \beta)^{1/3}\left(\frac{p}{q}\right)^{2/3} \quad (2.24)$$

2.2.3 Comparison with Analytical Results

There is no analytic solution to the general problem of a particle moving under the effect of gravitational forces from the Sun and the planets and radiation and solar wind forces. For this reason, the code cannot be tested in the most general case. But there are analytic solutions for the evolution of the orbital elements of a particle under the effect of radiation in the 2-body problem (Wyatt and Whipple, 1950; Burns et al., 1979) and in the circular restricted 3-body problem (Liou and Zook, 1997). We will use these solutions to test the numerical procedure and the validity of our results.

1. *Jacobi Constant Conservation*

In the circular restricted 3-body problem, consisting of a massless particle, a central mass and a planet in a circular orbit, the Jacobi constant is an integral of the motion. We have integrated the orbits of 50 massless particles in the presence of the Sun and Neptune (with $a=30$ AU and $e=0$). The semimajor axes of the particles were uniformly distributed between 36 and 40 AU and the perihelion distance was set to 30 AU. We use a step size of 2 years and an integration time of 10^9 years. We found that 34 out of 50 particles have close encounters, with $\Delta J/J(0) \sim O(10^{-6})$ – $O(10^{-7})$. The remaining 16 that do not suffer close encounters have $\Delta J/J(0) \sim O(10^{-8})$. The worst jacobi conservation has $\Delta J/J(0) \sim 7 \cdot 10^{-6}$. These results suggests that close encounters are integrated accurately.

2. *Rates of Change of Orbital Elements*

Burns et al. (1979), following Wyatt and Whipple (1950), derived the time rates of change (averaged over an orbit) of semimajor axis (a), eccentricity (e), and inclination (i), of a particle in the 2-body problem in the presence of radiation and solar wind forces,

$$\left(\frac{da}{dt}\right)_{PR} = -\frac{(1+sw)\beta m_0}{c} \frac{2+3e^2}{a(1-e^2)^{3/2}}, \quad (2.25)$$

$$\left(\frac{de}{dt}\right)_{PR} = -\frac{5(1+sw)\beta m_0}{2c} \frac{e}{a^2(1-e^2)^{1/2}}, \quad (2.26)$$

$$\left(\frac{di}{dt}\right)_{PR} = 0. \quad (2.27)$$

Figure 2.1 presents the evolution of a and e for a particle with $\beta=0.2$ and $sw=0.35$. The agreement between the numerical and analytical results is perfect.

When radiation is introduced into the circular restricted 3-body problem, the Jacobi constant is no longer an integral of the motion. Using the time variation of the Jacobi constant due to radiation and solar wind forces, together with the time rate of change of the Tisserand criterion, Liou and Zook (1997) have derived analytic expressions that describe the orbital evolution of a particle trapped in a MMR with a planet. The equation relating the time variation in e and i is

$$\frac{e}{(1-e^2)^{1/2}} \cos i \frac{de}{dt} + (1-e^2)^{1/2} \sin i \frac{di}{dt} = \frac{\beta_{sw} m_0}{a^2 c} \left[\cos i - \frac{a_{pl}^{3/2} (3e^2 + 2) (1-\beta)^{1/2}}{2a^{3/2} (1-e^2)^{3/2}} \right], \quad (2.28)$$

where $\beta_{sw}=(1+sw)\beta$ and a and a_{pl} are the semimajor axis of the resonant orbit and the planet respectively, related by equation

$$a = a_{pl} (1-\beta)^{1/3} \left(\frac{p}{q}\right)^{2/3}. \quad (2.29)$$

In the particular case when $i=0$,

$$\dot{e} = \frac{(1+sw)\beta m_0 (1-e^2)^{1/2}}{a^2 c e} \left[1 - \frac{a_{pl}^{3/2} (3e^2 + 2) (1-\beta)^{1/2}}{2a^{3/2} (1-e^2)^{3/2}} \right]. \quad (2.30)$$

The expansion of eq. (2.16) to second order in e and i allows to decouple their time variations; after integrating the resulting two differential equations, Liou and Zook (1997) arrive at these equations (valid only for e-type resonances),

$$e^2 = [e_0^2 - \frac{K-1}{3}] \exp\left(-\frac{3A}{K}t\right) + \frac{K-1}{3}, \quad (2.31)$$

$$i = i_0 \exp\left(-\frac{A}{4}t\right), \quad (2.32)$$

where $A=2(1+sw)\beta m_0/a^2 c$ and $K=p/q$; p and q are the two integers that specify the $p:q$ resonance ($K>1$ for exterior MMR, and $K<1$ for interior MMR). To carry

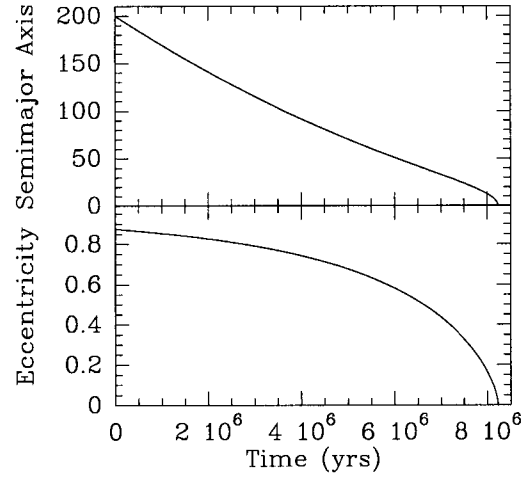


Figure 2.1: Evolution of a and e for a particle with $\beta=0.2$ and $sw=0.35$ in the 2-body problem. The solid and the dotted lines coincide and represent the numerical and analytical results respectively.

out the comparison between analytical and numerical results, we have followed the orbital evolution of 100 pyroxene dust particles, $1\mu\text{m}$ in diameter ($\beta=0.17$, $\text{sw}=0.35$) in a circular Sun-Neptune system. The different panels in Figure 2.2 show the evolution of four of these particles trapped in the 1:1, 5:3, 4:3 and 5:6 MMR with Neptune ($a=30\text{ AU}$, $e=0$). The agreement with equation (2.19) is good for small eccentricities, where the analytical expression holds. We conclude that the code is treating radiation and solar wind forces accurately.

2.3 Equilibrium Distribution

Ideally, one would like to be able to follow the evolution of a number of particles large enough to resolve the disk structure. However, even though our numerical integrator is very efficient, this task is not feasible with the current computational power. We estimate that for a 50 AU radius disk about 10^5 particles would be needed to resolve the structure induced by the Solar System planets. To get around this problem, LZ99 used the following approach to obtain the equilibrium spatial distribution of the dust using only 100 particle simulations: first integrate the orbits from their source in the KB until they are either ejected from the Solar System or drifted into the Sun, recording the positions of the particles every 1000 years; then transform the particles' coordinates into a reference frame rotating with the planet dominating the structure (Neptune); and finally accumulate all the rotated coordinates. This yields a time-weighted spatial distribution of the 100 particles over their dynamical lifetime. It is equivalent to the actual spatial density distribution of KB dust provided: (1) the dust production rate is in equilibrium with the loss rate, and (2) the dust particle dynamics is ergodic (i.e. the time-weighting reflects the spatial density). LZ99 point out one limitation of this approach: it assumes the same planetary configuration at the time of release of the dust particles (i.e. every 1000 years). There are, however, other more important limitations that were

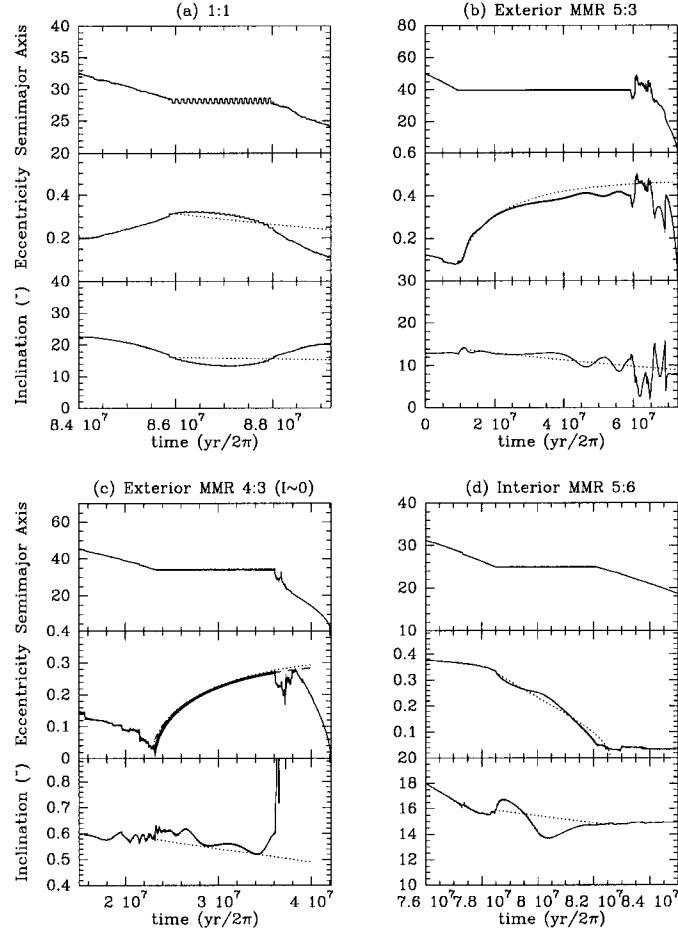


Figure 2.2: Comparison between numerical (solid line) and analytical results for the the evolution of the orbital elements of $1\mu\text{m}$ pyroxene dust particles ($\beta=0.17$, $\text{sw}=0.35$) in a circular Sun-Neptune-dust system. Neptune is placed at 30 AU with $e=0$. The dotted lines represent the analytical results given by (2.19) and (2.20) (valid to 2nd order in eccentricity and inclination) and the dashed line correspond to (2.18) (valid for all eccentricities when $i=0$). (a) Particle trapped for 2 Myr in the 1:1 MMR with Neptune. Since the eccentricity is already quite large at the time of trapping ($e \sim 0.3$), the agreement with (2.19) is not very good. (b) Particle trapped for 50 Myr in the exterior 5:3 MMR with Neptune. The agreement is very good until the eccentricity reaches ~ 0.3 , at that point it starts to deviate. (c) Particle trapped for 14 Myr in the exterior 4:3 MMR with Neptune. At the time of trapping, the inclination is very small ($\sim 0.6^\circ$). The evolution of the eccentricity is perfectly described by (2.18) and (2.19). (d) Particle trapped for 4 Myr in the interior 5:6 MMR with Neptune. The overall evolution of eccentricity and inclination are described reasonably well by (2.19). The semimajor axis stays constant as the eccentricity decreases until it reaches the limiting value 0, the point at which the particle leaves the resonance.

overlooked by LZ99. We consider these in detail because this is presently the only feasible approach to the problem of structure formation in debris disks.

2.3.1 Distribution of Particle Lifetimes

Owing to the ergodic assumption, the debris disk structure obtained using LZ99 approach is determined to a large extent by the longest lived particles, which represent only a very small fraction of the dust population. The question is: are these particles anomalous, or are they part of a continuous distribution of lifetimes? In the case of anomalies, the structure would be dominated by the dynamics of a very small number of particles of uncertain significance, in which case the structure obtained by LZ99 approach would not necessarily resemble any equilibrium distribution. If the second option were true, however, the longest lived particles would indeed be statistically significant, since they will represent the contribution from an existing population of particles whose lifetimes are part of a long tail in a continuous distribution.

In order to answer this question, we have studied the lifetimes of the particles in all our models for the Solar System run so far. To facilitate discussion, we include here the list of our models.

- Models I-A: parent bodies at $a=45$ AU, $e=0.1$ and $i=10^\circ$. 4 giant planets.
- Models I-B: same as above but without planets.
- Models II-A: parent bodies randomly distributed between $a=35$ -50AU, perihelion $q=35$ -50 AU and $i=0$ - 17° . 7 planets (excluding Mercury and Pluto).
- Models II-B: same as above but without planets.

For all models, the mean anomaly (M), longitude of ascending node (Ω) and argument of perihelion (ω) of dust particles, were randomly distributed between 0 and 2π . All models were run with 100 particles each for 5 different β s: 0.01, 0.05, 0.1, 0.2 and 0.4; for a density of 2.7 g cm^{-3} , these values correspond to particle sizes

of 40, 9, 4, 2 and 1 μm , respectively; for 1 g cm^{-3} , they correspond to 120, 23, 11, 6 and 3 μm , respectively.

Figure 2.3 shows the lifetimes for all the particles in our models. For the present discussion, the difference between having 4 or 7 planets is not important. What is important for this argument is that the initial conditions of the parent bodies are different upon release of the dust particles. We see in Figure 2.3 that the median lifetime and the dispersion of lifetimes are both systematically smaller for larger β . The longer lifetimes are due to longer trapping at exterior MMRs with Neptune. The residence time in an MMR is variable and unpredictable owing to the underlying chaotic resonance dynamics (Malhotra et al., 2000). From the point of view of using these simulations to obtain the equilibrium spatial distribution of dust, the most worrisome feature is that the lifetime of the longest-lived particle may be several times longer than the next longest-lived, and more than an order of magnitude greater than the median lifetime. This may be due to numerical errors that affect the behavior of a few particles, or it may be due to the underlying chaotic dynamics that produces a long tail in a continuous distribution of dynamical lifetimes.

To distinguish between these two possibilities, two additional runs of 100 particles each (with different random values of M , Ω and ω) were done for Model I-A with $\beta=0.1$. The results are shown in Figure 2.4. We see that with increasing number of particles, the gap between the longest and next longest lived particle is reduced. Overall, the distribution of lifetimes resembles the sum of a gaussian and a uniform distribution. With only a few hundred particles in numerical simulations, we are limited to small numbers of long lived particles. However, we conclude with some confidence that the longest lived particles are not anomalous but statistically representative of a real dynamical population.

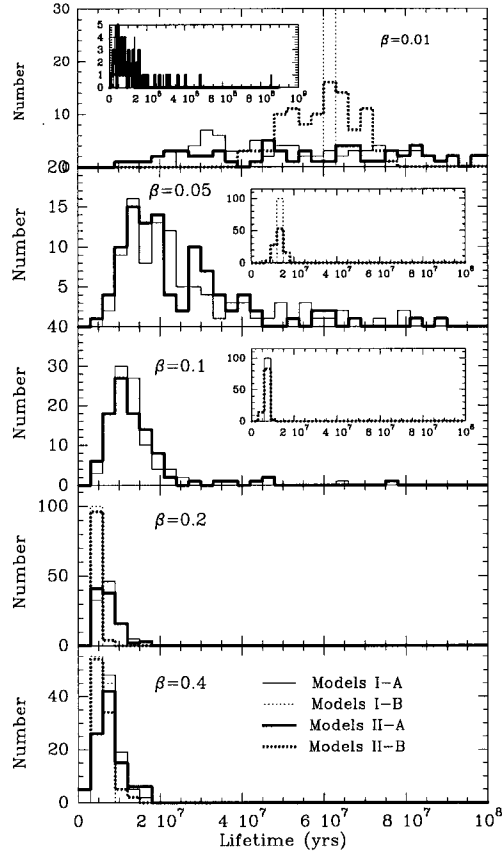


Figure 2.3: Lifetimes of the particles in models I-A (with 4 planets; thin solid line), models I-B (without planets; thin dotted lines), models II-A (with 7 planets; thick solid line) and models II-B (without planets; thick dotted lines). The insert for $\beta=0.01$ is included to show the full time expand of these very long-lived particles. The inserts for $\beta=0.05$ and $\beta=0.1$ show the no-planet models separately to avoid confusion. The presence of the planets increases the lifetime of the particles. The smaller the beta, the largest the difference between the planets and no-planets cases: the trapping into MMRs is more efficient when the drag force is small.

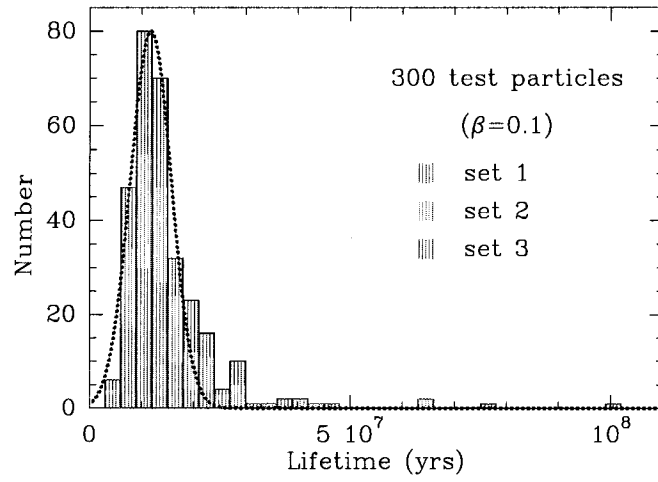


Figure 2.4: Lifetimes for the three models I-A, 100 particles each, plotted together with the different colors representing the contribution from the 3 different runs. The distribution of lifetimes reassembles that of a gaussian (dotted line) plus a long tail.

2.3.2 Spatial Distribution

Figure 2.5 shows the “equilibrium” number density distributions that result after applying LZ99 approach to the three models I-A with $\beta=0.1$. The relative occurrence of the different MMRs can also be seen in the histogram presented in this figure. Note that the only difference between the three runs is in the initial M , Ω and ω . We see that the dust particles’ times of residence in various mean resonances with Neptune are highly variable.

Figure 2.6 shows the radial profiles (averaged over all θ) and angular profiles (integrated between 25 and 35 AU) of the number and brightness (see §5) density distribution derived from 4 different sets of 100 particles each. This figure indicates that the LZ99 approach: (1) is able to predict reliably the radial structure; and (2) the azimuthal structure is not predictable in detail, except for a ‘gap’ near the outermost planet Neptune.

We have explored how fast structure is created and the effect of excluding the contribution to the structure from the longest lived particles. Our results, which are summarized in Figure 2.7, show that the structure is created quickly and that the radial profiles of the number density distribution do not strongly depend on the contribution from the longest lived particles. This provides further validation of the LZ99 approach.

2.4 Conclusions

(1) We have followed, from source to sink, the orbital evolution of dust particles from the Kuiper Belt. To integrate the equations of motion efficiently, we have introduced radiation and solar wind forces in the multiple time step symplectic integrator of DLL98. We have established the suitability of our code by comparison

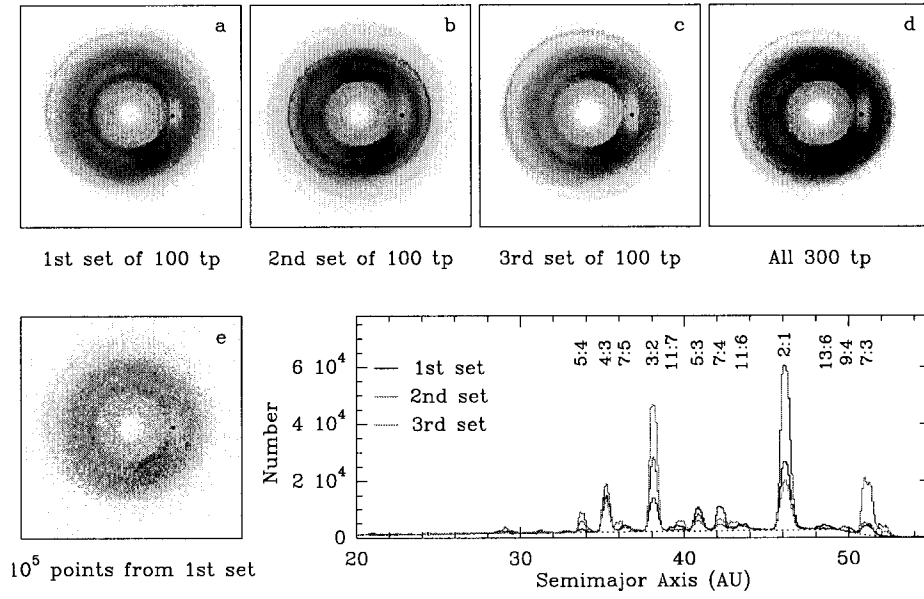


Figure 2.5: (a), (b) and (c) “Equilibrium” number density distributions for the three models I-A with $\beta=0.1$. (d) Number density distributions for the 300 particles together. (e) 10^5 randomly selected points from (a) indicating that a large number of particles is needed to resolve the structure. The dot indicates the position of Neptune. The histogram shows the relative occurrence of the different MMRs. The position of a few MMRs with Neptune are indicated in the figure.

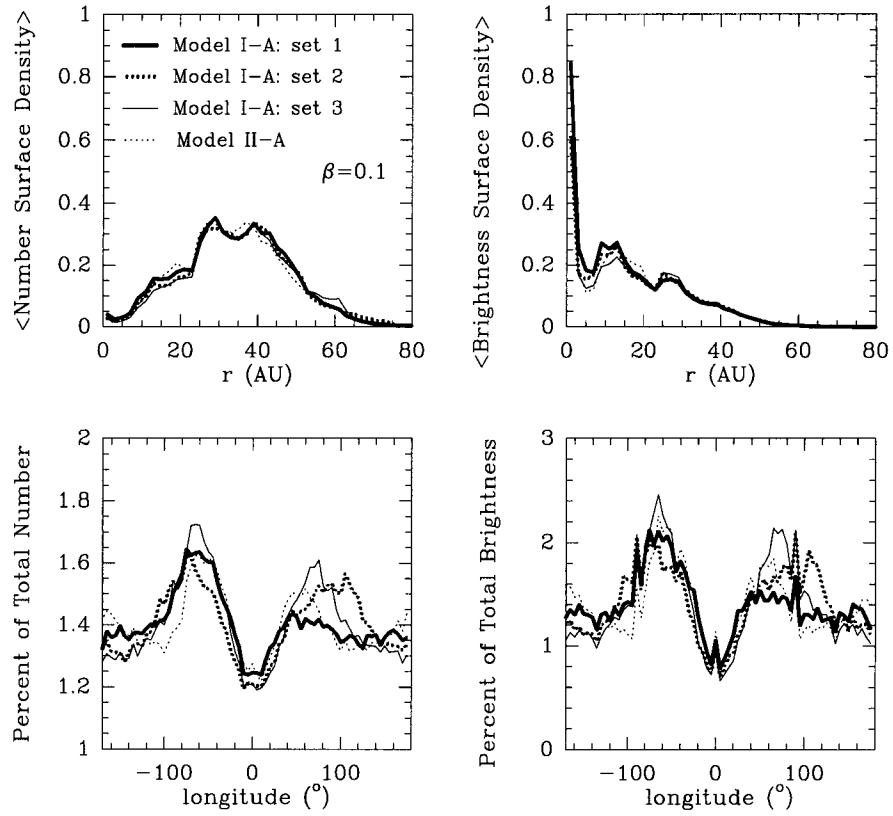


Figure 2.6: (top) Number and brightness density radial distributions, averaged over all θ , for particles with $\beta=0.1$. (bottom) Same as above but for angular distributions, integrated between 25 and 35 AU. The longitude is measured with respect to Neptune. The LZ99 approach is able to predict the radial structure, but the uncertainties in the azimuthal structure are large.

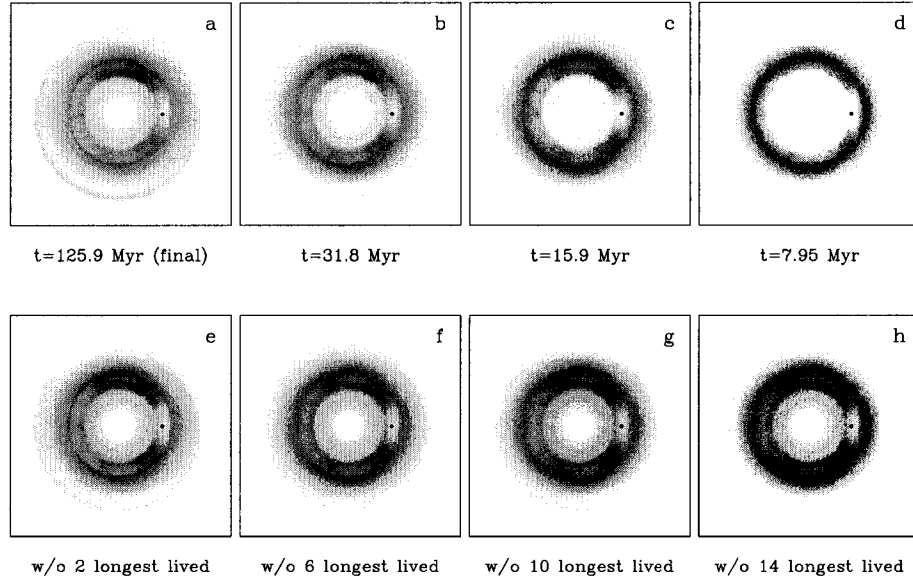


Figure 2.7: (top) Time scale in which structure is created: (a) Number density distribution for one of the models I-A with $\beta=0.1$ by the time the last particle leaves the system (125.9 Myr). (b), (c) and (d) show the structure seen at earlier and earlier times: 31.8, 15.9 and 7.95 Myr, respectively. (bottom) Effect of excluding the longest-lived particles: (e), (f), (g), (h) show the structure after excluding the contribution from the 2, 6, 10 and 14 longest-lived particles respectively. These results validate the use of LZ99 approach by indicating that the structure is created quickly and that the radial profiles of the number density distribution do not strongly depend on the contribution from the longest-lived particles. The dot indicates the position of Neptune.

between numerical results and analytical solutions to 2-body and restricted three-body cases, as well as comparison with other numerical results in the literature (LZD96, LZ99).

(2) We have carried out numerical simulations for single size particle disks in the presence and in the absence of planets in order to estimate the uncertainties inherent in the prediction of structure in the outer solar system debris disk, owing to the chaotic dynamics of dust orbital evolution. We simulate dust particle initial conditions according to the wider distribution of parent bodies indicated by the recent observed distribution of KBOs, and our simulations extend to larger particle sizes than previous studies.

(3) We find that the distribution of KB dust particle lifetimes in the Solar system are described as a sum of a gaussian and a nearly uniform distribution; the latter represents only a small fraction of all particles but extends to very long lifetimes, while the gaussian represents the dominant fraction of particles. The mean and dispersion of the gaussian component increases systematically with particle size, and is in the range of a few million years for 1–100 μm particle sizes. We do not find any correlations between the initial orbital elements and dynamical lifetimes of dust particles (see §3.2).

(4) We have examined carefully the method used by LZ99 to estimate the equilibrium spatial distribution of KB dust in the Solar System. This method is based on the ergodic assumption, so the dust structures obtained are determined to a large extent by the longest lived particles, which represent only a very small fraction of the dust population. The ergodic assumption is generally not applicable in chaotic dynamical systems. Nevertheless, we have established that in practice this method gives reliable results for several aspects of dust dynamical studies for three reasons: (i) the distribution of dust particle lifetimes is described as a sum of a gaussian plus a nearly uniform distribution, i.e. the longest-lived particles are not anomalous,

they are statistically representative of the long tail population; (ii) the dust spatial structure is created quickly; (iii) the radial profile of the equilibrium number density distribution does not strongly depend on the longest-lived particles (although the azimuthal structure does).

(5) We find that the azimuthal structure of the dust disk is not predictable in detail, except for a ‘gap’ near the outermost planet Neptune. This is because the azimuthal structure depends sensitively on the long lived particles trapped in mean motion resonances with Neptune, and the times of residence in the various resonances are highly variable and unpredictable.

CHAPTER 3

The Kuiper Belt Dust Disk: a Study Case of a Debris Disk with Giant Planets

3.1 Introduction

The results presented in Chapter 2 validate the use of our numerical approach for the modeling of the spatial density distribution of dust in debris disks harboring giant planets. In this chapter, we will apply this method to the Solar System Kuiper Belt dust disk. The Solar System, being filled with interplanetary dust and harboring giant planets, is an ideal case of study to investigate the effect of massive planets (Jupiter through Neptune) on the dynamics of the dust originating in an outer belt of planetesimals (the Kuiper Belt; KB).

The dust in the inner Solar System gives rise to the zodiacal light (observed by *Pioneer 10*, *IRAS* and *COBE*), and its dominant sources are debris from Jupiter family short period comets and asteroids (Liou et al., 1995; Dermott et al., 1992). The discovery of a debris disk around β -Pictoris, extending to 100s of AU, together with the confirmation of the existence of the theoretically predicted Kuiper Belt objects (KBOs) (Jewitt and Luu, 1995), suggest that significant dust production also occurs in the outer Solar System. This dust would spread throughout the Solar System due to P-R drag forming a dust disk that, if observed from afar, would be its brightest extended feature. Kuiper Belt Objects (KBOs) are icy bodies that lie in a disk beyond Neptune's orbit. It is estimated that there are about 10^5 objects with diameters greater than 100 km in the 30–50 AU annulus and a total population

roughly 3 orders of magnitude larger than that of the asteroid belt (Jewitt and Luu, 2000). The outer limit of the belt is presently not well determined but may be near 50 AU (Chiang and Brown, 1999; Allen et al., 2001). Dust production in the KB occurs due to mutual collisions of KBOs (Backman and Paresce, 1993; Backman et al., 1995; Stern, 1996) and to collisions with interstellar grains (Yamamoto and Mukai, 1998). Stern (1996) suggested that mutual collisions among KBOs can generate debris at a rate of $(0.0095\text{--}3.2)\times 10^{11} \text{ g s}^{-1}$. Using this estimate, Yamamoto and Mukai (1998) calculated a dust production rate of $(0.0086\text{--}2.9)\times 10^7 \text{ g s}^{-1}$ in particles smaller than $10 \mu\text{m}$. The impacts of interstellar dust on KBOs are also a significant source of interplanetary dust particles. Yamamoto and Mukai (1998) estimated that if there are $\sim 10^{13}$ KBOs of radius $\geq 0.1 \text{ km}$, the total dust production rate for particles smaller than $10 \mu\text{m}$ is $(0.37\text{--}2.4)\times 10^6 \text{ g s}^{-1}$ if the objects have hard icy surfaces, or $(0.85\text{--}3.1)\times 10^7 \text{ g s}^{-1}$ if the objects are covered with icy particles smaller than the interstellar grain impactors.

Detectors on board *Pioneer 10* and *11* have indeed been able to detect in situ dust in the outer solar system (Landgraf et al., 2002). Interstellar dust grains are estimated to contribute less than one percent to the measured flux, therefore this dust is thought to have a solar system origin. The dynamical signatures indicate that the dust detected between Jupiter and Saturn is due to short period external Jupiter family comets and short period Oort cloud comets. The dust detected beyond 10 AU (outside Saturn's orbit) is most likely produced by KBOs. If so, then a KB dust production rate of 2×10^{14} particles per second (for particles between 0.01 and 6 mm) is needed to explain the measured fluxes. Assuming a fragmentation power law for the size distribution, this corresponds to a dust production rate of $\sim 5\times 10^7 \text{ g s}^{-1}$, in agreement with the theoretical estimates above (Landgraf et al., 2002). The study of KB dust is of interest for several reasons: (1) it is a source of micrometeoroid impacts on outer Solar System bodies, and as such it could affect the giant planet atmospheric chemistry; (2) its contribution to the background radiation at long

wavelengths is important for Cosmology; (3) it is a source of anomalous cosmic rays; (4) it may enrich the local ISM with large particles (see Chapter 4); (5) it is a platform for organic chemistry in space; and it constitutes a hazard to fast-moving space probes traveling in the outer Solar System. There are several space missions planned for the future that will contribute in an important way to the understanding of KB dust. *HST*-ACS will carry out a survey to study with unprecedented detail the KBO population. *Cassini* dust detectors will study the mass, velocity and chemical composition of dust grains smaller than $10\ \mu\text{m}$ between 5–10 AU, while *New Horizons* and *InterStellar Probe* will provide data at larger distances (10–40 AU and 200 AU, respectively).

The study of hypervelocity micrometeoroid craters on lunar material and on the panels of the *Long Duration Exposure Facility* showed that Earth accretes about 3×10^7 kg of interplanetary dust particles (IDPs) every year (Grun et al., 1985; Love and Brownlee, 1993). Some of these particles are collected from the stratosphere by high-flying aircraft and are brought back to Earth for laboratory analysis. It is therefore very important to know their origin, as these studies can provide important information about the Solar System objects from where these dust particles originally came from. Is the KB a significant source of these accreted IDPs? Kortenkamp and Dermott (1998) (hereafter KD98) have calculated capture rates for IDPs of asteroidal and cometary origins. Based on these rates, and on the fact that the analysis of IDPs collected in the stratosphere shows a small diversity of chemical compositions (Flynn, 1995), they argue that the sources of IDPs are very limited and lie mainly in the asteroid belt, with less than 25% having cometary origin. KB dust particles were, however, not considered in their study.

The possibility that the KB may be a significant source of IDPs and the zodiacal cloud was first suggested by Liou et al. (1996). They found that (1) about 20% of KB dust particles are able to reach the inner solar system and (2) these particles have small eccentricities and inclinations (similar to asteroidal grains)

when they cross the orbit of the Earth, enhancing their chances of being captured and of surviving atmospheric entry. The significance of these results is that, as they explain, asteroids are certainly an important source of IDPs, but they can accrete material from only as far as ~ 4 AU and it is not clear that organic material at such distances can survive the T-Tauri wind of the young Sun. KB dust grains, on the other hand, can bring in unaltered primitive material from the outer solar system, so they could potentially be a source of the earliest organic material that gave rise to life on Earth. Comets could also bring material from the outer solar system, but as LZD96 argue, their high eccentricities and inclinations cause the released dust particles to be in highly eccentric and inclined orbits. This translates into high encounter velocities with Earth (>10 km/s), making it difficult for any organic material to survive atmospheric entry. In their paper, however, they do not actually calculate capture rates and entry velocities for KB dust grains, giving only qualitative estimates.

In this chapter, we are going to follow numerically, from source to sink, the evolution of several hundred of dust particles from the KB under the combined effects of solar gravity, solar radiation pressure, Poynting-Robertson (P-R) and solar wind drag, and the gravitational forces of 7 planets (excluding Mercury and Pluto). We consider particles of diameter 3–115 μm (assuming $\rho=1$ g/cm³; equivalently 1–40 μm for $\rho=2.7$ g/cm³). The different particle sizes are referred to in terms of their β value. The sinks of dust included in our numerical simulations are (1) ejection into unbound orbits, (2) accretion into the planets, and (3) orbital decay to less than 0.5 AU heliocentric distance.

§3.2 explains the distribution of parent bodies and the orbital evolution of dust. In §3.3 we discuss the formation of structure in the KB debris disk and its observational signatures. In §3.4, we present the radial density profiles derived from our models and the KB dust production rate from Landgraf et al. (2002); from these, we estimate the contribution of the KB dust to the zodiacal cloud. Assuming

steady state, this leads us to an estimate of the total mass in the KB dust disk. We also describe how the effects of radiation forces and the planets' perturbations change the particle size distributions. In §3.5, we address the question of the KB contribution to the collected IDPs on Earth by calculating geocentric encountering velocities and capture rates. In §3.6, we present the velocity field of the KB dust in the inner and outer solar system. In §3.7, we evaluate the magnitude of the Lorentz force, and the effect of dust destruction processes that are not included in our models. Finally, §3.8 summarizes our results.

3.2 Distribution of Parent Bodies and Orbital Evolution of Dust Particles

Our selection of the orbital elements of the parent bodies is based on published observations of KBOs and on recent studies of their debiased radial (Trujillo and Brown, 2001) and inclination distributions (Brown, 2001). Semimajor axes were uniformly distributed between 35 and 50 AU; eccentricities were derived from perihelion distances, with random values between 35 and 50 AU; inclinations were uniformly distributed between 0° and 17° , and the other three orbital elements, mean anomaly (M), longitude of ascending node (Ω) and argument of perihelion (ω), were randomly selected between 0 and 2π .

When dust particles are released from their parent bodies ($\beta=0$), their orbital elements instantaneously change due to the effect of radiation pressure that, as we saw in §2.2.2, makes the particle *feel* a less massive Sun by a factor $(1-\beta)$. Their new semimajor axis (a') and eccentricity (e') in terms of their parent bodies' (a and e) are given by

$$a' = a \frac{1 - \beta}{1 - 2a\beta/r} \quad (3.1)$$

$$e' = \left| 1 - \frac{(1 - 2a\beta/r)(1 - e^2)}{(1 - \beta^2)} \right|^{1/2}. \quad (3.2)$$

Figure 3.1 shows e and i for the parent bodies and the dust particles at the time of release.

In their slow journey toward the Sun, the particles cross MMRs with the giant planets. As a result, some particles get trapped and structure in the debris disk begins to form. As reported by LZ99, and also seen in our models, the exterior resonances with Neptune dominate the trapping. Usually, the particles escape the resonances via close encounters with the planet, but in the case of interior resonances, they can also escape due to the decrease of a , that makes the particle get farther away from the planet where drag forces dominate (Liou and Zook, 1997).

We have used the three models I-A with $\beta=0.1$ to study the existence of correlations in the initial orbital elements of the longest-lived particles. Figure 3.2 shows a , e , $\lambda-\lambda_{Neptune}$ and M for the 65 longest lived particles (solid lines; these particles have lifetimes $\geq 2 \times 10^7$ years; see Figure 2.4) compared to all the 300 particles in the models (dotted lines). There are two prominent features both readily understood: (1) As the particles are released, and due to their increased semimajor axis, their mean anomaly is such that they avoid aphelion, explaining the gap between 90° and 270° . (2) The longest-lived particles tend to have smaller initial eccentricities, as expected from the fact that they tend to be trapped more easily in resonances. We find no evidence of correlation between lifetime and initial orbital parameters.

3.3 Structure Formation: the Giant Planets Reshape the Debris Disk

Figure 3.3 shows the equilibrium semimajor axis distributions, Figures 3.4 and 3.5 show the equilibrium number density distributions in the presence and absence of planets, and Figure 3.6 shows the radial profiles averaged over all θ . The main features seen in these figures are: (1) the ring-like structure along Neptune's orbit,

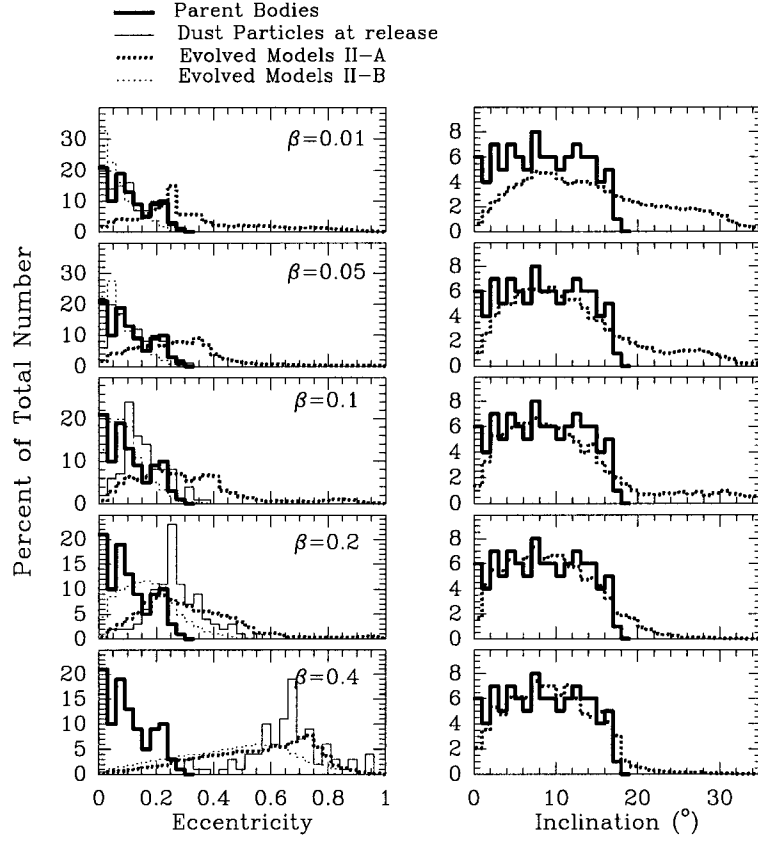


Figure 3.1: Distribution of eccentricities and inclinations for parent bodies (thick solid line), dust particles at the time of release (thin solid line), evolved dust particles in models II-A (thick dotted line) and evolved dust particles in models II-B (thin dotted line). The difference between the presence and non presence of planets is more dramatic for smaller β s. When planets are present, a fraction of the particles have their eccentricities and inclinations increased (due to trapping in $e - type$ and $i - type$ exterior resonances respectively). Radiation forces do not affect inclination, so the thick solid line, the thin solid line and the thin dotted line coincide.

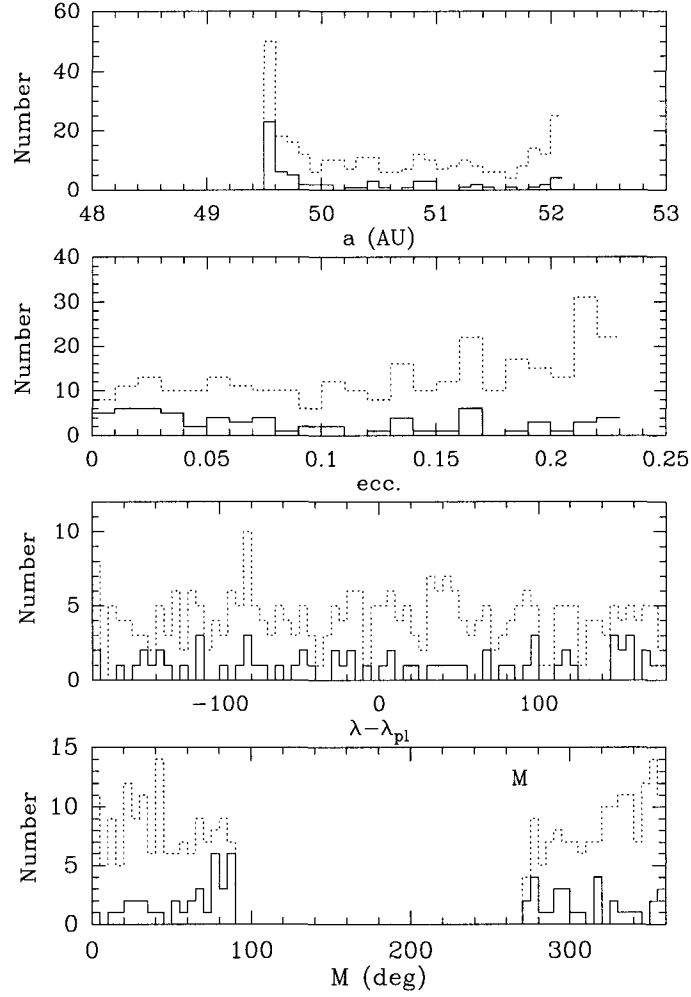


Figure 3.2: Initial orbital elements of the 65 longest-lived particles from the three models I-A with $\beta=0.1$ (solid line), compared with the total of 300 particles (dotted line). The longest-lived particles tend to have lower e . The gap between 90° and 270° is explained because upon release, due to the increased a , the particles avoid aphelion.

showing some azimuthal variation due to MMRs; (2) the minimum density at Neptune's position, as particles in MMRs tend to avoid the perturbing planet; (3) the clearing of dust from the inner 10 AU; and (4) the fact that the structure is more prominent for larger particles (smaller β s). The latter is because the trapping in MMRs is more efficient when the drag forces are small (LZ99). On the other hand, the ejection of particles from the inner 10 AU does not depend on size. The difference between models I-A and II-A in Figure 3.3 gives an estimate of the uncertainties, since the effect of the 3 terrestrial planets is negligible and the only difference is in the initial conditions of the parent bodies. The relative "strength" of the dominant MMRs depends quite strongly on the initial conditions (see also the histogram in Figure 2.5). This may indicate that the exact prediction of a planet's orbit, based on the identification of resonances, may be difficult. The ring-like structure in the number density is also visible in the brightness distributions of Figure 3.4, which were calculated assuming greybody absorption and emission by the dust grains in a $3 \times 10^{-11} M_{\odot}$ single size grain disk, at a distance of 30 pc. Additional features seen in the brightness distribution are: (1) a bright ring between 10 and 15 AU with a sharp inner edge, due to the ejection of particles by Saturn and Jupiter; and (2) a steep increase in brightness in the inner 5 AU. Both features are the combination of the decreasing particle density and increasing grain temperature closer to the Sun.

From the observational point of view, current IR detector technology does not allow us to spatially resolve many of these features. As an example, the *Spitzer* MIPS 24 μm detector has a spatial resolution of 5", which at the distance of β -Pictoris (16.4 pc) is about 80 AU. For *Spitzer* IRAC (3.6-8.0 μm) the resolution would be about 40 AU. The question is then how much information can be derived from the disk spectral energy distribution (SED). Figure 3.7 shows the composite SEDs that result from combining the SEDs from the $\beta=0.01, 0.05, 0.1, 0.2$ and 0.4 disks, with weights in such a way that they follow the power law distribution $n(b)db=n_0 b^{-3.5}db$, where b is the particle radius. The different lines correspond to

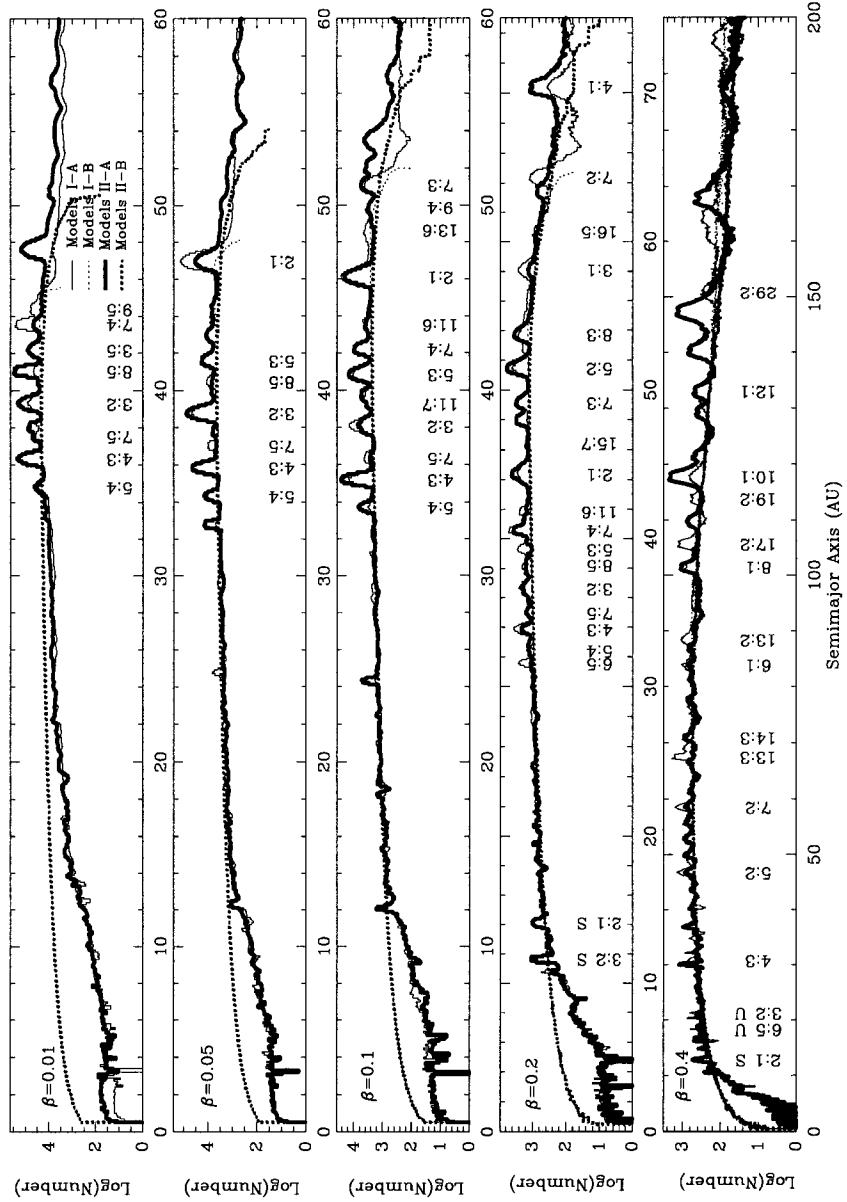


Figure 3.3: “Equilibrium” semimajor axis distribution in logarithmic scale for the particles in the models I-A (thin solid lines), models I-B (thin dotted lines), models II-A (thick solid lines) and models II-B (thick dotted lines). The trapping of particles in the exterior MMRs with Neptune and the depletion of particles in the inner 10 AU in the presence of planets are the most prominent features in the figure.

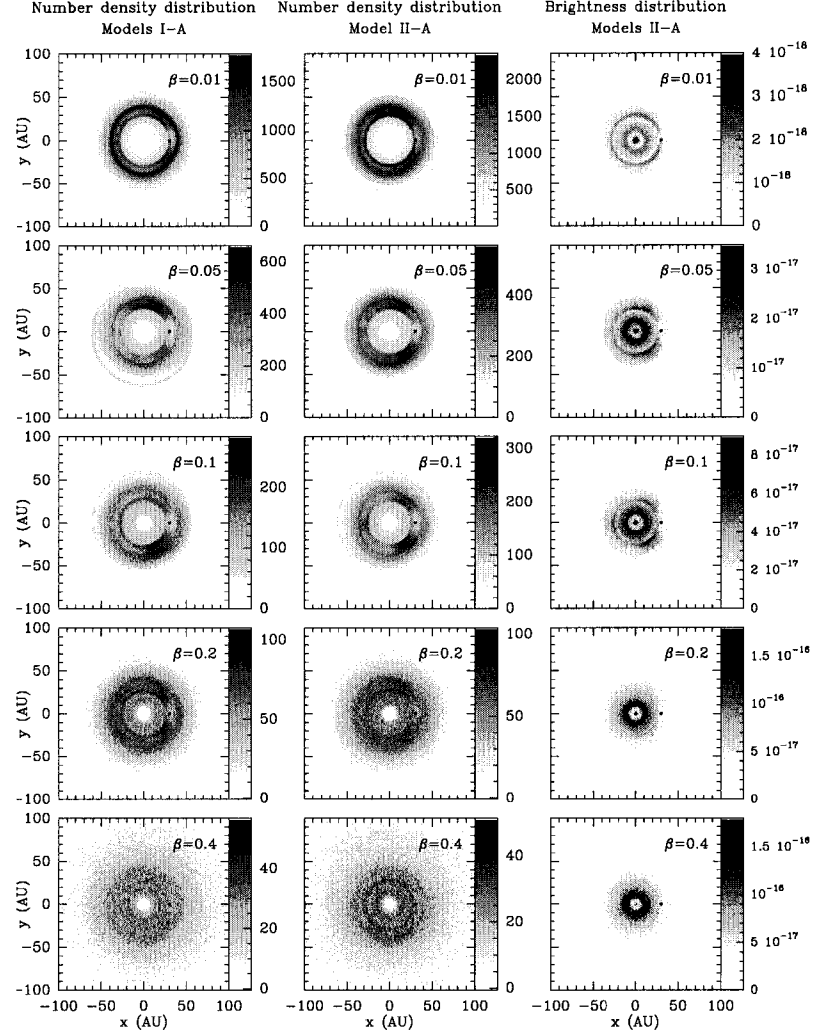


Figure 3.4: "Equilibrium" number density distribution for models I-A and II-A (columns 1 and 2) and brightness density distribution for model II-A (column 3). The brightness density is in units of $\text{ergs}^{-1}\text{cm}^{-2}(1\text{AU})^{-2}$ and corresponds to the thermal emission, integrated from 21.6 to 26.3 μm , of a $3 \times 10^{-11} M_{\odot}$ disk at a distance of 30 pc surrounding a $1 L_{\odot}$ star. Grain temperatures were calculated using the expressions in Backman and Paresce (1993) for the thermal equilibrium and emitted spectra of generic grains. Absorptive efficiency was assumed to be $\epsilon=1$ and emissive efficiency was $\epsilon=1$ for $\lambda < b$ and $\epsilon=b/\lambda$ for $\lambda > b$, where b is the grain radius. The dust particles have $\rho=2.7 \text{ gcm}^{-3}$. The dot at (30,0) indicates the position of Neptune.

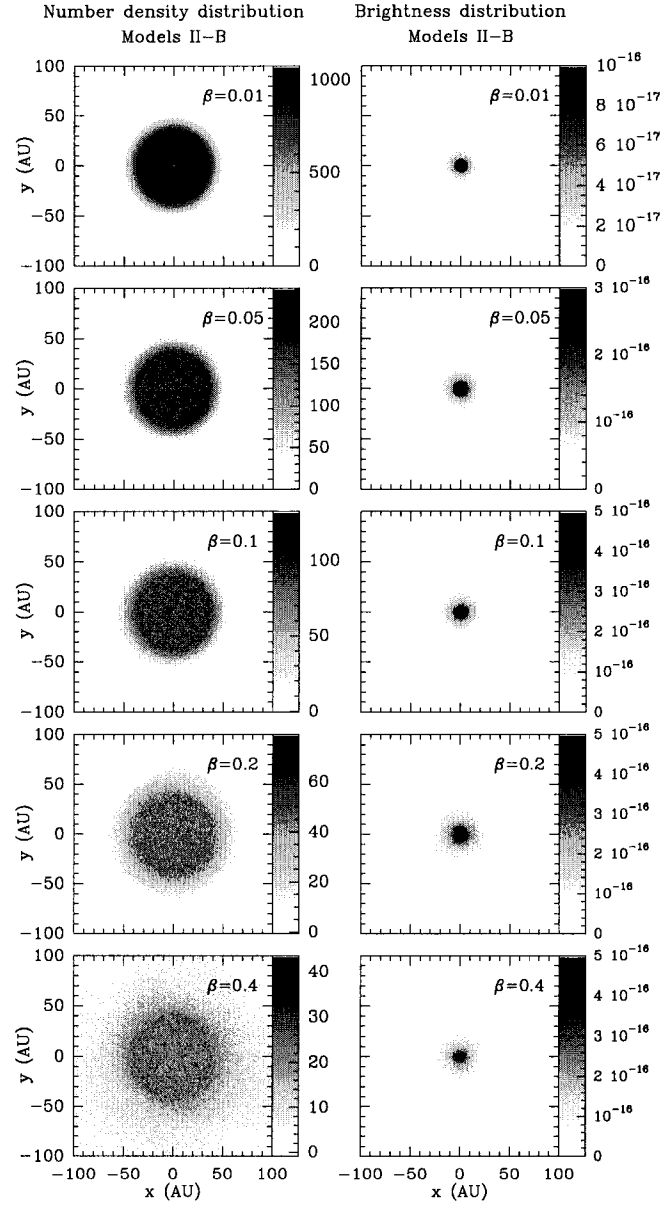


Figure 3.5: Same as Figure 3.4 but for the “equilibrium” number and brightness density distributions of models II-B.

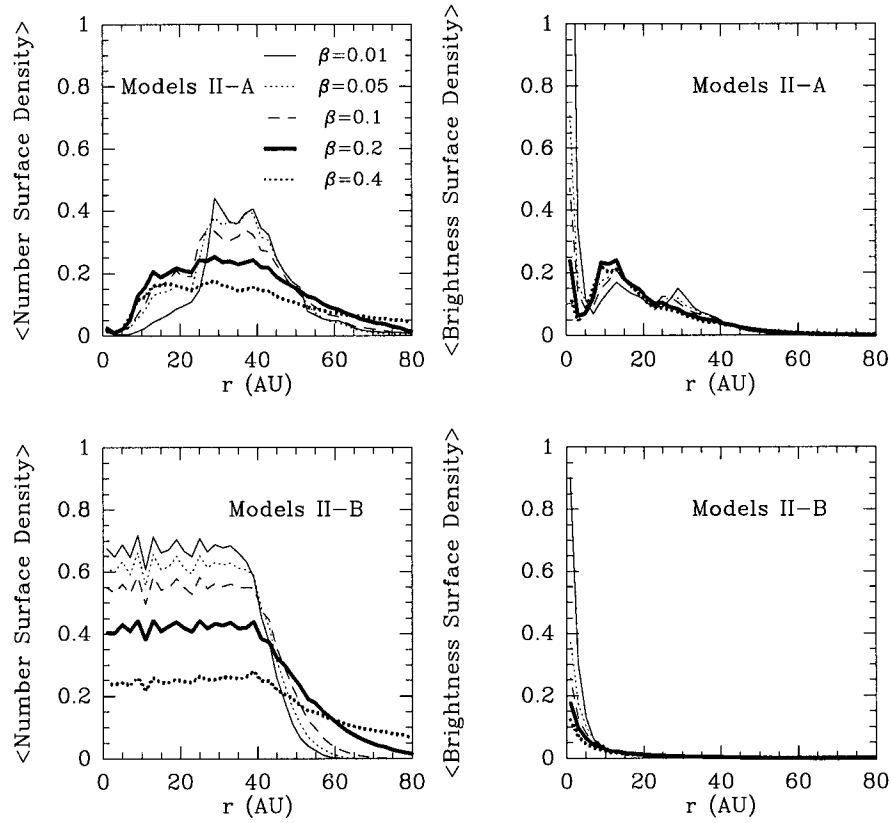


Figure 3.6: Number and brightness surface density radial distributions, averaged over all θ , for models II-A (top) and models II-B (bottom) shown in Figures 3.4 and 3.5. The main features are the depletion of particles in the inner 10 AU, due to scattering by Jupiter and Neptune, and the enhancement of particles from 30 to 50 AU, due to trapping in MMRs with Neptune.

the SEDs from a $3 \times 10^{-11} M_{\odot}$ disk only; and the Sun plus a disk with three different masses. In all cases, the solid line is for a system with 7 planets and the dotted line is for a system without planets. The wavelength labels correspond to the *Spitzer* MIPS and IRAC bands potentially useful to study these systems. We see that the presence of planets does modify the disk SED. The main modification is due to the clearing of dust in the inner region (an “inner gap”) by Jupiter and Saturn, which causes a significant deficit in the disk SED at higher frequencies. The density enhancement in the annulus between 35 and 50 AU, due to trapping in Neptune’s exterior MMRs, causes a relatively smaller effect on the shape of the disk SED. How well can one determine the masses and orbits of planetary perturbors from the shape of the disk SED? We plan to address this question in Chapter 5 by exploring in detail the parameter space of planetary masses and orbital elements.

It is important to note that our model systems (with and without planets) contain the same amount of disk mass. We are interested in how the structure created by the planets affects the shape of the SED, independent of the dust production rate. The latter determines only the normalization factor. However, planetary perturbations can affect the dust production rate, possibly leading to more massive dust disks. This effect is not taken into account in our models, but will be considered in the future.

3.4 Radial Distribution and Mass of the Kuiper Belt Dust Disk

Based on our models and on estimates of KB dust production rates, we can calculate the number density of dust in the KB and its mass. The simulations yield radial profiles of the number density of dust for various particle sizes; the production rates are used to get the normalization of these profiles. For the production rates in the KB, we use the observationally based estimate by Landgraf et al. (2002) of 2×10^{14} particles per second of radius between 0.01 and 6 mm. For the size distribution,

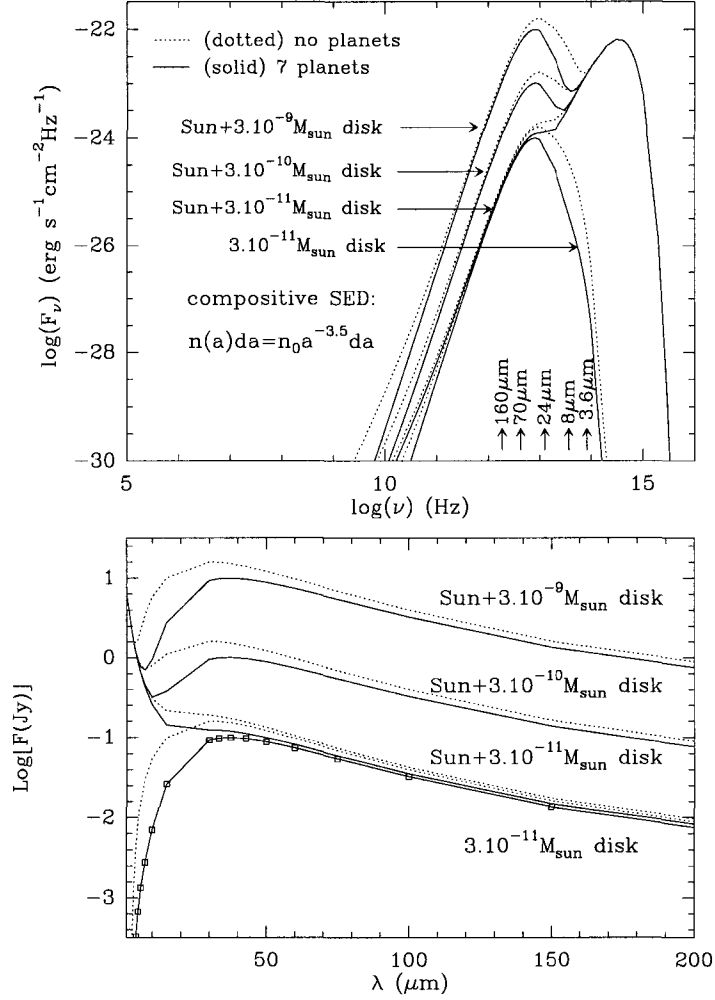


Figure 3.7: (top) Composite SEDs that result from combining the SEDs from the $\beta=0.01, 0.05, 0.1, 0.2$ and 0.4 disks, with weights in such a way that they follow the size distribution $n(b)db=n_0b^{-3.5}db$, where b is the particle radius. The different lines correspond to a $3 \times 10^{-11} M_{\odot}$ disk only; Sun + $3 \times 10^{-11} M_{\odot}$ disk; Sun + $3 \times 10^{-10} M_{\odot}$ disk; and Sun + $3 \times 10^{-9} M_{\odot}$ disk. In all cases, the solid line is for a system with 7 planets, the dotted line is for no planets and the system is at a distance of 30 pc. (bottom) Same as top but in Jy vs. μm . The squares correspond to the data points, indicating the spectral resolution on the synthetic SEDs.

we use a fragmentation power law, $n(b)db = n_0 b^{-q} db = n_0 b^{-3.5} db$, where b is the particle radius. (This corresponds to a generic grain mass distribution in collisional equilibrium; see, e.g., Dohnanyi (1969)). Then, assuming a bulk density $\rho=1$ g/cm³, we calculate the following dust production rates (in particles per second with the size bins in parentheses; the size corresponding to the particle's diameter): 4.5×10^{16} (2.1–4.2 μm ; $\beta=0.4$), 8.0×10^{15} (4.2–8.5 μm ; $\beta=0.2$), 1.4×10^{15} (8.5–17 μm ; $\beta=0.1$), 2.5×10^{14} (17–33.9 μm ; $\beta=0.05$) and 4.9×10^{12} (81.3–162.6 μm ; $\beta=0.01$). Because of the power law distribution, the size bins are chosen in such a way that they all have the same width in logarithmic scale; for each size bin, we have assigned a single β -value, as indicated (Liou and Zook, 1999).

3.4.1 Radial Distribution

The radial profiles of the number density of particles within 1 AU of the ecliptic, based on our dynamical models and normalized using the dust production rates and the size bins listed above, are shown in Figures 3.8*a* and 3.8*b*. In our models, the parent bodies are assumed to be distributed in orbits with semimajor axis and perihelion distances between 35 and 50 AU. Upon release, a dust particle has the same position and velocity as its parent body, but its orbital elements are different as a result of radiation pressure. The latter effectively causes the particle to feel a Sun less massive by a factor $(1-\beta)$. The larger the β , the more its orbit differs from its parent body's. After a particle leaves its parent body, P-R drag and solar wind drag tend to circularize and decrease the semimajor axis of its orbit, forcing particles to slowly drift in toward the central star (Burns et al., 1979). Assuming that the dust particles are being produced constantly, this drift creates a dust disk of wide radial extent. Figure 3.8*a* shows the radial distribution of particles of five different values of β in a fictitious KB disk unperturbed by planets.

The radial distribution changes in the presence of planets. We have modeled

the gravitational effects of seven of the planets, Venus through Neptune. Two effects play a major role in the quasi-steady state distribution of KB dust that we obtain in our models (see Fig. 3.8*b*):

1. *Gravitational resonances.*— The journey of the dust particles toward the central star is temporarily interrupted by the trapping of particles in Mean Motion Resonances (MMRs), mainly with the outermost planet, Neptune. The particles accumulate at certain semimajor axes, leading to the creation of structure in the disk; this explains the “bumps” that appear between 35 and 50 AU. The structure is more prominent for the smaller β -values because the resonance trapping is more efficient when the drag force is small.
2. *Gravitational scattering.*— Massive planets scatter and eject dust particles out of the planetary system, an effect that is independent of β . Scattering is responsible for the most striking difference between Figures 3.8*a* and 3.8*b*: for particles larger than the blow-out size ($\beta < 0.5$), the scattering of dust by the giant planets is able to extend the disk beyond the boundaries set by radiation effects alone. This has important consequences on the size distribution that will be explored below.

In Figure 3.8*c*, we show the radial profile of the total number density of particles with radius between 1.4 and 10 μm , compared to the *Voyager 1* number density estimate, inferred from dust impact rates of 1.4–10 μm particles from 30 to 51 AU (Gurnett et al., 1997; Jewitt and Luu, 2000). The radial profiles are obtained as follows: First, for each choice of particle bulk density ρ , we assign each β -value to a particle size bin (the size being the particle’s diameter). For $\rho = 1 \text{ g/cm}^3$, we define the following size bins: 2.8–4.2 μm ($\beta=0.4$); 4.2–8.5 μm ($\beta=0.2$), 8.5–17 μm ($\beta=0.1$) and 17–20 μm ($\beta=0.05$). For $\rho = 2.7 \text{ g/cm}^3$, the size bins are: 2.8–5.3 μm ($\beta=0.1$), 5.3–13.3 μm ($\beta=0.05$) and 13.3–20 μm ($\beta=0.01$). Next, we normalize the radial profile obtained from our numerical models for each of the values of β

(i.e., for the corresponding size bins) using the dust production rates from Landgraf et al. (2002) and assuming the power law size distribution stated above ($q=3.5$). As a final step, we add the contribution from all the size bins to obtain the total number density radial distribution shown in Figure 3.8c. The differences between the profiles for the two choices of ρ arise from the fact that the bulk density affects the correspondence between the β -value and the particle size, and the size in turn affects the estimate of the dust production rate because of the assumed power law in the size distribution. When comparing the modeled radial profiles with the *Voyager 1* estimate, one should keep in mind that there are uncertainties in the dust production rates and in the index of the power law (both of which determine the normalization factors of the models), as well as in the *Voyager 1* number density estimate (which is based on a few impact events and also has some uncertainty in the sizes of the particles detected). Nevertheless, the two modeled radial profiles are in good agreement with the *Voyager 1* observations. We cannot favor silicate over icy composition for KB particles based on this comparison.

3.4.2 Size Distribution

Radiation forces and planetary perturbations change the size distribution of dust particles, as the particles spread out from their site of production at rates that are dependent on their size. Figure 3.9 shows these effects in plots of the cumulative size distribution at various heliocentric distances throughout the KB dust disk. (The *cumulative* size distribution is calculated by integrating the *differential* size distribution obtained from our models in the size bins described above for $\rho=1$ g/cm³). As we mentioned, the initial differential size distribution at the time of dust production is assumed to be a power law with $q=3.5$; it is represented in Figure 3.9 as the thick line of slope -2.5, with the distance between the squares indicating our particle size binning “resolution”. The other lines represent the cumulative size distribution obtained in our models at five different heliocentric distances: 5, 21, 41,

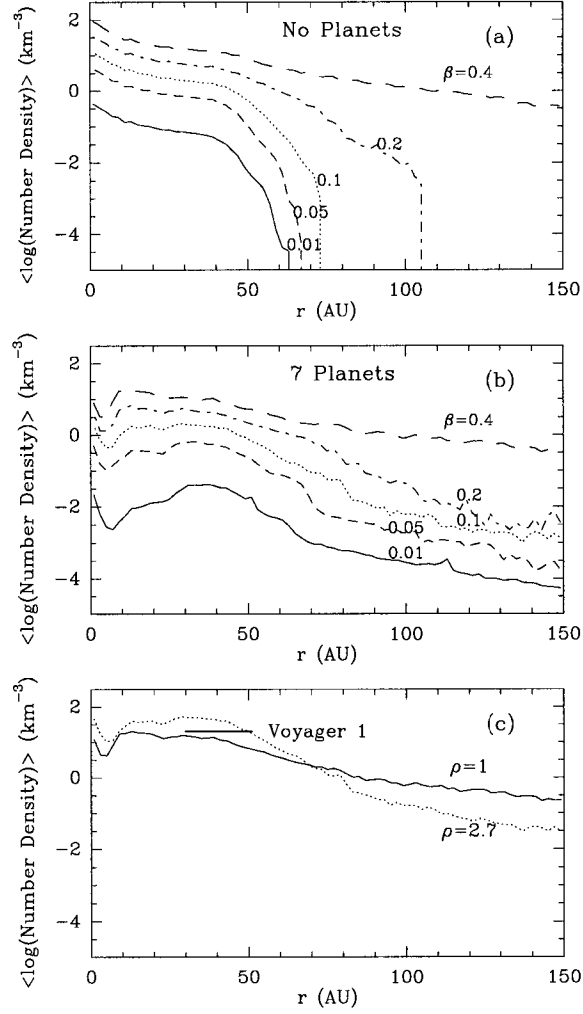


Figure 3.8: Radial profiles of the number density in the ecliptic for different values of β (labeled). The normalization is calculated using the dust production rates in (Landgraf et al., 2002), the size distribution $n(b)db = n_0 b^{-3.5} db$ and the size bins in § 3.4.1. The total number of particles used to create these profiles are as follows (for β of 0.01, 0.05, 0.1, 0.2 and 0.4, respectively): with planets, 552,787, 180,832, 112,885, 61,234 and 36,408; without planets: 1,107,811, 232,917, 125,398, 73,789 and 52,314. (a) A fictitious KB dust disk unperturbed by planets; (b) KB dust disk perturbed by 7 planets; (c) comparison between the *Voyager 1* number density estimate (*thick solid line*; from Jewitt and Luu (2000)) and a KB disk with 7 planets and two different particle bulk densities, for particle radius between 1.4 and 10 μm (see details in text).

81 and 141 AU, as indicated in the figure. Figure 3.9*a* shows results for a fictitious KB disk unperturbed by planets, while Figure 3.9*b* shows results for the KB dust disk perturbed by the seven planets, Venus through Neptune.

The main features are the following:

1. Radiation forces alone change the differential size distribution, from the original power law with $q = 3.5$, to another power law of smaller index (see Fig. 3.9*a*). This is due to the fact that radiation pressure “kicks out” the smaller particles preferentially and P-R drag spreads out the smaller particles faster than the bigger ones.
2. This shallower power law (with slope of ~ -1.5 , corresponding to a differential power law index $q \sim 2.5$) is maintained constant throughout the disk at distances smaller than the aphelion of the parent bodies (parallel dotted, dashed and solid lines in Fig. 3.9*a*). At larger distances, however, we start to encounter the disk boundaries set by radiation pressure, which depend on the particle sizes. This explains the steeper size distributions found at 81 and 141 AU (only the smaller particles reach those larger distances).
3. In the presence of planets, the size distribution changes greatly at distances larger than the aphelion of the parent bodies: compare the shallower slopes obtained at 141 AU and 81 AU in Figure 3.9*b*, with the steep slopes at the same distances in Figure 3.9*a*. Unlike radiation pressure, gravitational scattering by the giant planets can send larger particles to these larger distances, effectively spreading all the dust widely. As the figure shows, the dust distribution is no longer described by a power law with a single index.
4. The trapping of particles in MMRs with Neptune (between 35 and 50 AU), and the fact that large particles are more easily trapped, explains why the slope of the size distribution becomes more shallow at 41 AU (slope about

-1.5, $q \sim 2.5$) than at 5 and 21 AU (slope about -1.9, $q \sim 2.9$) (compare solid and dashed lines with dotted line in Fig. 3.9b).

Although some of these effects are minor, the large change in the size distribution described in point 3 is very significant. It is clear that the detection of an exoplanetary dust disk of wide radial extent (a hundred to thousands of AU) does not necessarily imply the presence of dust-producing planetesimals at such large distances: gravitational scattering by giant planets can spread the dust to distances much larger than the aphelion of the parent bodies. The obvious question is whether this effect could be used to unambiguously infer the presence of giant planets. We plan to address this question in the future by studying the effect that the change in the particle size distribution has on the disk's spectral energy distribution.

3.4.3 Total Dust Mass

From our models, we estimate the total mass of the KB dust disk to be, $m_{KB \text{ dust}} \sim 1.2 \times 10^{-11} M_{\odot}$ for particles with diameter 2.4–160 μm (assuming $\rho = 1 \text{ g/cm}^3$), or $m_{KB \text{ dust}} \sim 4.2 \times 10^{-11} M_{\odot}$ for particle with diameter 0.8–150 μm (for $\rho = 2.7 \text{ g/cm}^3$). Using COBE observations at 140 and 240 μm , Backman et al. (1995) set an upper limit for the total mass of dust in the KB of $\sim 3 \times 10^{-10} M_{\odot}$. Jewitt and Luu (2000) calculated that the mass in particles with radius 1.4–10 μm to be $\sim 4 \times 10^{-14} M_{\odot}$, based on a simple estimate using the *Voyager 1* number density; the volume of an annulus with 30 AU inner radius, 50 AU outer radius, and 10 AU thickness; and the assumption of an average grain mass of $2 \times 10^{-14} \text{ kg}$. For this size range, and using the same size bins used for Figure 3.8c, our models predict a mass of $5.2 \times 10^{-13} M_{\odot}$ (for $\rho = 1.0 \text{ g/cm}^3$), or $5.5 \times 10^{-12} M_{\odot}$ (for $\rho = 2.7 \text{ g/cm}^3$).

The uncertainties in the derived $m_{KB \text{ dust}}$ come not only from the dust production rates, but also from the fact that we are extrapolating the results from only five β -values to a wide range of particle sizes. To estimate $m_{KB \text{ dust}}$, we do

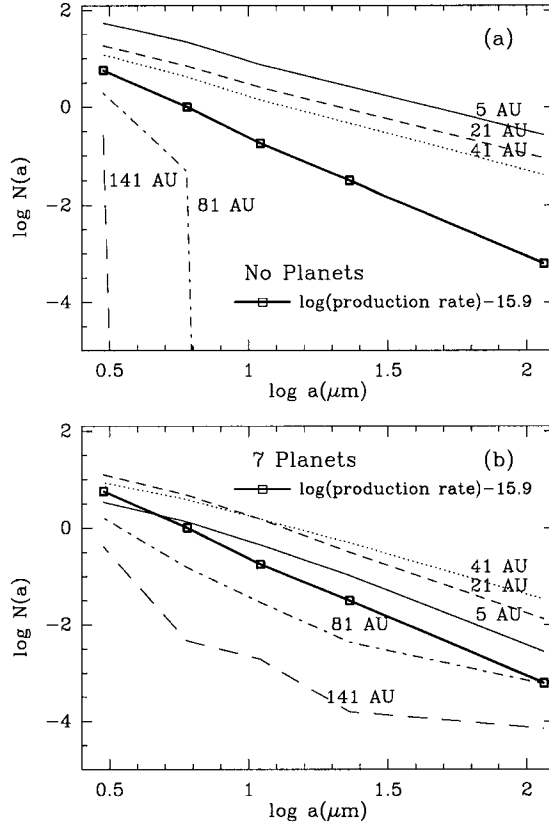


Figure 3.9: Effect of radiation forces and the presence of planets on the cumulative size distribution (size bins in § 3.4.1). The thick solid line shows the size distributions at the time of dust production by the parent bodies in units of number of particles per second. To fit in the figure, the line has been displaced by -15.9 dex. The slope of the cumulative distribution is -2.5, corresponding to a differential size distribution of index -3.5. The distance between the squares indicates the particle size binning “resolution”. The rest of the lines are the number density of particles in the ecliptic (in km^{-3}) at five different distances (indicated in the figure). (a) A fictitious KB dust disk unperturbed by planets; (b) KB dust disk perturbed by 7 planets.

the following: (1) We count the number of particles present in our five “steady state” models, each corresponding to a different β . The models assume an artificial dust production rate of 100 particles every 1000 years (see Chapter 2). (2) We multiply the number of particles by the ratio of the dust production rates derived from Landgraf et al. (2002) (in the size bins corresponding to the values of β under consideration), to our artificial dust production rate. This gives us the total number of particles in each of the five size bins. (3) To convert this number into mass, one must multiply by the particle mass. The particle mass that we attribute to each size bin is calculated using the fragmentation power law, so that the small particles have more weight because they are more abundant. (If we were to use the mass of the particle that lies in the middle of the bin [corresponding to the modeled β], our total dust masses would be about 4.5 times larger). (4) Finally, we add together the masses from the five different size bins. This results in the values of $m_{KB\ dust}$ quoted above.

3.5 Is the Kuiper Belt a Significant Source of Interplanetary Dust Particles?

We have calculated Earth’s capture rates and entry velocities for KB dust grains based upon our numerical models, and adopting the procedure of KD98. We find that (1) KB dust grains have higher eccentricities when crossing the orbit of the Earth than those found by LZD96 and (2) their encounter velocities and capture rates are more similar to dust grains of cometary origin than to asteroidal origin; this is contrary to the results of LZD96.

We define a particle to be Earth crossing if its orbit overlaps that of Earth, that is, $q < R < Q$, where $q = a(1-e)$ is the perihelion of the particle, $Q = a(1+e)$ is its aphelion and R is the heliocentric distance of Earth, $0.9833 \text{ AU} < R < 1.0167 \text{ AU}$. The encounter velocity v_0 between the Earth and a particle on a crossing orbit was

calculated following Kessler (Kessler, 1981). The effective capture cross-section σ_c is given by $\sigma_c = \sigma_{Earth}(1 + v_e^2/v_0^2)$, where v_e is the escape velocity from the Earth (at an altitude of 100 km, $v_e = 11.1 \text{ km s}^{-1}$) and σ_{Earth} is Earth's geometric cross section. The average spatial density at heliocentric distance R and ecliptic latitude l of a population of dust particles with orbital elements a , e and i is given by

$$S(R, l) = \frac{1}{2\pi^3 R a [(\sin^2 i - \sin^2 l)(R - q)(Q - R)]^{1/2}}. \quad (3.3)$$

The fraction of this population captured by the Earth at position (R, l) per unit time is $p = v_0 \sigma_c S(R, l)$. Following KD98, for each of the Earth-crossing particles in our models we have calculated $S(R, l)$ at 360 positions along Earth's orbit, with R and l uniformly distributed in the range $0.9833 \text{ AU} < R < 1.0167 \text{ AU}$ and $-0^\circ.00035 < l < 0^\circ.00035$. Table 3.1 shows the results after averaging over these 360 positions and over the whole population of Earth-crossing particles. For comparison, the results from KD98 for asteroidal and cometary dust (with $\beta = 0.0469$) are also included.

As Figure 3.10 shows, we find high eccentricities for KB dust grains, similar indeed to cometary dust and not to asteroidal dust, which implies a low spatial density and high encounter velocity, and, therefore, a low capture rate (see Table 3.1). The asteroidal dust particles, on the other hand, have lower eccentricities and inclinations, which translates into a higher capture rate. The discrepancies with LZD96 probably arise from the different criterion used to identify particles on Earth-crossing orbits; LZD96's criterion, $a < 1$, which is less precise than the one we adopt here, has a strong bias toward low-eccentricity orbits.

In order to estimate the relative contributions of various sources to the IDPs captured at Earth from the relative capture rates in Table 3.1 (which depends only on the orbital elements of the population of Earth-crossing particles), we need to know the relative contribution of each source to the number density of particles on Earth-crossing orbits. This problem has yet to be solved because the actual dust production rates from asteroids, comets and KBOs are highly uncertain and very

Table 3.1: Earth-crossing dust grains.

NOTE.—Earth orbital elements: $a=1$ AU, $e=0.0167$, $i=0.00035^\circ$. a : Approximate values from KD98 Fig.24, 25 (for $\beta=0.0469$ and a ratio of solar wind to P-R drag $sw=0.3$). b : Previously trapped and non-trapped in MMR with Jupiter.

Source	Average Capture Rate (Gyr^{-1})	Geocentric Encountering Velocity (km s^{-1})
Kuiper Belt:		
$\beta=0.01$	10.9	13.4
$\beta=0.05$	10.2	13.3
$\beta=0.1$	14.5	12.1
$\beta=0.2$	14.7	12.4
$\beta=0.4$	9.3	18.0
Asteroids ^a :		
Eos	100	5
Themis	390	4
Koronis	660	3
Other	170	6
Comets ^a		
Trapped ^b	35	11
Non-trapped ^b	5	17

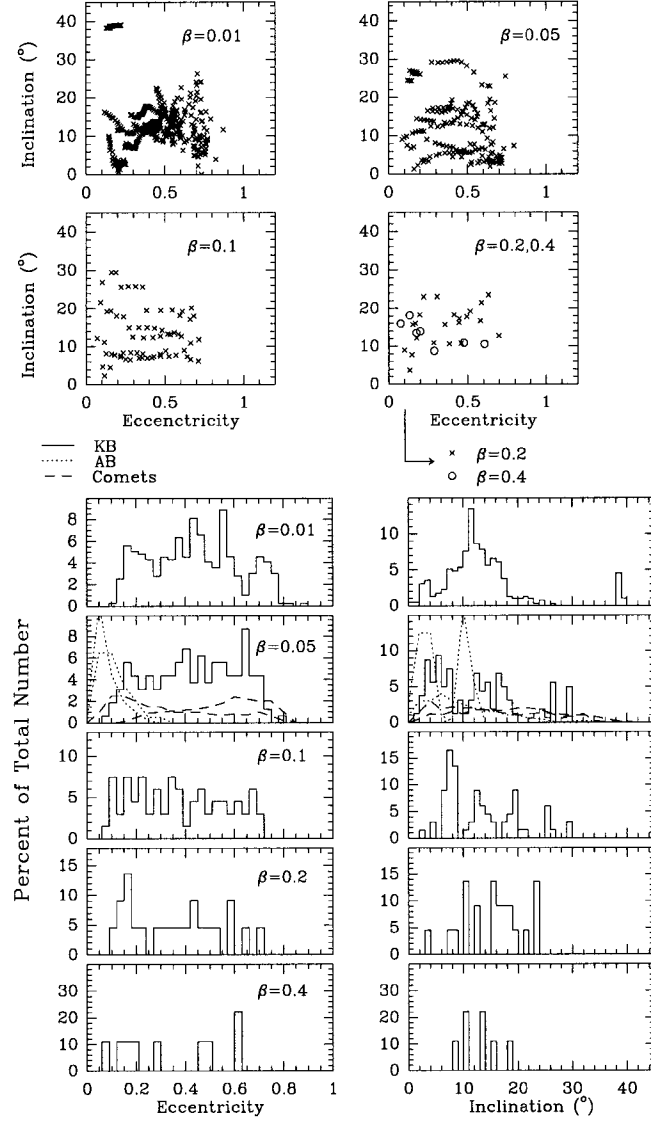


Figure 3.10: Eccentricities and inclinations of dust grains in Earth-crossing orbits. For comparison, and in a different scale, the $\beta=0.05$ histograms show the distribution of eccentricities and inclination calculated by KD98 for dust particles with $\beta=0.0469$, whose parent bodies are the asteroid families Eos, Themis and Koronis, and the non-family asteroids (*dotted lines*) and the comets (*dashed lines*). The eccentricities and inclinations of the Earth-crossing KB dust grains are very different from those of the asteroidal dust, more resembling the distributions of cometary dust.

model dependent. Since cometary and KB dust grains have similar capture rates, we can extend the results of KD98 to predict that cometary plus KB dust can represent more than half of the IDPs captured by Earth only if comets and KBOs together supply $\sim 95\%$ of the Earth-crossing particles. Based on modeling of the IRAS dust bands, KD98 estimated that (5–25)% of the Earth-crossing particles originate in the asteroid families Eos, Themis and Koronis. Using Dermott et al. (1994) 1:3 ratio of dust produced by asteroid families to that produced by all asteroids, we then have that all asteroids contribute (15–75)%, leaving the rest for comets and KBOs. In the extreme case that as much as 85% has cometary or KBO origin, this suggests that because of the lower capture rates of these highly eccentric grains, only 25% of the collected IDPs will be supplied by comets and KBOs. Interestingly, Brownlee et al. (1994) concluded that, based upon the maximum temperature reached during atmospheric entry from the study of helium release, about 20% of IDPs $< 10 \mu\text{m}$ have entry velocities typical of cometary IDPs (see Figure 3.11 for an example). This is in agreement with the above estimate. In the other extreme case, where 25% of IDPs have cometary or KBO origin, our models, together with KD98's results, suggest that they will represent only about 2% of the collected IDPs. Our conclusion from this exercise is that the KB can certainly be a source of IDPs but it is not as important as predicted by LZD96.

The estimates above are for the relative contributions from the different sources to the collected IDPs and depend on their relative contribution to the number density of particles on Earth-crossing orbits. We can also calculate the absolute contribution from the KB by using Landgraf et al. (2002) dust production rates and the capture rates in Table 3.1. Our models, together with the dust production rates, yield the number of particles on Earth-crossing orbits. The capture rates are the fraction of this population that is captured by Earth every 10^9 yr. The multiplication of these two numbers leads to the following results: $1.2 \times 10^5 \text{ kg yr}^{-1}$ (2.4–160 μm , $\rho=1 \text{ g cm}^{-3}$), or $4.1 \times 10^5 \text{ kg yr}^{-1}$ (0.8–150 μm , $\rho=2.7 \text{ g cm}^{-3}$). These

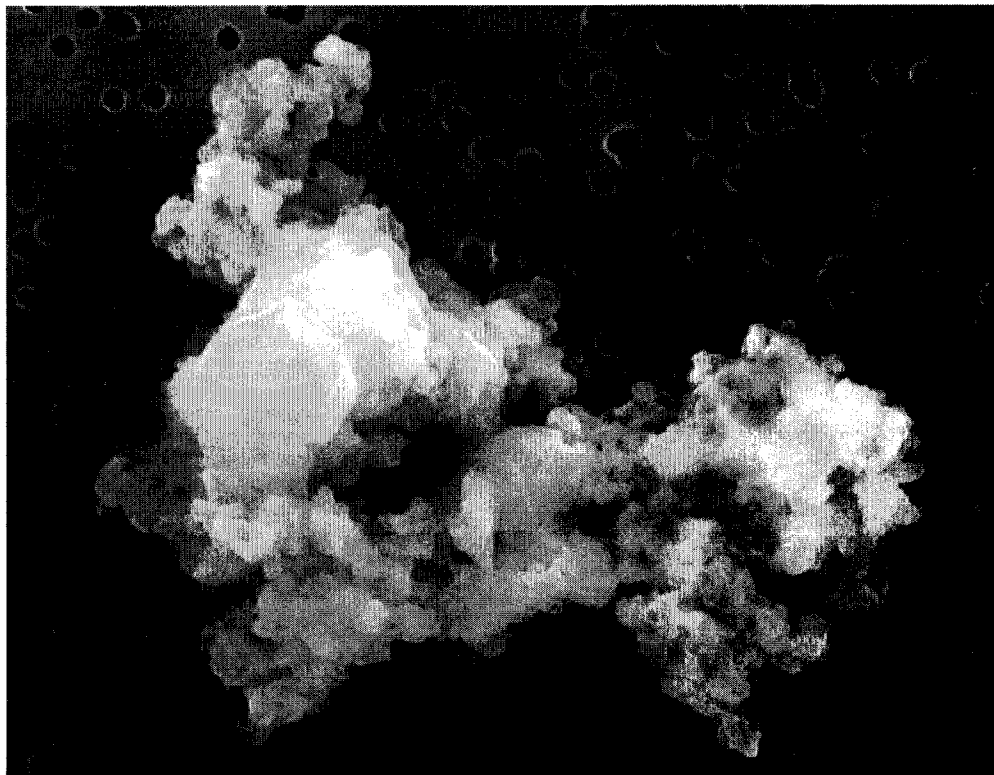


Figure 3.11: Example of 10 μm IDP collected in the Earth's stratosphere. It has high carbon and volatile abundances and high porosity, indicating probably a cometary origin.

numbers should be compared to the total mass influx of $3 \times 10^7 \text{ kg yr}^{-1}$ inferred from the microcraters on the *Long Duration Exposure Facility* (Love and Brownlee, 1993). The microcraters correspond to particles of radius between 2.5 and 250 μm , and show a peak and a cutoff in the particle size distribution near 100 μm . The accreted KB dust mass represents between 0.4% (assuming $\rho=1 \text{ g cm}^{-3}$) and 1.4% (assuming $\rho=2.7 \text{ g cm}^{-3}$) of this total mass influx. The same uncertainties in the dust mass estimates mentioned in §3.4.3 apply here —namely, if we were to use the mass of the particle that lies in the middle of each bin instead of weighting the mass using the power law, the values would be 4.5 times larger. Also, because most of the mass is contained in the large particle sizes, these results depend on the maximum particle radius chosen. The conclusion, however, is clear: if Landgraf et al. (2002) KB dust production rates are correct, then the KB presently provides only a few percent of the collected IDPs.

The delivery rate of KB dust to Earth's vicinity is calculated using the dust production rates in §3.4 and the percentage of particles that is able to drift all the way into the Sun, which, as seen in Table 3.2, is also a function of β . The delivery rates are (expressed in particles per second, followed by the bin sizes in parentheses) 4.9×10^{15} (2.1–4.2 μm), 1.2×10^{15} (4.2–8.5 μm), 2.9×10^{14} (8.5–17 μm), 4.7×10^{13} (17–33.9 μm) and 5.4×10^{11} (81.3–162.6 μm). One should keep in mind, however, that these estimates, and the ones in §§ 3.4 and 3.6, are rather model-dependent: the Landgraf et al. (2002) dust production rate estimate makes assumptions about the KB parent bodies' orbits that are significantly different from the observed distribution; they also assume that there is no source of dust in the 10–30 AU region, and we have neglected the destruction of dust grains due to interstellar and mutual collisions.

Table 3.2: Final fate of Kuiper Belt dust grains.

NOTE.—Listed as percentages; Liou et al. 1996 results appear in parentheses.

 a : Planet of last encounter.

Result	$\beta=0.01$	$\beta=0.05$	$\beta=0.1$	$\beta=0.2$	$\beta=0.4$
Ejected ^a :					
Jupiter	32	38 (45)	44 (35)	40 (35)	20 (45)
Saturn	37	28 (30)	23 (40)	31 (40)	32 (35)
Uranus	5	8 (0)	6 (0)	6 (0)	13 (0)
Neptune	13	4 (0)	3 (5)	8 (5)	21 (5)
None					3
Drift in	11	19 (25)	21 (20)	15 (20)	11 (15)
Hit planet:					
Jupiter	1	1 (0)	1 (0)		
Saturn	1	2 (0)	1 (0)		
Uranus			1 (0)		

3.6 Velocities of Kuiper Belt Dust Grains

A study of the velocity field of KB dust is useful for predicting the flux of particles colliding with a spacecraft exploring the outer solar system (e.g. *New Horizons* and *Interstellar Probe*).¹ This is of interest for planning dust detectors or dust analyzers, as well as for estimating the potential hazard posed by dust collisions to fast-moving spacecraft. In order to provide some general estimates, we have used our models to calculate the non-circular velocity of the KB dust in the ecliptic: for each particle, the instantaneous circular velocity at that distance has been calculated and has been subtracted from its actual velocity. The resulting magnitude of non-circular velocities in the ecliptic presented in Figure 3.12 corresponds to the average values of the particles that lie in square cells of 1 AU in size. We find no significant azimuthal structure, except for the following: between 25 and 35 AU, the non-circular velocities show a small systematic azimuthal variation at the level of 10–20%, with a maximum at Neptune’s position, which may be due to the fact that the particles trapped in MMRs tend to avoid the planet in the resonance. Figure 3.13 shows the radial profile of the ratio between the non-circular and the circular velocity averaged over azimuth. The increase of the fractional non-circular velocity for heliocentric distances $r > 50$ AU is due to the fact that only particles of large eccentricities are to be found at distances beyond the parent bodies. The non-circular velocities tend to be higher for smaller particles (larger β), as expected from their larger eccentricities upon release.

3.7 Other Physical Processes

Our models do not include the effect of magnetic fields on charged dust grains and the dust grain destruction processes (such as sublimation, sputtering and collisions).

¹<http://pluto.jhuapl.edu/> and <http://interstellar.jpl.nasa.gov/>

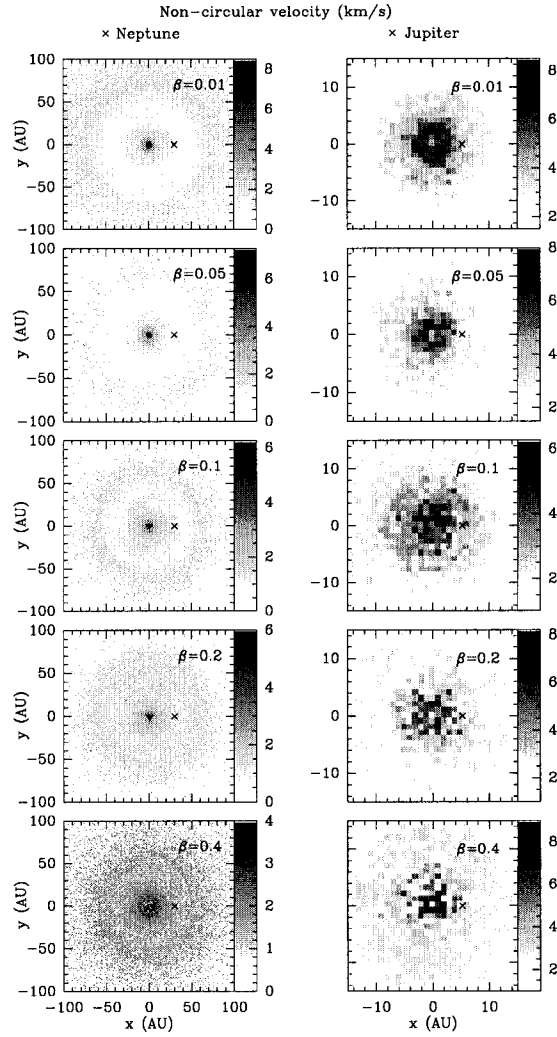


Figure 3.12: Non-circular velocity field (km s^{-1}) in the ecliptic for different particle sizes. The crosses indicate the position of Neptune (*left*) and Jupiter (*right*).

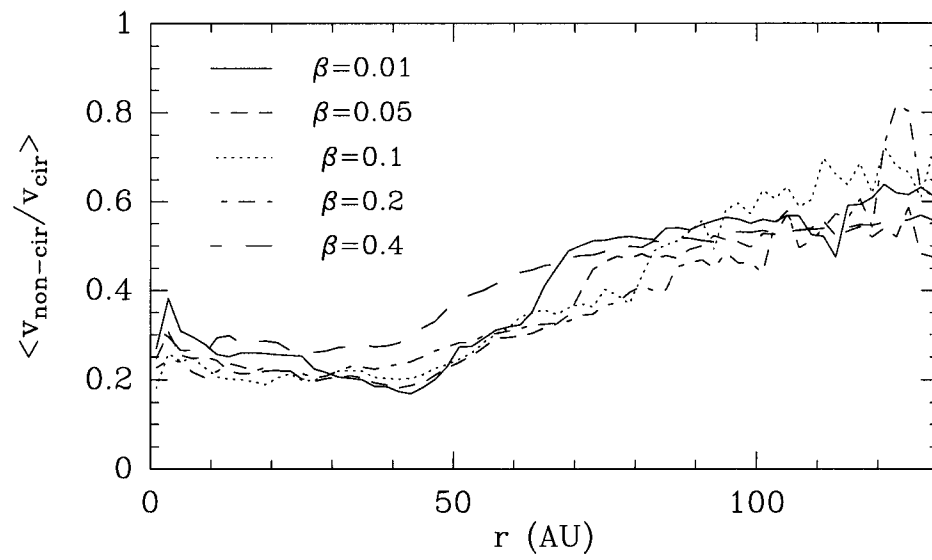


Figure 3.13: Radial profiles of the ratio between the non-circular and the circular velocity for different values of β .

Below, we briefly comment on how this may affect the results presented here, but a comprehensive evaluation of these processes is beyond the scope of this thesis.

3.7.1 Effect of Heliospheric Magnetic Fields

Dust grains are generally electrically charged, as a result of the ejection of photoelectrons and the accretion of ions and electrons. Inside the heliosphere, < 150 AU, the grains are therefore subject to the Lorentz force exerted by the interplanetary magnetic field, while outside the heliosphere the interstellar magnetic field dominates. The effects of solar wind magnetic forces on charged dust grains have been discussed previously (Parker, 1964; Consolmagno, 1979; Morfill and Grun, 1979; Mukai, 1985; Gustafson, 1994; Fahr et al., 1995; Grun and Svestka, 1996). Here we summarize the lines of argument that lead us to conclude that the omission of Lorentz forces in our modeling is not a significant limitation of our results.

The interplanetary magnetic field is known to have a complex structure and time behavior. The dipole component changes polarity every 11 years, with the 22 year solar cycle. Moreover, near the ecliptic these sign reversals take place more rapidly because of the presence of the heliospheric current sheet, the extension of the Sun's magnetic equator into interplanetary space, separating regions of opposite polarity. At solar minimum, the current sheet extends from approximately -25° to 25° from the solar equator. Particles within this latitude range cross the current sheet at least twice every solar rotation (~ 27 days), or four or even six times if the current sheet is wrapped because of higher order terms in the magnetic field (Balogh, 1996). At higher ecliptic latitudes, the particles cross the current sheet at least twice as they orbit the Sun. Therefore, the time-averaged effect of the Lorentz force will tend to vanish within a particle's orbital period, because the sign reversals are significantly faster than the orbital period of most KB particles. (We note that 80–90% of the KB dust grains are ejected by the giant planets [see Table 3.2], and

therefore their orbital periods during their lifetimes are generally much larger than the 11.8 year period of the innermost giant planet, Jupiter. However, we cannot rule out resonant effects for charged grains that remain in the vicinity of Jupiter and Saturn for extended periods of time, as they may be subject to Lorentz forces of period comparable to their orbital periods.)

Parker (1964) was the first to study the effect of this fluctuating interplanetary field on dust grains on non-inclined, circular orbits. Because the dominant component of the field is perpendicular to the radial solar wind vector, with a magnitude $\sim 3 \times 10^{-5}/r(\text{AU})$ gauss for heliocentric distances r exceeding a few AU (Parker (1963), p. 138), he concluded that the Lorentz force will scatter the grains out of the ecliptic plane, by perturbing the particle's inclinations while keeping the energy of the orbit unchanged. At the distance of the Earth, the scattering would be important only for grains $<1 \mu\text{m}$, for which the inclinations change significantly before P-R drag sweeps them into the Sun. More recently, Fahr et al. (1995) estimated that the inclination change causes a negligible evolutionary effect on zodiacal dust particles $>10 \mu\text{m}$. They found that for particles with inclinations $i < 15^\circ$, where the bulk of the dust particles considered in this paper are, this effect is completely negligible compared to P-R migration rates because of the stochastic character of the electromagnetic force near the current sheet; for $i > 15^\circ$ and circular or quasi-circular orbits, the Lorentz force exactly cancels out when integrated over a complete orbit, whereas for more eccentric orbits, the orbit-averaged change in inclination turns out to be very small because the Lorentz force reverses every 11 years with the solar cycle.

But as Parker (1964) pointed out, in reality, the interplanetary field also fluctuates in the direction perpendicular to the ecliptic. These fluctuations cause a random walk in the semimajor axis of the particles. Over a period of time Δt , the P-R effect will dominate over Lorentz scattering provided that $\langle \Delta a \rangle_{PR} \gg \langle \Delta a^2 \rangle_L^{1/2}$. Using Consolmagno's (Consolmagno, 1979) derivation for $\langle \Delta a^2 \rangle_L^{1/2}$ in a circular

orbit, the estimates of Jokipii and Coleman (1968) for the fluctuating perpendicular component of the magnetic field (based on measurements by *Mariner 4*), the Burns et al. (1979) expression for $\langle \Delta a \rangle_{PR}$, and adopting $q = bV/300$ esu for the particle's electric charge, we can write the condition above as $\frac{bQ_{pr}}{V} \gg 0.64 \left(\frac{a^3}{\Delta t} \right)^{1/2}$, where b is the particle's radius in μm , V is its electrical potential in volts, a is in AU, and Δt is in years. The dependence on the time Δt arises from the fact that the P-R effect causes a systematic drift in a that is proportional to Δt , while the fluctuating Lorentz force causes a diffusion in a that is proportional to $(\Delta t)^{1/2}$. Scaling the comparison time Δt by the orbital period of the particle, that is, $\Delta t = (ka)^{3/2}$, where k is a numerical factor, we find that the P-R effect will dominate Lorentz scattering for particle sizes $b \gg 3.2 \left(\frac{a/1\text{AU}}{k} \right)^{3/4} \left(\frac{V}{5\text{volt}} \right) \left(\frac{1}{Q_{pr}} \right) \mu\text{m}$. Thus, for particles of radius larger than a few microns, the systematic P-R drift will exceed the random Lorentz scattering on timescales from a few orbital periods in the inner solar system to a few tens of orbital periods in the outer solar system. Over the characteristic P-R drift timescale, $(a/\dot{a})_{PR}$, Lorentz scattering is negligible for the particle sizes and heliocentric distances in our models. We therefore consider that neglecting the Lorentz force does not constitute a major limitation of this work.

3.7.2 Collisions

Particles that from the dynamical point of view are able to drift all the way into the Sun, may get destroyed by mutual collisions or collisions with interstellar dust grains before they reach the inner Solar System. Based on Ulysses measurements of interstellar dust flux at 5 AU, and assuming that this flux is constant throughout the Solar System and does not vary in time, the average time for one collision to occur between an spherical grain of diameter d and an interstellar grain of diameter d_i : $t_c = 504/(d+d_i)^2$ Myrs (LZD96). Assuming that interstellar dust grains have an average size of $1.2 \mu\text{m}$, the collisional times for 1,2,4 and $9 \mu\text{m}$ particles are 104, 49, 19 and 4.8 Myrs respectively. For densities of 2.7 gcm^{-3} these sizes correspond

to β s of 0.4, 0.2, 0.1 and 0.05 respectively. KB dust grains, however, are more likely to have lower densities. Analysis of collected IDPs indicate that high velocity IDPs have fluffy, porous textures with an average density of about 1 g cm^{-3} (Joswiak et al., 2000). For those densities the sizes corresponding to the β s above are 3, 6, 11 and $23 \mu\text{m}$. These particles will have collisional times of 28.6, 9.7, 3.4 and 0.86 Myr respectively. In these size ranges mutual collisions are not as important as collisions with interstellar grains (LZD96). If so, comparing the collisional times and the dynamical lifetimes in Figure 2.3 shows that collisional destruction is only important for grains larger than about $6 \mu\text{m}$. Smaller particles will therefore survive collisions and drift all the way into the Sun contributing to the zodiacal cloud. Particles larger than $50 \mu\text{m}$ may also survive collisions because interstellar grains are too small to destroy these in a single impact, so it is possible that they are able to evolve into the inner Solar System (LZD96). Figure 2.7 shows the timescale for disk structure formation in the case of $\beta=0.1$. Structure is already beginning to form by about 8 Myrs; by 16 Myr, the structure shows almost all the features of the equilibrium state. Collisional time scales for $\beta=0.1$ range from 3.4 to 19 Myrs, depending on the density. It is not clear therefore that disk structure for these particles sizes is able to survive collisions. For smaller particles (larger β s) structure will survive, but these particles do not have as prominent a structure associated with the exterior MMRs with outer planets (see Figure 2.5). Although all these results should be taken with caution, since the flux and the size distribution of the interstellar grains are rather uncertain, what is clear is that one should keep in mind collisions with interstellar grains when trying to infer the presence of planets from the study of structure in debris disk (see also LZ99).

3.7.3 Sublimation

Depending on the composition of dust particles, sublimation may or may not play an important role in dust destruction processes and therefore in the ability of dust to

reach the inner Solar System. For silicates, the sublimation temperature is ~ 1500 K. For the particle sizes considered in this paper, 1, 2, 4, 9 and $40 \mu\text{m}$ (that correspond to β s of 0.4, 0.2, 0.1, 0.05 and 0.01 with $\rho=2.7 \text{ gcm}^{-3}$), this temperature is reached at $r < 0.5$ AU, which is the minimum heliocentric distance allowed by our models. In this case, sublimation does not affect the evolution of dust particles and the radial disk structure. But if the KB dust composition is more similar to water ice, the sublimation temperature is ~ 100 K, then for sizes of 3, 6, 11, 23 and $120 \mu\text{m}$ (corresponding to the β s above with $\rho=1 \text{ gcm}^{-3}$), this temperature is reached at 27, 19, 14, 10 and 4.3 AU respectively. In this case, the ability of dust to reach the inner Solar System would be greatly diminished by sublimation, even for dust grains as large as $120 \mu\text{m}$, and the disk structure created by the inner planets would be destroyed. For example, the staying time for a grain between 1 AU and 2 AU from the Sun on an orbit with $a=10$ AU and $e=0.9$ (i.e. $q=1$ AU and $Q=19$ AU) is $\sim 10^7$ s, while the lifetime of an icy grain with a radius of $163 \mu\text{m}$ is $\sim 10^3$ s at 2 AU from the Sun (Mukai, 1986; Gustafson, 1994). Therefore, the icy grain cannot survive near the Earth due to quick sublimation. KB grains are likely a mixture of silicates and ices. While the ice fraction will sublimate quickly, the silicate remnant will likely survive to sub-Earth perihelion distances. Qualitatively, and for the size ranges considered in this paper, we expect that the rapid loss of the ice component will cause the grain's orbit to become more eccentric, as a result of the increased magnitude of radiation pressure on smaller grain sizes. Thus, our dynamical models would underestimate the eccentricities of KB grains on Earth-crossing orbits. (However, for smaller grains of radii less than a few tenths of a micron, the effect would be the opposite because β decreases as the grain's radius decreases.) Furthermore, taking into account the sublimation of the icy fraction, our conclusion from §3.5, that $\sim 1\%$ of silicate IDPs may be from the KB, becomes an upper limit. The overall conclusion is still the same: most of the captured IDPs do not come from the KB.

3.7.4 Sputtering

Sputtering by solar wind particles may cause mass loss and erosion of dust grains, as well as chemical alteration of their surfaces. The erosion rate is quite uncertain in the existing literature. Most estimates are based on the analysis of *Apollo* samples of lunar soils and related computer simulations and bombardment experiments. Some of these estimates are as follows: McDonnell and Flavill (1974) and McDonnell et al. (1977), estimated an erosion rate of $0.043 \text{ \AA yr}^{-1}$ and 0.43 \AA yr^{-1} , respectively, on the basis of He^+ bombardment experiments. A few years later, Flavill et al. (1980) estimated $0.025\text{--}0.045 \text{ \AA yr}^{-1}$, while Kerridge (1991) estimated $0.0024 \text{ \AA yr}^{-1}$ based on analysis of Ar^{36} retention efficiency for solar wind implantation and its measures in a lunar sputtered surface. In another independent study, Johnson and Baragiola (1991) estimated erosion rates of $0.1\text{--}0.2$, $0.01\text{--}0.03$ and $0.002\text{--}0.003 \text{ \AA yr}^{-1}$, where the two lower estimates take into account the decrease of sputtering efficiency due to the sticking of sputtered material to neighboring grains and to micrometeorite vapor deposition, respectively. Evidently, the estimated erosion rates differ by up to a factor of 200 in these studies. Most recently, Mukai et al. (2001) suggest a rate of $0.1\text{--}0.2 \text{ \AA yr}^{-1}$.

Adopting an erosion rate of 0.2 \AA yr^{-1} at 1 AU, and taking into account that it scales with heliocentric distance roughly as r^{-2} , we can estimate the mass loss experienced by our modeled KB dust grains. Our dynamical studies of KB dust show that most of the particles spend most of their time at $a > 20$ AU, and that their typical lifetime is $\sim 10^7$ yr (Figures 2.3 and 3.3). Consider a typical particle that spends 10^7 yr at 20 AU from the Sun. The fraction of mass loss is $\sim 50\%$ for a $3 \mu\text{m}$ particle, and it scales as b^{-1} , where b is the particle radius. (This is likely an upper limit because the particles usually get trapped in exterior MMRs with Neptune at $a > 30\text{AU}$.) Of course, one would need to take into account that as the particles drift in as a result of P-R drag, their erosion rate increases because of

increased solar wind flux at smaller heliocentric distance. Our dynamical studies show that typically particles spend less than $\sim 10^6$ yr inside 20 AU. We estimate that a 3 μm grain will be almost completely destroyed before reaching the inner solar system, while a 10 μm grain will suffer little erosion. If the erosion rate is 100 times smaller than our adopted value (and within the present uncertainties), the mass loss would be negligible in both cases. We may therefore conservatively conclude that grains >10 μm do not suffer significant erosion due to corpuscular sputtering.

Sputtering-induced chemical alteration of dust grain surfaces may also reduce the mass loss. Corpuscular sputtering preferentially depletes the surface regions of volatiles, but also causes implantation of ions that can change the chemistry of the grain surface by producing mixing and molecular bonding between layers of dissimilar materials. This may explain why IDPs, thought to be Van der Waals-bonded aggregates, can lose icy mantles and remain sufficiently stable to survive atmospheric entry. A blackened, sputter-resistant, highly carbonized and refractory surface layer can be created from organic and volatile mantles (Johnson and Lanzerotti, 1986; Johnson, 1990; Mukai et al., 2001). Once this layer is formed, the efficiency of erosion by corpuscular sputtering will be reduced.

Our conclusions above are consistent with the findings of Mukai and Schwehm (1981) and Johnson (1990) who conclude that at the distances at which sputtering is important, the erosion is relatively small under present solar wind conditions but chemical alterations may be significant.

We note here that one of our long-term goals, as part of the *Spitzer* FEPS Legacy project (principal investigator M. Meyer),² is to study the effect of planets and radiation on the particle size distribution in exo-planetary systems. Considering that there are large uncertainties in the solar wind corpuscular sputtering effects,

²<http://feps.as.arizona.edu>

as well as the interstellar grain flux and size distribution for our own solar system, we think it is not well-justified to introduce in our numerical models the effects of sputtering and collisions for systems where the interstellar dust environment would likely be even less well known.

3.8 Conclusions

(1) Overall, the number density of the KB dust disk shows a depletion of dust in the inner 10 AU, due to gravitational scattering by Jupiter and Saturn, and an enhanced dust density in a ring between 35 and 50 AU, due to trapping of particles in MMRs with Neptune. The structure is more pronounced for larger particle sizes. The brightness distribution shows a bright ring between 10 and 15 AU with a sharp inner edge (particles ejected by Saturn and Jupiter), and a steep increase in brightness in the inner few AU (a combination of the decreasing number density and increasing grain temperature).

(2) We have calculated disk brightness density and spectral energy distributions (SED), assuming greybody absorption and emission from the dust grains. We find that the presence of planets modifies the shape of the SED. The Solar System debris disk SED is particularly affected by the clearing of dust from the inner 10 AU due to gravitational scattering by Jupiter and Saturn.

(3) We have estimated the radial distribution of KB dust from our dynamical models and the KB dust production rate estimates from Landgraf et al. (2002). (We neglect dust physical destruction processes.) We find that the presence of planets has a very important effect on the distribution of dust: for particles larger than the blow-out size ($\beta < 0.5$), the gravitational scattering of dust by the giant planets is able to extend the disk beyond the boundaries set by radiation effects alone. We also find that it has important consequences for the dust size-frequency distribution (see below).

(4) The observation of dust disks of wide radial extent, a hundred to thousands of AU, does not necessarily imply the presence of dust-producing planetesimals at such large distances, because the gravitational scattering by giant planets at much smaller semimajor axes can cause the dust to spread to distances much larger than the aphelion of the dust parent bodies.

(5) Radiation forces alone change the differential size distribution from the (assumed) initial power law of index $q = 3.5$ at production, to a shallower power law with $q \approx 2.5$, valid at distances smaller than the aphelion of the parent bodies. No large particles are found at larger distances, and consequently the size distribution there is very steep. However, when we account for planetary perturbations, the size distribution changes greatly at these large distances. Overall, we conclude that the combination of radiation forces and planetary perturbations causes the dust disk to spread out and the dust size frequency distribution to flatten (Figures 3.8 and 3.9). In a future study, we plan to investigate the potential of the latter effect for the detection of planets in debris disks.

(6) We estimate the total mass of the KB dust disk to be $m_{\text{KB dust}} \sim 1.2 \times 10^{-11} M_{\odot}$ (2.4–160 μm , $\rho=1 \text{ g cm}^{-3}$), or $m_{\text{KB dust}} \sim 4.2 \times 10^{-11} M_{\odot}$ (0.8–150 μm , $\rho=2.7 \text{ g cm}^{-3}$). These estimates are consistent with other KB dust mass estimates found in the literature.

(7) We find in our dynamical models that KB dust grains near Earth have high eccentricities and inclinations similar to those of cometary grains and not asteroidal grains (Figure 3.10). (Sublimation of the volatile fraction of these grains in the inner solar system is likely to increase their eccentricities further.) As a consequence, they have encounter velocities and capture rates similar to cometary dust values; this is contrary to previous results (Liou et al., 1996).

(8) We estimate, following Kortenkamp and Dermott (1998), that at most 25% of IDPs captured by Earth have cometary *or* KB origin. Furthermore, using Landgraf

et al. (2002) estimates of KB dust production rates, we find that the KB presently provides no more than a few percent of the collected IDPs.

(9) We have present the velocity field of KB dust grains in the inner and outer solar system (Figures 3.12 and 3.13). This is potentially useful for planning dust detectors on future spacecraft missions, as well as for estimating the hazard to space probes in the outer solar system.

(10) We estimate that the Lorentz forces due to the interplanetary magnetic field within the heliosphere are likely negligible for the particle sizes considered in this paper. Mainly as a result of the rapid reversals in magnetic field polarity with the solar cycle, and the wrapped structure of the heliospheric current sheet, the effect of the Lorentz force will tend to average out within a particle's orbit.

(11) Some physical destruction processes on KB dust grains may affect their dynamical evolution significantly, and detailed analysis is warranted in future studies. We estimate that the effect of rapid sublimation of the volatile component of KB dust grains is to increase their Earth encounter velocities and to reduce their relative abundance among captured IDPs. The effects of sputtering by the solar wind are insignificant for grain sizes exceeding $\sim 10\mu\text{m}$. Collisional destruction by interstellar grains likely modifies the size frequency distribution further, beyond the effects considered in our dynamical models.

(12) Grain physical lifetimes are limited by collisions, sublimation and sputtering. The comparison of the dynamical lifetime of particles, the timescale for structure formation and the collisional time between KB and interstellar grains indicates that, if the current estimates for the flux and the size distribution of interstellar grains are correct, collisional destruction is important for grains larger than about $6\mu\text{m}$. For smaller particles, debris disk structure will be able to survive, although the smaller particles have less prominent structure associated with the outer planets.

Collisional destruction by interstellar grains likely modifies the size frequency distribution further, beyond the effects considered in our dynamical models. Depending on their composition, sublimation of particles may or may not play an important role in the destruction of structure. If KB dust has water ice composition, and assuming a sublimating temperature of 100 K, it is likely that even large $120\ \mu\text{m}$ particles will sublimate before reaching the inner 4 AU of the Solar System. We estimate that the effect of rapid sublimation of the volatile component of KB dust grains is to increase their Earth encounter velocities and to reduce their relative abundance among captured IDPs. The effects of sputtering by the solar wind are insignificant for grain sizes exceeding $\sim 10\ \mu\text{m}$. We conclude that grain destruction processes need to be examined more carefully in future applications of our studies to infer the presence of planets from structure in debris disks.

CHAPTER 4

Dust Outflows from Planetary Systems

4.1 Introduction

Radiation pressure arises from the interception by the dust particles of the momentum carried by the incident stellar photons; it makes the orbits of the dust particles change immediately upon release from their parent bodies (i.e., the meter-to-kilometer size dust-producing planetesimals). For parent bodies in circular orbits, small grains with $\beta > 0.5$ (corresponding to particles with diameters smaller than $2.4 \mu\text{m}$ for $\rho=1 \text{ g/cm}^3$) are forced into hyperbolic orbits as soon as they are released. (If the parent bodies' orbits are eccentric, ejection occurs for $\beta > 0.5(1 \mp e)$ for a particle released at perihelion or aphelion, respectively.) In the Solar System these particles are known as β -meteoroids (Zook and Berg, 1975). As these dust particles are being produced, they leave the system in a “disk wind”, whose angular extent is determined by the inclinations of the parent bodies; this is because radiation pressure is a radial force which does not change the inclinations of the dust particles after their release.

Larger grains, on the other hand, remain on bound orbits upon release, and their orbital evolution is the subject of our study. Their dynamical evolution is affected by the P-R effect, which tends to circularize and shrink their orbits, forcing these particles to slowly drift in toward the central star (Burns et al., 1979). If no planets were present, the final fate of these dust particles would be to drift all the way into the star until they sublime. But when planets are present the story

changes: (a) the trapping of particles in mean motion resonances (MMRs) with the planets causes an accumulation of particles at resonant semimajor axes; and (b) sufficiently massive planets can scatter and eject dust particles out of the planetary system. In the case of dust produced in the Kuiper Belt in our Solar System, about 80–90% of the dust grains are ejected by close encounters with the giant planets (mainly Jupiter and Saturn), a few percent accrete onto the planets, and the remaining 10–20% drift all the way into the Sun (Liou et al., 1996; Moro-Martín and Malhotra, 2003); (see also Table 4.1). Thus, in addition to the afore-mentioned β -meteoroids, an outflow of larger particles produced by gravitational scattering from planets also exists.

We show that this large-particle outflow is mainly confined in angular extent to a disk. We describe the characteristics of this outflow in different planetary architectures, discuss its detectability, its implications for exo-planetary debris disks, its contribution to the clearing of circumstellar debris in planetary systems, its effect on the particle size distribution of the immediate vicinity of star-forming regions, and its implications for the interpretation of in-situ dust detection experiments in space probes traveling in the outer Solar System.

4.2 Dependence on Planetary Architecture

We have explored the characteristics of the large particle outflow and its dependence on planetary architecture. For the solar System architecture, it is known that the majority of KB dust particles are ejected by Jupiter (Liou et al., 1996; Moro-Martín and Malhotra, 2003). Motivated by this, we have modeled 13 hypothetical planetary systems consisting of a single Jovian-mass perturber and a KB dust source. These 13 models explore a range of planetary masses M_p (0.054, 1, 3, and 10 M_{Jup}), and orbital semimajor axis, a (1, 5.2 and 30 AU), and we also considered 3 cases of eccentric planetary orbits ($a=5.2$ AU, $e=0.4$) (see Table 4.1). Figure 4.1 shows

examples of the escaping¹ particle trajectories for the Solar System case, projected in the ecliptic plane (XY; left panel), and in the RZ plane (right panel; where R is the in-plane heliocentric distance and Z is the off-plane out-of-ecliptic distance). These examples are of particles that reach 1000 AU and had their last encounter with Jupiter. We see that Jupiter creates a fan-like outflow, mainly confined to the ecliptic. All the trajectories are in the same counterclockwise (prograde) direction; the inclination distribution shows that the scattering rarely changes the inclination of the particles by more than 15 degrees. We see in Figure 4.2 that the escaping particles are all ejected outward, i.e. none achieve perihelion interior to Jupiter’s orbit. An explanation for this comes from the well known approximate conservation of the Tisserand parameter in the restricted 3-body problem: $T = 1/a + 2(a(1-e^2))^{1/2}\cos(i)$, where the particle’s semimajor axis, a , is in units of Jupiter’s semimajor axis. Prior to a close encounter, particles in low eccentricity, low inclination orbits drifting toward Jupiter have $T > 3$. If ejected during a close encounter, their perihelion distance $q > 9/8$, owing to the conservation of the Tisserand parameter. (Of course, the PR drag does not conserve the Tisserand parameter; the above argument applies only to the short period of evolution of particles as they approach Jupiter’s orbit).

In Figure 4.2 the velocities projected in the XY (ecliptic) plane (left) show that the outflow is radial; the projection in the XZ plane (right) shows that it is largely confined to the ecliptic, except when massive close-in planets are present. This angular confinement is not obvious a priori because the ejection of the particles is due to gravitational scattering, a process that does not necessarily preserve the

¹Our definition of “escaping” is that the particles reach a distance 1000 AU from the star (see Figure 4.2); at that point, we stop integrating their orbits. This is not quite equivalent to the precise criterion for ejection, which would be that a particle’s velocity exceed the escape velocity. However, our numerical studies find that the particles that reach 1000 AU, 30-60% (depending on their β) are in hyperbolic orbits, and more than 90% have orbital eccentricity $e > 0.98$. This means that even though some of the particles are still bound by the time they reach 1000 AU, it is very likely that they will also be set on hyperbolic orbits within a few orbits, either by subsequent scattering from the planets or due to small additional perturbations not included in our models.

Table 4.1: Average ejection velocities.

a: \bar{v}_∞ : mean value of the velocity at infinity, $(2E)^{1/2}$, of the particles on hyperbolic orbits; $\sigma_{\bar{v}_\infty}$: standard deviation; n_{1000} : number of particles that reach 1000 AU (out of a total of 100); n_{ejec} : number of particles on hyperbolic orbits ($E > 0$).

b: Parent bodies with $a=35\text{--}50$ AU, $e=0\text{--}0.05$ and $i=0\text{--}0.05$ radians.

c: Models include the seven Solar System planets (excluding Mercury and Pluto).

d: Parent bodies of the dust particles are distributed like the KBOs, with $a=35\text{--}50$ AU, e such that perihelion= $35\text{--}50$ AU and $i=0\text{--}17^\circ$.

M_{planet} (M_{Jup})	a	e	β	$\bar{v}_\infty^a (\sigma_{\bar{v}_\infty}^a)$ (km/s)	$(\langle v_z^2 \rangle / \langle v_{xy}^2 \rangle)^{1/2}$	n_{1000}^a	n_{ejec}^a
Single Planets:							
1 (KB)	1	0	0.044	5.9(4.6)	0.10	54	48
(thin) ^b				5.8(4.7)	0.10	58	53
3 (KB)	1	0	0.044	6.2(4.5)	0.17	80	72
(thin)				6.5(3.8)	0.06	91	89
10 (KB)	1	0	0.044	5.5(4.4)	0.29	94	86
(thin)				4.6(5.6)	0.31	89	78
1 (KB)	5.2	0	0.044	2.8(1.8)	0.15	79	54
(thin)				2.6(1.6)	0.09	75	53
3 (KB)	5.2	0	0.044	2.7(1.6)	0.19	90	63
(thin)				3.7(3.0)	0.27	88	52
10 (KB)	5.2	0	0.044	2.1(2.8)	0.16	97	66
(thin)				2.0(2.2)	0.41	95	48
1 (KB)	30	0	0.044	0.9	0.003	83	1
(thin)				1.1(0.8)	0.08	81	10
3 (KB)	30	0	0.044	0.9(0.4)	0.06	99	8
(thin)				1.2(0.7)	0.05	97	17
10 (KB)	30	0	0.044	1.2(0.6)	0.08	97	49
(thin)				1.4(0.6)	0.03	96	52
1 (KB)	5.2	0.4	0.044	2.9(1.8)	0.09	41	17
(thin)				2.9(2.2)	0.12	48	26
3 (KB)	5.2	0.4	0.044	2.7(2.1)	0.10	93	50
(thin)				2.5(1.8)	0.03	87	53
10 (KB)	5.2	0.4	0.044	1.9(1.3)	0.12	92	42
(thin)				3.2(2.9)	0.05	89	36

Table 4.2: Average ejection velocities (cont.)

M_{planet} (M_{Jup})	a	e	β	$\bar{v}_\infty^a (\sigma_{\bar{v}_\infty}^a)$ (km/s)	$(\langle v_z^2 \rangle / \langle v_{xy}^2 \rangle)^{1/2}$	n_{1000}^a	n_{eject}^a
Solar System ^c :							
(KB) ^d			0.01	2.0(1.3)	0.07	87	32
			0.05	2.1(1.6)	0.08	78	28
			0.1	2.0(1.5)	0.05	76	48
			0.2	2.4(1.7)	0.10	85	42
			0.4	3.3(2.1)	0.10	89	58

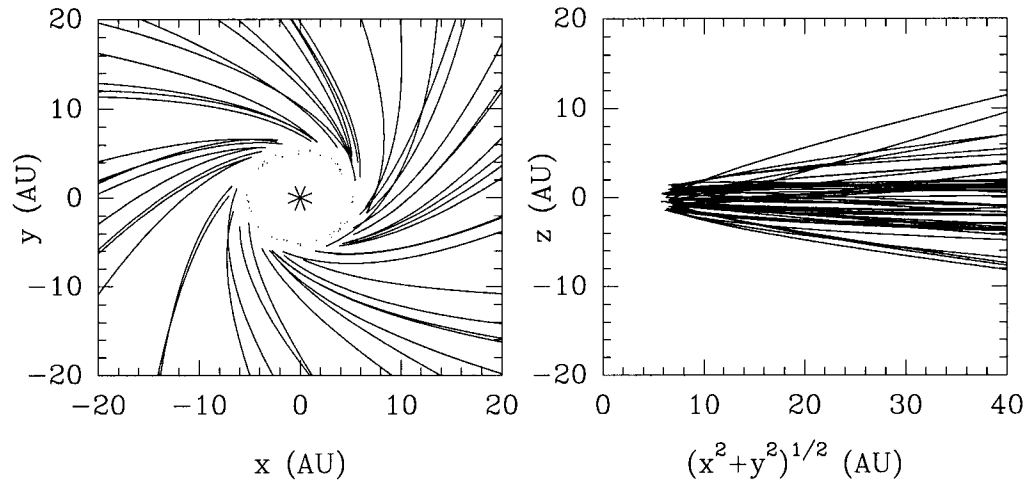


Figure 4.1: Trajectories of the particles that reach 1000 AU after scattering by Jupiter. These particles have $\beta=0.2$ and their paths are shown just after the last encounter with the planet. (left) in the XY plane; the dots represent the position of Jupiter at the time of last encounter; (right) in the RZ plane, where $R=(x^2+y^2)^{1/2}$ is the in-plane heliocentric distance and Z is the off-plane out-of-ecliptic distance.

inclination of the orbits.

Table 4.1 gives a list of the multiple and single-planet models that we used to study how the outflow velocity and angular confinement depend on the planets' masses and orbital elements. The values in this table correspond only to the averages of the particles on hyperbolic orbits, i.e. with $E > 0$ and $v_\infty = (2E)^{1/2}$, where E is the total energy of the particle and v_∞ is its velocity at infinity (the number of hyperbolic orbits is given by n_{eject} out of a total of 100). We find the following dependencies (the parentheses show the values explored by our models).

- *Particle sizes* ($\beta=0.01, 0.05, 0.1, 0.2, 0.4$, corresponding to particle diameters of 115, 23, 11, 6 and 3 μm , for $\rho=1 \text{ g/cm}^3$): There is only a weak dependence of \bar{v}_∞ on particle size for $\beta \ll 0.5$. We find that particles of all sizes are equally confined to the disk, have similar velocities and similar probabilities of ejection (Table 4.1). This is not surprising because gravitational scattering is independent of particle size, as particle masses are more than 30 orders of magnitude smaller than the masses of the planets.
- *Planet semimajor axis* (1, 5.2 and 30 AU): We find that the average dust outflow velocity is larger in the presence of closer-in planets than more distant planets of the same mass (see Table 4.1). This can clearly be seen in the left panel of Figure 4.3. The slope of the line corresponds to a dependency of approximately $\bar{v}_\infty \sim a_{pl}^{-0.5}$. In a recent paper, Murray et al. (2003) derive an analytical expression for the ejection velocity of a particle using the two body approximation and assuming that during the close encounter with the planet the particle follows a hyperbolic orbit with respect to the planet. They find that $v_\infty \sim a_{pl}^{-0.5}$, in good agreement with our results. The left panel of Figure 4.3 also shows that the velocity of the outflow caused by the $10M_{Jup}$ planet at 30 AU is higher than expected from this relation. The reasons for this discrepancy are not entirely obvious. However, we note that the

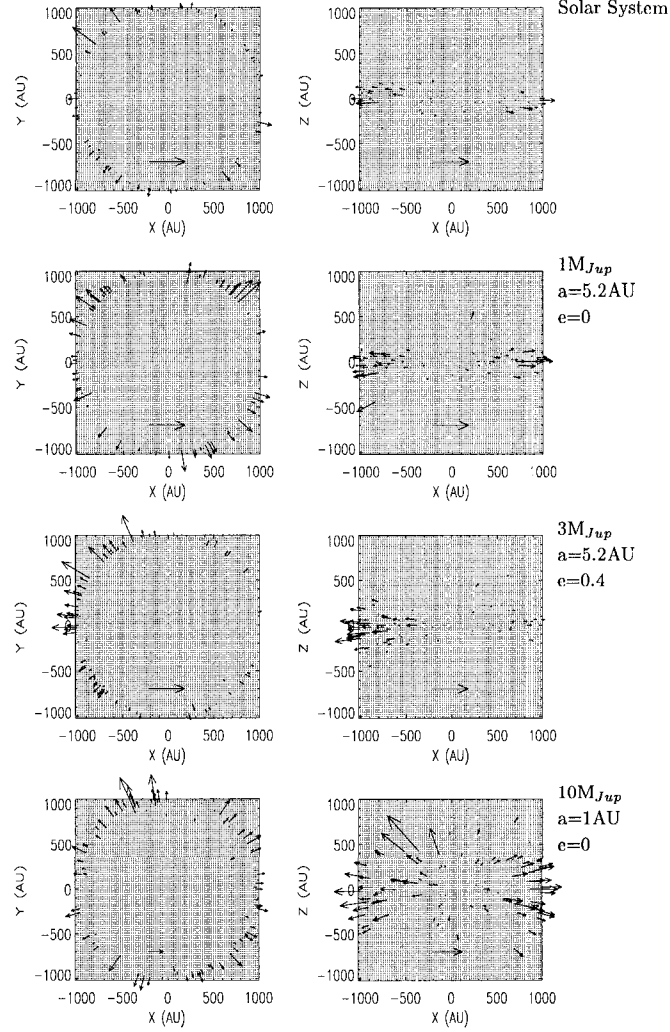


Figure 4.2: Velocities of escaping dust particles in four different planetary systems, shown in the XY plane (left) and XZ plane (right). From top to bottom, the panels correspond to: Solar System (with seven planets, Venus through Neptune) and dust particles with $\beta=0.05$; Single M_{Jup} planet with $a=5.2$ AU and $e=0$ and dust particles with $\beta=0.044$; Single $3M_{Jup}$ planet with $a=5.2$ AU and $e=0.4$ and dust particles with $\beta=0.044$; Single $10M_{Jup}$ planet with $a=1$ AU and $e=0$ and dust particles with $\beta=0.044$. The velocity scale of 10 km/s is indicated by the size of the large arrow at the bottom-center in each panel. In all cases, the dust-producing planetesimals are randomly distributed between $a=35\text{--}50$ AU, $q=35\text{--}50$ AU and $i=0\text{--}17^\circ$.

initial conditions of the parent bodies in that model may not be physically reasonable, because such a planet will have a chaotic zone that extends up to ~ 42 AU, and therefore a KB inner edge would be at distances greater than the 35 AU adopted in our model.

- *Planet mass* (M_{Nep} , M_{Jup} , $3M_{Jup}$ and $10M_{Jup}$): The right panel of Figure 4.3 shows the scaling of the average ejection velocity (\bar{v}_∞) with the mass of the planet. Murray et al. (2003) find $v_\infty \sim M_{pl}^{1/4}$ for planets significantly more massive than Jupiter, with no dependency on the planet semimajor axis. As Figure 4.3 shows, the scaling we find is more complex, depending not only on the planet mass, but also on the planet semimajor axis and the distribution of the dust-producing planetesimals. When the parent bodies are distributed in a KB-like disk (“thick disk”, dotted line), the average ejection velocity is weakly dependent on the planet mass for $1-3M_{Jup}$, with $\bar{v}_\infty = 6.0, 2.7, 0.9$ km s $^{-1}$, for planets at $a_{pl} = 1, 5.2$ and 30 AU, respectively. But for larger masses, $3-10M_{Jup}$, we find three different dependencies: \bar{v}_∞ stays almost constant when $a_{pl} = 1$ AU, decreases to 2.1 km s $^{-1}$ for $a_{pl} = 5.2$ AU and increases to 1.2 km s $^{-1}$ for $a_{pl} = 30$ AU. When the parent bodies are distributed in a thinner disk (i.e. with a smaller range of eccentricities and inclinations; thick line), the average ejection velocity for $1-3M_{Jup}$ is weakly dependent on the planet mass only for $a_{pl} = 1$ and 30 AU, but increases with mass for $a_{pl} = 5.2$ AU. From $3-10M_{Jup}$, \bar{v}_∞ shows a decrease for $a_{pl} = 1$ AU and 5.2 AU, and an increase for $a_{pl} = 30$ AU. The magnitude of the ejection velocity for the Jupiter-like planet (~ 2.7 km s $^{-1}$), is higher than the numerical result given by Murray et al. (2003) (~ 1 km s $^{-1}$), and agrees better with their theoretical estimate (~ 3.3 km s $^{-1}$). But as seen above, the dependency of the ejection velocity does not agree with their predictions. Their analysis, however, assume that the particle ejection takes place after one single encounter, while our models show that multiple encounters are needed. In addition to this complexity,

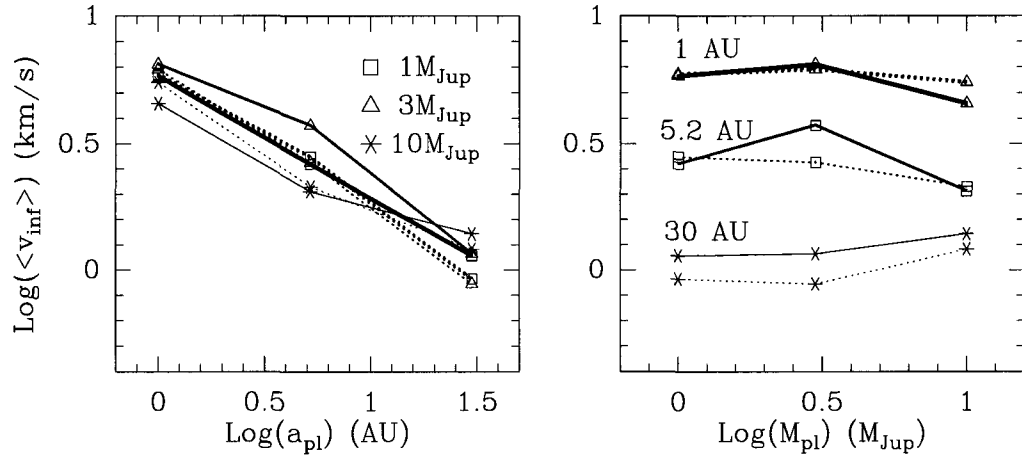


Figure 4.3: Logarithmic plot of the average velocity as a function of planet semi-major axis (left) and planet mass (right). (left) The squares and the heaviest line correspond to $1M_{\text{Jup}}$ planet; the triangles and the second heaviest line to $3M_{\text{Jup}}$ planet; and the stars and thinner line to $10M_{\text{Jup}}$ planet; (right). The triangles and the heaviest line correspond to a planet at 1AU; the squares and the second heaviest line to a planet at 5.2AU; and the stars and thinner line to a planet at 30AU; (dotted line) the parent bodies of the dust particles are distributed like the KBOs, with $a=35\text{--}50$ AU, e such that perihelion= $35\text{--}50$ AU and $i=0\text{--}17^\circ$; (solid lines) parent bodies with $a=35\text{--}50$ AU, $e=0\text{--}0.05$ and $i=0\text{--}0.05$ radians.

it is important to remember that the effect of the planet's orbital elements and mass on the outflow parameters (velocity and confinement to the plane) is not only direct, via the close encounters, but also indirect, as the particles encounter the planet with a history of evolution in the MMRs that can change the initial orbital elements of the particles and therefore affect their subsequent dynamical evolution. As an example, the eccentricity distributions of the soon-to-be-ejected particles near the planet show that for the 1 and 3 M_{Jup} models, $e \sim 0.4\text{--}0.5$, but for 10 M_{Jup} , $e < 0.2$.

Overall our models show that the bulk of the outflow is within 30° of the planet's orbit plane, except for 10 M_{Jup} at 1 and 5.2 AU (see Figure 4.2). For a planet at 1 and 5.2 AU, the angular confinement of the outflow is affected by the planet's mass; the more massive the planet the less confinement the outflow has.

- *Planet eccentricity* (0 and 0.4): Large planet eccentricities create an asymmetric outflow, oriented along the major axis of the planet's orbit and favoring the apoastron direction of the planet (see Figure 4.2); the average outflow velocity is also decreased, compared to the case of a planet on a circular planet orbit (see Table 4.1). The asymmetry is due to the fact that the planet spends more time near apoastron and therefore the probability of encounter with a dust particle is higher near apoastron; the orbital velocity of the planet at apoastron is smaller, explaining the decrease in outflow velocity. It is of interest to notice that many of the known exo-planets to date have large orbital eccentricities (Marcy et al., 2003); our models predict that the large dust grain outflow will be asymmetric in these cases.
- *Comparison with Solar System*: The single planet analog of the Solar System (i.e. only Jupiter in a circular orbit at 5.2 AU) produces a somewhat higher velocity outflow (compared with the actual multi-planet Solar System). This is mainly due to the effect of Saturn in our Solar System: having a larger

semimajor axis, Saturn intercepts a fraction of the KB dust grains as they evolve inward due to the P-R drag and ejects them at a somewhat lower velocity, thus depressing the mean velocity of the outflow.

4.3 Discussion

There are several significant implications of this large-particle outflow.

4.3.1 Exo-Planetary Debris Disks and Planet Formation Environment

Stellar surveys show that at least 15% of A-K main sequence stars are surrounded by debris disks, and that the far-infrared excess decreases with stellar age, dropping from about 50% to about 15% after approximately 500 Myr. But these samples are sensitivity-limited, and therefore the occurrence of debris disks could be higher (Lagrange et al. (2000) and references therein). Stellar radial velocity surveys indicate that about 7% of the FGK main sequence stars have a Saturn or Jupiter-mass planet within 3 AU (Marcy, 2003). Even though the correlation between the presence of planets and debris disks is not known yet, our studies suggest these large-particle dust outflows may be a common phenomena in planetary systems that harbor debris disks. This is of interest because:

(a) These large-particle dust outflows *may contribute significantly or even dominate the clearing of circumstellar debris in planetary systems*. Hitherto, the main processes that have been considered for such clearing are stellar winds, radiation pressure, sublimation, and collisions (that reduce the size of the dust particles until they are small enough to be blown away by radiation pressure). However, as our models indicate, gravitational scattering by giant planets is also significant, and in some cases may be a dominant process, ejecting 50–90% of the dust grain population.

(b) These outflows should be added to the list of processes that *link the interplanetary environment to the galactic environment of a star*. Planetary systems are prime sites for large particle formation. As such, they can contaminate the immediate vicinity of star-forming regions through this large particle outflow, and thus affect the particle size distribution of their local ISM.

The presence of an outflow and its detectability will strongly depend on the orbital characteristics of the planet and the orientation of the system. For face-on systems, the expected surface brightness of the dust outflow will be very low, making it very hard to detect astronomically as a radial extension of the debris disk. Additionally, the lack of velocity information from usual infrared measurements will not allow to distinguish between an outflow and a bound disk.

The face-on optical depth of a disk composed of grains of radius a and observed at frequency ν is given by (Backman and Paresce, 1993): $\tau_{\perp}(r, \nu) = \sigma(r)(\xi a \nu / c)^q$; where $\sigma(r)$ cm²/cm² is the face-on fractional geometric surface density, equal to the surface density $n(r)$, multiplied by the geometric cross section of the grain, $\sigma(r) = n(r)\pi a^2$. ξ is the ratio between the critical wavelength λ_0 up to which the grain absorbs and emits radiation efficiently) and the grain radius a , and depends on the grain properties (e.g. $\xi \equiv \lambda_0/a \sim 2\pi$, $1/2\pi$ and 1 , for strongly, weakly and moderately absorbing materials; we will use $\xi \sim 1$). q is the power law index of the emissive efficiency ϵ , such that for $\lambda < \lambda_0$, $\epsilon \sim 1$, but for longer wavelengths the emissive efficiency decreases as $\epsilon = \epsilon_0(\lambda_0/\lambda)^q$; for the intermediate size regime, where a is larger than λ_{peak} of the incoming radiation (absorbs efficiently) but smaller than λ_{peak} of the grain thermal emission (emits inefficiently), $q=1$. And c is the velocity of light.

We can estimate the surface density $n(r)$ (cm⁻²) at a distance r from the central star from mass conservation by equating the mass that is produced in time dt , $dM = dprf_{ej}dt$, with the mass that crosses the annulus of radius r in time dt ,

$dM=n(r)2\pi r v dt$. dpr is the dust production rate in particles per second; f_{ej} is the fraction of particles that are ejected (our numerical studies find $f_{ej}\sim 50\text{--}90\%$); and v is the velocity of the particles at distance r , for large distances we will take $v\approx v_{esc}=(2GM_{Sun}/r)^{1/2}$. Solving for $n(r)$ and substituting into $\sigma(r)$,

$$\tau_{\perp}^{outflow}(r, \nu) = \sigma(r) \left(\frac{\xi a \nu}{c} \right)^q = \frac{dpr f_{ej}}{2\pi r (2GM_{Sun}/r)^{1/2}} \pi a^2 \left(\frac{\xi a \nu}{c} \right)^q. \quad (4.1)$$

We can estimate the optical depth of the Solar System's outflow using the KB dust production rates derived by Landgraf et al. (2002), which are based on *Pioneer 10* and *11* measurements and for the Kuiper Belt gives $dpr \sim 2 \times 10^{14}$ particles/s (for particles between 0.01 and 6 mm). Because the size distribution is very steep, one can assume that most of the detections are caused by particles just above the detection threshold, i.e. particles with $a \approx 5 \mu\text{m}$. For this particle size, $\beta \approx 0.05$ and $f_{ej} \approx 0.8$, and the optical depth at $60 \mu\text{m}$ ($\nu = 5 \times 10^{12} \text{Hz}$) will then be $\tau_{\perp}^{outflow}(r, \nu) = 2.6 \times 10^{-14} / r^{1/2}$ (where r is in AU). We can compare this to the optical depth of the Kuiper Belt (bound) disk. From Figure 3.4 we can get the surface density that corresponds to a fictitious dust production rate of 100 particles per 1000 years, $n \approx 300$ particles/AU². Scaling up this density to account for the dust production rate found by Landgraf et al. (2002), we find that $n \approx 8.4 \times 10^{-2}$ particles/cm², $\sigma \approx 6.6 \times 10^{-8}$, so that $\tau_{\perp}^{disk} \approx 5.5 \times 10^{-9}$. For the Solar System, the ratio of the two optical depths is then $\sim 10^{-6}$. Other models for the Kuiper Belt dust disk give $\sigma \approx 10^{-6}$ (15 times larger than our value; Backman et al. (1995)). It is estimated that for a system at 30 pc, the $70 \mu\text{m}$ *MIPS* array in *SIRTF* will be able to detect a disk with $\sigma \approx 3 \times 10^{-6}$ (Backman, 2003). This means that in order to see the Kuiper Belt dust disk the dust production rate will need to be increased by a factor of ~ 3 in Backman's models, or a factor of ~ 45 in our models (using Landgraf's dpr). But in order to see the outflow it will need to be increased by a factor of $\sim 6 \times 10^6$ (Backman's) or 9×10^7 (ours). In any case, this increase will make the bound disk to be optically thick. In other words, for an optically thin debris disks (where our dynamical models are valid), this outflow is very unlikely to be detected. For a

younger and more massive edge-on systems, however, after the giant planets have already formed, it may be possible to detect the outflow out of the plane. In this geometry, the signature of the off-plane outflow will be clearer against the fainter background (Rieke, 2003).

It is possible that such an outflow may have already been detected *in situ* with the Advanced Meteor Orbit Radar (AMOR), a ground-based radar that senses plasma signatures produced by extra-terrestrial dust particles ablating in the Earth's atmosphere; its high directional accuracy allows identification of the sources of the meteoroids (as small as $40\ \mu\text{m}$ in diameter). AMOR data presented evidence of a general background influx of extra-solar system particles, with enhanced areas that appear to be discrete sources, the main one of which seems to coincide in direction with the debris disk main-sequence star β Pictoris (Taylor et al., 1996; Baggaley, 2000). This result, however, has been recently challenged by Murray et al. (2003). They concluded that the discrete source cannot not be related to β Pictoris because the ejection velocity needed to reproduce the location and velocity of the meteoroids is $\sim 29\ \text{km/s}$, too large to be explained by gravitational scattering with a massive planet. Regardless of this conclusion, it is likely that large particle outflows from extra-solar planetary systems may be a source of the large interstellar particles that have been detected in the interplanetary medium.

4.3.2 Interpretation of *in situ* Dust Detections Made by Space Probes

Recent Ulysses and Galileo dust experiments have led to a very important discovery: the identification of interstellar grains within the heliosphere, sweeping through the Solar System (Grun et al., 1993). Previously, interstellar grains could only be studied by extinction and polarization measurements of optical starlight, not sensitive to grains larger than 0.3 microns because of their small contribution to the optical cross section, and by infrared emission. These in-situ detections allowed for the

first time to study the mass distribution of interstellar grains within the heliosphere, leading to the surprising discovery of a population of large particles ($> 10^{-16}$ kg, Grun et al. (1994)) that are 30 times more massive than the interstellar grains causing stellar extinction. Therefore, more mass is locked up in large grains locally than is expected from the astronomical measurements. As a consequence, the gas-to-dust ratio derived from astronomical measurements (400–600) is found to be much larger than the value of ~ 100 derived from the in-situ detections, implying that the local interstellar cloud exceeds cosmic abundances (Frisch et al., 1999). These very important results rely critically on the correct identification of the origin of the dust grains. This identification is based on a geometrical argument: the direction the grains are coming from, with interstellar grains coinciding with the flow of neutral helium through the Solar System; and a dynamical argument: the impact velocity and the expectation that only interstellar grains are on unbound hyperbolic orbits (Grun et al., 1993). Under the current understanding, the sources of meteoroids in interplanetary space and their orbital properties are assumed as follows: Asteroids: low eccentricity and inclination; Comets: high eccentricity and inclination; Kuiper Belt: low eccentricity and inclination; and Interstellar: hyperbolic, and aligned with the direction of flow of the interstellar gas. However, we have shown in this paper that ~ 80 – 90% of large Kuiper Belt grains ($\beta < 0.5$) are gravitationally scattered outward by Jupiter and Saturn into hyperbolic orbits; therefore there is the potential of misinterpreting these escaping interplanetary particles as interstellar. Ulysses and Galileo detections were probably not affected by this potential confusion because they did not probe beyond Jupiter’s orbit. But other sources of dust exist inside this orbit, such as comets, Asteroid Belt and Trojan asteroids. Due to radiation pressure, some of the dust particles released at those locations will be set on Jupiter crossing orbits, so in principle close encounters with Jupiter could take place resulting on hyperbolic orbits. In the future, we plan to study whether or not these particles may have been detected by Ulysses and Galileo. For the analysis of future in-situ dust detections in the outer Solar System, such as with the *Cassini* Cosmic

Dust Analyzer and the *Interstellar Probe*, it will be important to keep in mind the existence of the large-particle outflow of Solar System dust to correctly identify the origin of the massive fast moving particles, whether interplanetary or interstellar. It has been recently announced that the analysis of the ion charge signals in the *Cassini* dust detector, together with geometric and kinematic considerations, have led to the identification of an interstellar flux at 0.8 AU that is in agreement with the flux measured by Ulysses at 3 AU at the same time (Altobelli et al., 2003). But any dust detections by Cassini outside Jupiter's orbit have not yet been reported.

CHAPTER 5

Model Spectral Energy Distributions of Circumstellar Debris Disks. Belt of Planetesimals with Interior Giant Planets

5.1 Introduction

A first general approach to the simulation of spectral energy distributions (SEDs) of debris disk systems using analytic dust density distributions has been undertaken by Wolf and Hillenbrand (2003) (hereafter WH03). This study made clear that the SED analysis strongly depends on the assumed density distribution, in particular of the smallest grain population. In contrast to the former approach by WH03, however, the dust density distribution of a debris disk should not be chosen *a priori* because it cannot be defined independently from the SED of the embedded star or the dust grain properties (grain size distribution, density and optical constants). In this study we use a self-consistent combination of existing numerical tools for the simulation of debris disk dust density distributions (that take into account the interplay between the central star SED, the grain properties and the dust dynamics), and the radiative transfer simulations in WH03 for the calculation of their emergent SEDs.

We study hypothetical debris disks originating from a belt of planetesimals [from 35 to 50 AU; similar to the Kuiper Belt (KB)] and evolving under the effect of gravitational perturbation from interior giant planets in various planetary configurations. In Chapter 3 we described how in the Solar System, the trapping of particles in mean motion resonances (MMRs) with the giant planets can create structure in

the KB dust disk as the dust particles accumulate at certain semimajor axes. We found that for the Solar System planetary configuration, the azimuthal structure of the dust disk is not predictable in detail (with simulations of a small number N of particles, $N \sim 100$) because it depends sensitively on the times of residence in the various resonances and these are highly variable and unpredictable. After careful analysis we concluded that even though the particle dynamics is chaotic, our method could robustly estimate the equilibrium radial density distribution of dust. We found that the combination of radiation forces and planetary perturbations causes the dust disk to be depleted inward of Saturn's orbit and spread outward beyond the KB source region, and the particle size distribution to flatten.

In anticipation of future observations of unresolved debris disks with *Spitzer*, in this chapter we investigate to what extent these planet-induced changes in the radial spatial density distribution and the particle size distribution affect the dust disk SED, and how these effects might be exploited to infer the presence of giant planets in *spatially unresolved* debris disks. For each of the planetary systems under consideration we will:

1. Calculate the spatial density distribution of dust grains of different sizes, corresponding to different β values. The dynamical evolution of the dust particles depend only on the parameter β , which is the dimensionless ratio of the radiation pressure force and the gravitational force and depends on the grain size and composition. The resulting three-dimensional density distribution is then transformed into a one-dimensional radial density distribution (§ 5.2), which is sufficient to calculate the disk SED because we assume that the disk is optically thin, and therefore the temperature distribution of the grains depends only on the distance to the central star.
2. Select a representative sample of chemical compositions based on debris disk spectroscopic observations. This will include Fe-rich and Fe-poor silicates

(crystalline and amorphous olivine and pyroxene), as well as carbonaceous materials. For each chemical composition, using laboratory optical constants and Mie theory, we will calculate their radiation pressure coefficients averaged over the stellar spectrum. This will allow us to find the correspondence between β and the particle radius (§ 5.3).

3. Once the particle size is known for each β value and selected chemical composition, we will calculate, using the same one-dimensional radiative transfer code as in WH03, the emitted dust SED (plus the stellar scattered light) for each single particle size, single composition disk, using a solar type star as the central heating source, a disk mass of $10^{-10}M_{\odot}$ and a distance of 50 pc. We will later weight and combine these SEDs in order to consider certain particle size distributions (§ 5.4).

A schematic diagram explaining the steps above is shown in Figure 5.1. The goal is to investigate how the presence of planets affects the debris disk's SED by comparing systems with planets (of different masses and different semimajor axis) and systems without planets, and to derive and analyze the parameter degeneracies in the model SEDs.

5.2 Dust Spatial Density Distributions

A detailed description of the dynamical models used to calculate the dust spatial density distributions, the numerical algorithm used to integrate the equations of motion, and the uncertainties inherent in the prediction of structure, owing to the chaotic dynamics of dust orbital evolution, are described in Chapter 2. Here, we briefly overview the main ideas.

We follow numerically, from source to sink, the evolution of sets of 100 dust particles from an outer belt of planetesimals similar to the KB under the

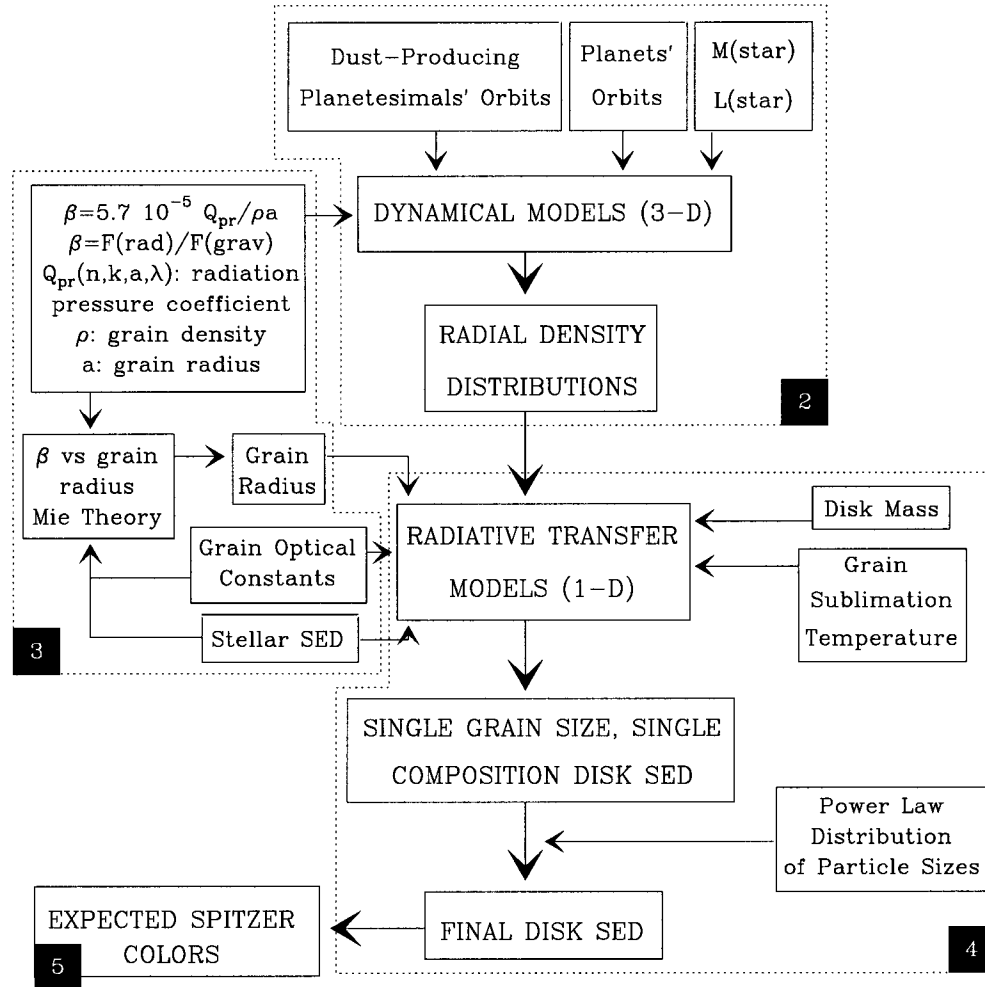


Figure 5.1: Schematic diagram showing the steps of the modeling approach. The numbers inside the black squares indicate the relevant sections in this chapter

combined effects of solar gravity, solar radiation pressure, Poynting-Robertson (P-R) and solar wind drag, and the gravitational forces of the planets. We study the following planetary configurations:

1. The Solar System with 7 planets (excluding Mercury and Pluto). The parent bodies of the dust particles are assumed to be uniformly distributed in orbits with semimajor axis between 35 and 50 AU, eccentricities such that the periastron distances are between 35 and 50 AU (i.e. between 0 and 0.3), and inclinations between 0° and 17° , in approximate accord with current estimates of the orbital distribution of KB objects (KBOs) (Malhotra et al., 2000).
2. A system with the same distribution of parent bodies as above but without planets.
3. Nine single-planet systems with a planet mass of 1, 3 and 10 M_{Jup} in a circular orbit with semimajor axis of 1, 5, and 30 AU. The parent bodies are distributed in orbits with semimajor axis between 35 and 50 AU, eccentricities between 0 and 0.05 and inclinations between 0 and 3° , to account for the fact that a thinner planetesimal disk may be more realistic when a single giant planet is present. [In this study we found that the difference between the “thick” and the “thin” planetesimal disks is negligible]. For the models with a single planet at 30 AU, we ignored the dust particles originated from the 30 planetesimals that lie between 35–40 AU [i.e. inside the 3:2 MMR]. This is because due to multiple close encounters with the planet, we do not expect to have planetesimals in stable orbits in that region.
4. A system with the same distribution of parent bodies as above but without planets.

For the first two cases (KB-like disk with and without Solar System planets), we run 17 sets of 100 particles each, corresponding to 17 different particle sizes,

with β values ranging from 0.00156 to 0.4, distributed to get a uniform logarithmic sampling in particle size (see Figure 5.4). For the rest of the systems (i.e. the “thinner” planetesimal disk with and without single planets), we run a subset of nine β values, also ranging from 0.00156 to 0.4.

We assume that the dust is generated from a constant grinding down of planetesimals due to mutual collisions or collisions with interstellar grains. The sinks of dust included in our numerical simulations are ejection into unbound orbits, accretion onto the planets, and orbital decay to less than r_{min} , where $r_{min} = 0.5$ AU (astrocentric distance) for all models, except for those where the single planet is at 1 AU, for which we use $r_{min} = 0.1$ AU instead. Assuming that the dust production rate is in equilibrium with the loss rate, and the dust particle dynamics is ergodic (i.e. the time-weighting reflects the spatial density), we can obtain equilibrium density distributions by recording the positions of these 100 particles at equal time intervals (every 1000 years); then transforming the particles’ coordinates into a reference frame rotating with the planet dominating the structure (Neptune); and finally treating each position as an individual particle, i.e. accumulating all the rotated particles’ coordinates over the total lifetime of the sample particles. This leads to a three-dimensional time-weighted equilibrium density distributions that is “resampled” into a logarithmic one-dimensional radial grid which is the input for the radiative transfer code.

The dynamics only takes into account gravitational forces and P-R and solar wind drag. It does not include: (1) mutual grain collisions and gas drag (i.e. the systems under consideration are old optically thin disks); (2) quick sublimation of icy fraction (a rapid mass loss can cause the grain’s orbit to become more eccentric); (3) grain erosion due to sputtering by solar wind particles; and (4) Lorentz forces due to interplanetary magnetic fields. For a more detailed description of the applied numerical model and an estimate of its limitations see Chapters 2 and 3.

5.2.1 Radial Density Distributions: Output from the Dynamical Models

Figure 5.2 shows the resulting surface density distributions of dust. The main features are the following:

1. When no planets are present the dust density distribution is flat, as expected for a collisionless system with grains in circular orbits (Briggs, 1962), and no large particles ($\beta < 0.5$) are found at distances larger than the apoastron of the parent bodies. But when planets are present, the surface density distribution deviates from a flat profile (see below) and gravitational scattering of dust by the giant planets is able to extend the disk beyond the boundaries set by radiation effects alone.
2. Depletion of dust inside the planet's orbit due to gravitational scattering by the planet. In the Solar System, depletion takes place in the inner 10 AU from gravitational scattering by Jupiter and Saturn. Inner cavities, possibly created by gravitational scattering, have been also inferred to exist in systems like β Pic (20 AU), HR 4796A (30-50 AU), ϵ Eri (50 AU), Vega (80 AU) and Fomalhaut (125 AU) (Dent et al., 2000; Greaves et al., 2000; Wilner et al., 2002; Holland et al., 2003).
3. Enhanced dust density in a ring outside the planet's orbit. This is produced by the trapping of particles in exterior MMRs with the planet. In the Solar System, the ring is between 35–50 AU and the resonant planet is Neptune. The trapping into MMRs can clearly be seen in the “equilibrium” semimajor axis distributions shown in Figure 5.3 (for the single-planet models) and Figure 3.3 (for the Solar System models).
4. The structure is more pronounced for larger particle sizes (smaller β) because the trapping in MMRs is more efficient when the drag forces are small. The boundary of the disk is less steep for smaller particles (larger β) compared

to larger particles; this is because immediately after release from their parent bodies the orbits of the former are more strongly affected by radiation pressure, which tends to increase their eccentricity and semimajor axis.

The surface density distributions in Figure 5.2 show in some cases scattering at small astrocentric distances. In others cases, the particles drifting inward do not follow a flat surface density (instead it rises steeply). The presence of planets may explain part of these features, but from experience we know that some of this “noise” owes to our use of a logarithmic radial sampling to allow higher spatial resolution near the central star (where the high grain temperature implies a strong contribution to the SED). Where the radial shells are very small, a particle crosses many radial grids before its position is recorded; this, together with the fact that we are modeling the dynamical evolution of a small number of test particles ($N \sim 100$), produces numerical “noise” due to small number statistics. For this reason, as described in § 5.2.2, the radial density distributions that are used as input for the radiative transfer code will not take into account the numerical results at small astrocentric distances.

The depletion factor inside the planet’s orbit is the percentage of particles that are able to drift inward relative to the total number of particles. Because we are modeling sets of only 100 particles, and jovian-mass planets eject a significant fraction of these, the number of particles that drift inward is usually small and is subject to some uncertainty. We have several KB models with the same or similar initial conditions whose results indicate that a conservative estimate of the uncertainty in the depletion factor is $\sim 10\%$ (see Table 5.1). In Table 5.2 we list the final fate of the dust grains for the single-planet models. The quantity $n_{r_{min}}$ is the number of particles that reach r_{min} , the minimum heliocentric distance allowed in the dynamical simulations. However, because some of these particles may have been scattered by the planet, as opposed to smoothly drifting inward, we calculate n_{drift} , the number of particles that reach r_{min} with aphelion $Q = a_{pl} - 3.5 \times r_{Hill}$, i.e. particles that do

not cross the planet’s orbit. In other words, the particle is considered to drift inward if its eccentricity is smaller than some critical value given by $e = (Q - q)/(Q + q)$, where $q = r_{min} = a(1 - e)$ and $Q = a_{pl} - 3.5 \times r_{Hill} = a(1 + e)$. For the single planet models these eccentricities are: 0.767 (1M_{Jup} at 1 AU); 0.767 (1M_{Jup} at 5 AU); 0.957 (1M_{Jup} at 30 AU); 0.735 (3M_{Jup} at 1 AU); 0.735 (3M_{Jup} at 5 AU); 0.950 (3M_{Jup} at 30 AU); 0.658 (10M_{Jup} at 1 AU); 0.658 (10M_{Jup} at 5 AU); and 0.933 (10M_{Jup} at 30 AU). Therefore, n_{drift} , rather than n_{min} , gives an estimate of the depletion factor. As Table 5.2 shows, depletion factors are smaller than 10% for the majority of the single-planet systems studied (and for most β values), except for 1M_{Jup} at 1 AU and 5 AU for $\beta > 0.025$, for which depletion factors are $\sim 20\%$ – 40% and $\sim 20\%$ – 50% , respectively. This means that except for these two cases, the uncertainty due to the small number of particles studied makes the depletion factors obtained consistent with having an empty hole.

5.2.2 Radial Density Distributions: Input for the Radiative Transfer Models

The radial density distributions are uncertain interior to the planet’s orbit to a 10% level. To account for this uncertainty, and to estimate the contribution of the particles trapped in the MMRs to the SED of the disk, we will calculate and compare the SEDs that arise from three different types of surface density distributions (see Figure 5.2):

1. *Empty Gap* models: the surface density distribution accounts for the trapping of particles in the MMRs with the planet and the total depletion of particles interior to the planet’s orbit, i.e. we assume that the “gap”¹ is empty. The astrocentric distance of this “gap” is determined by the radius at which the

¹In this chapter a “gap” is an inner hole interior to the planet’s orbit, not an angular depletion zone around the planet’s orbit.

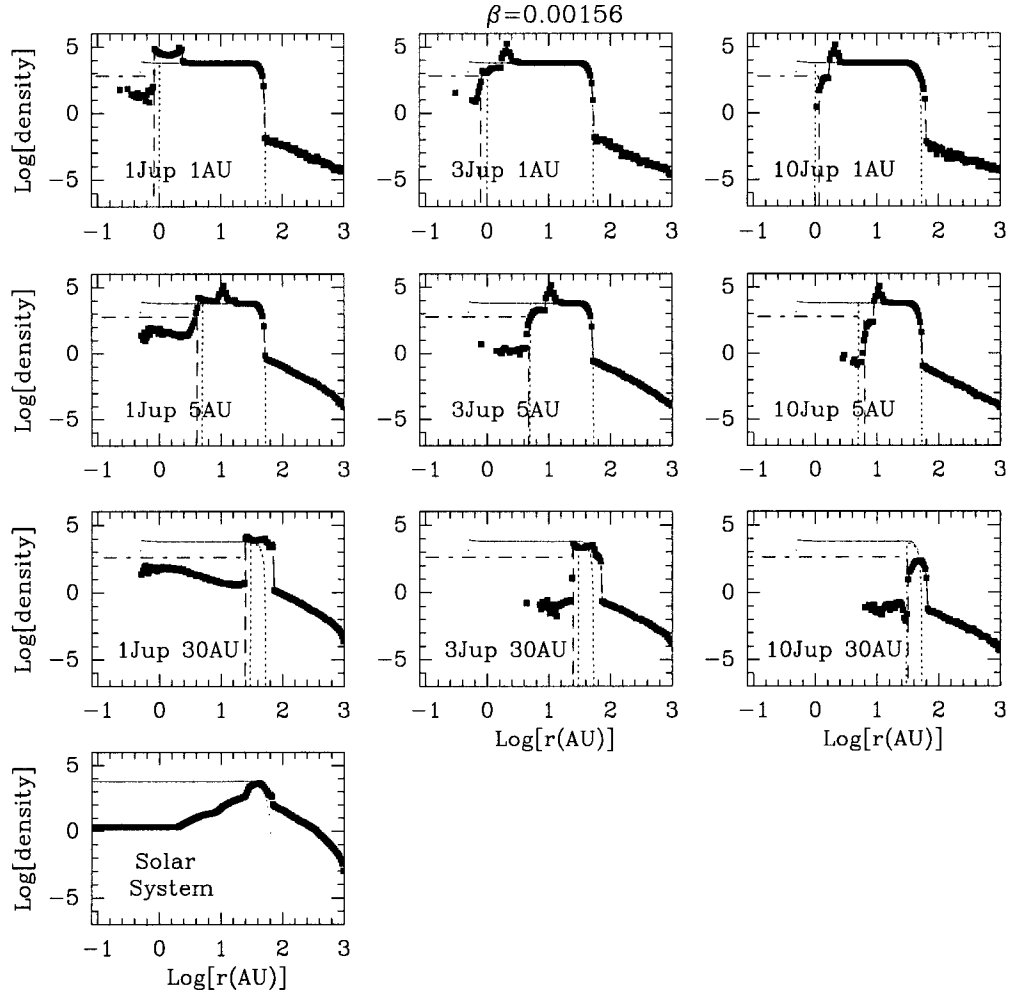
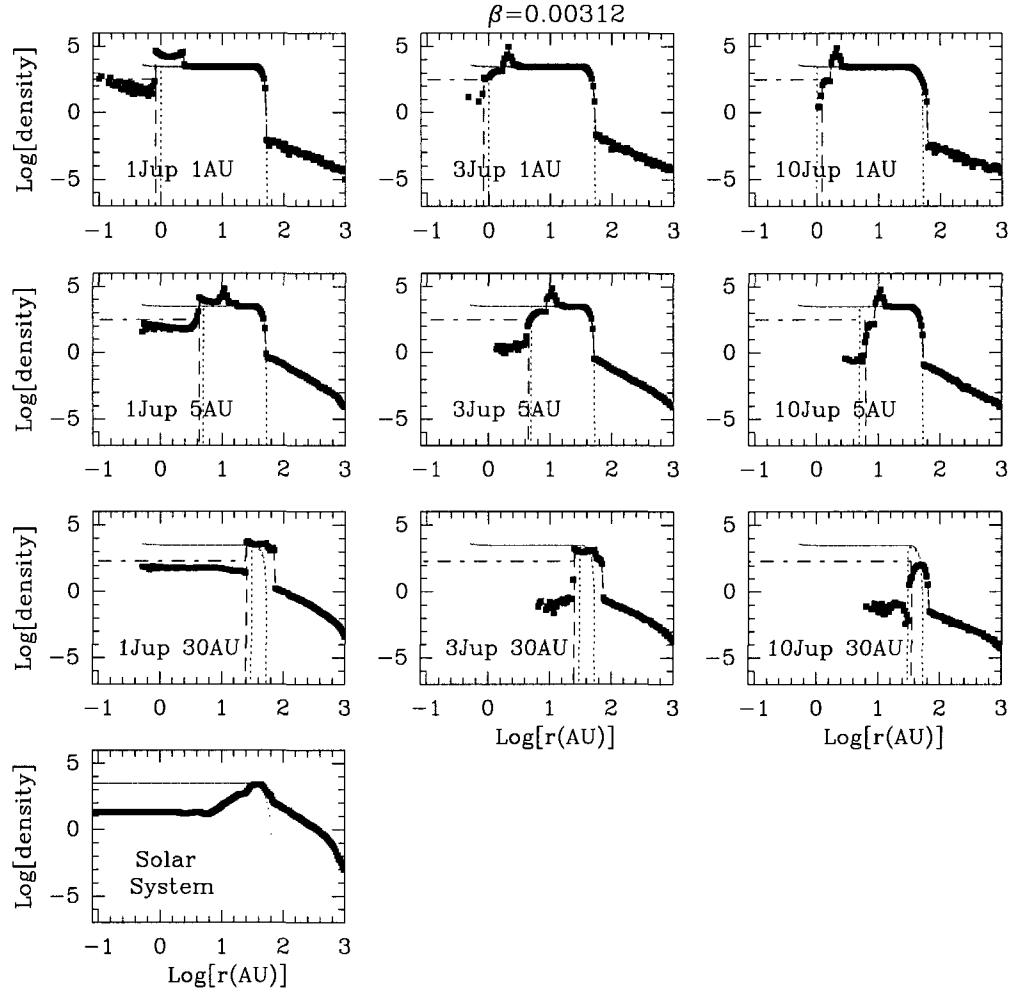
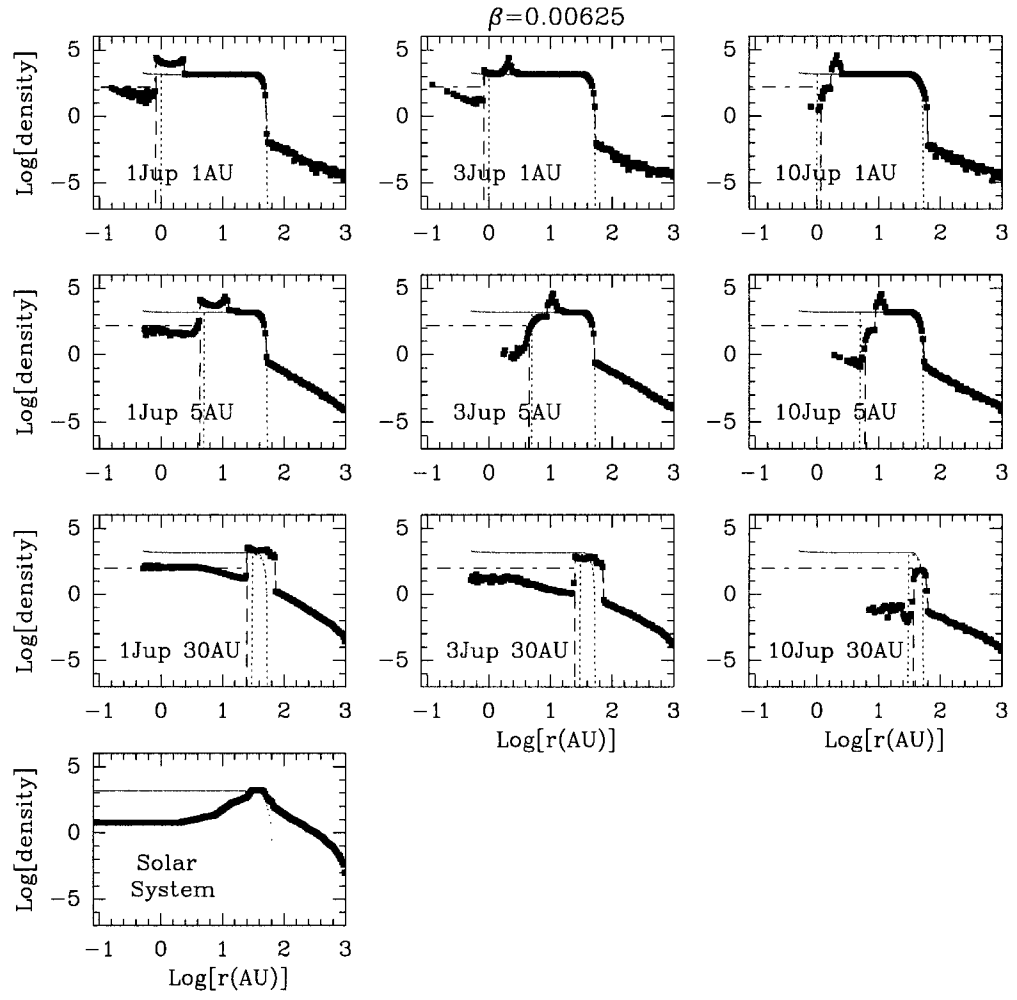
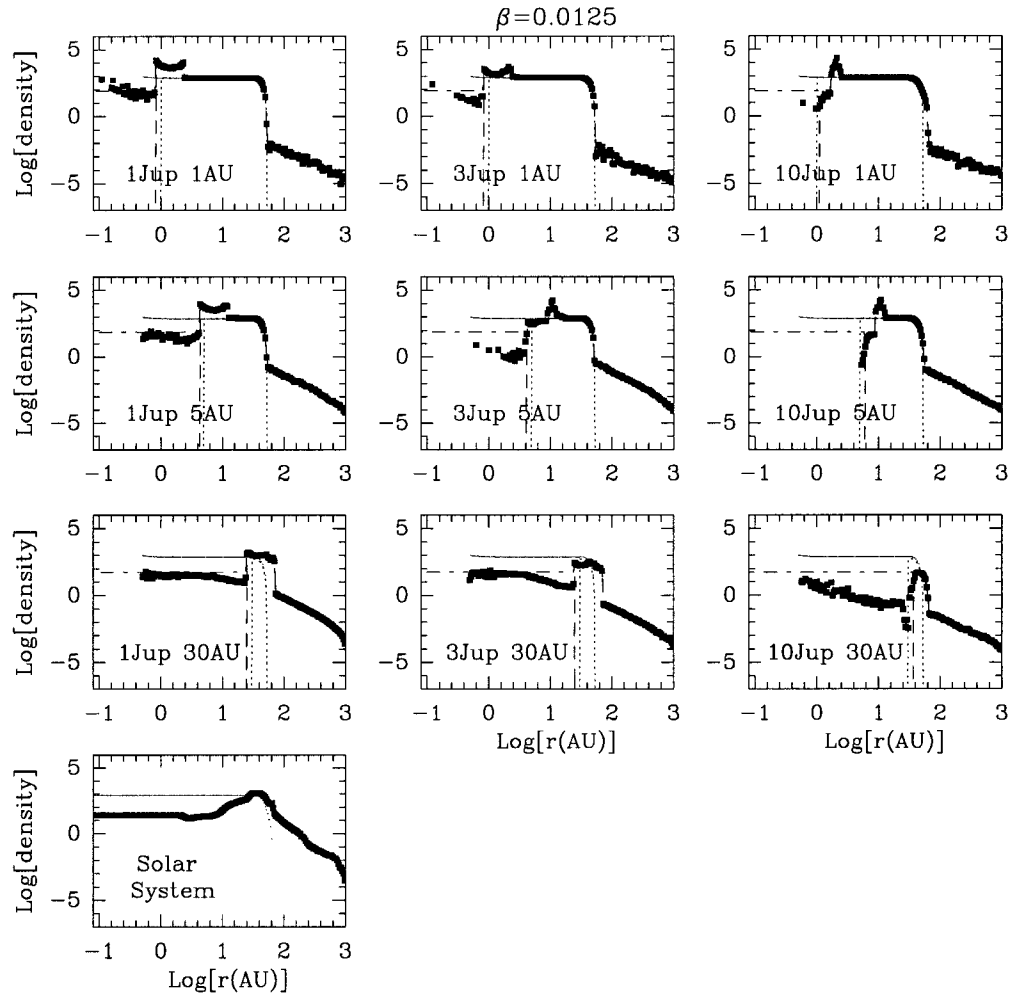
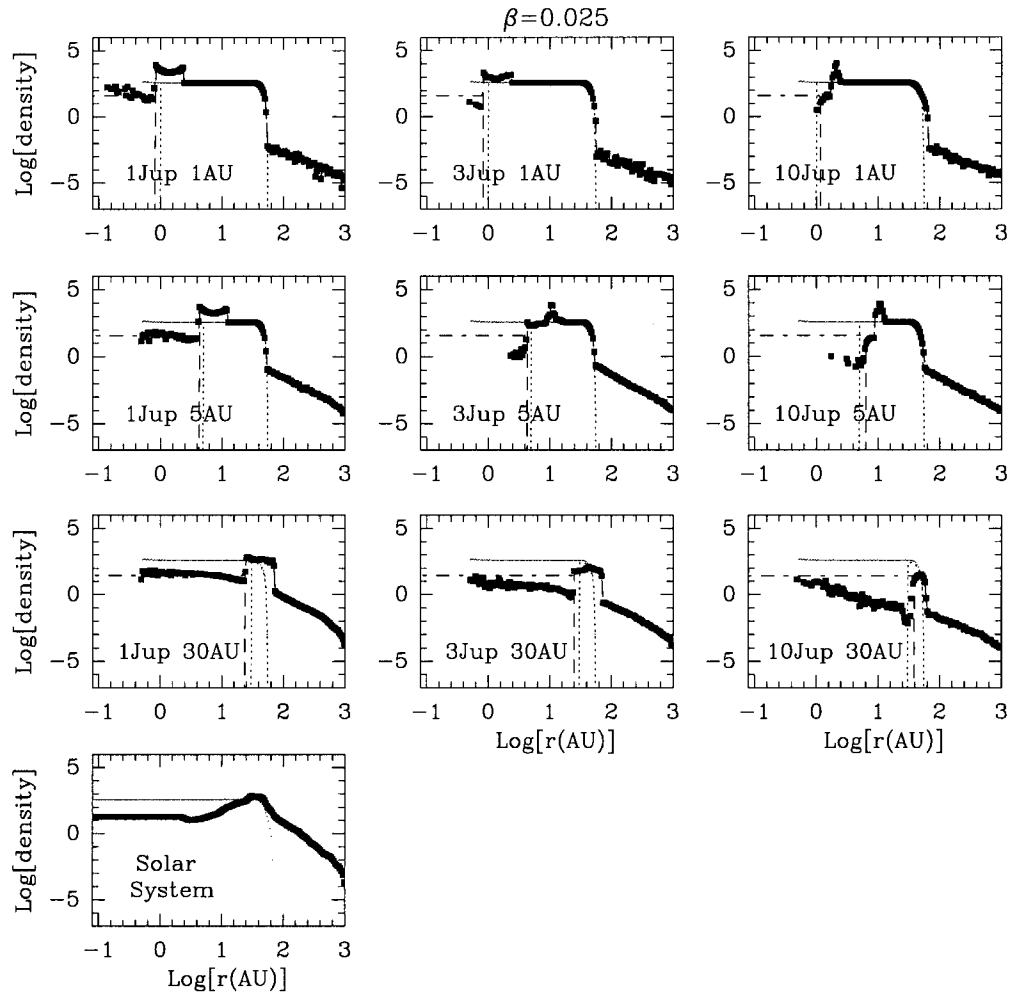


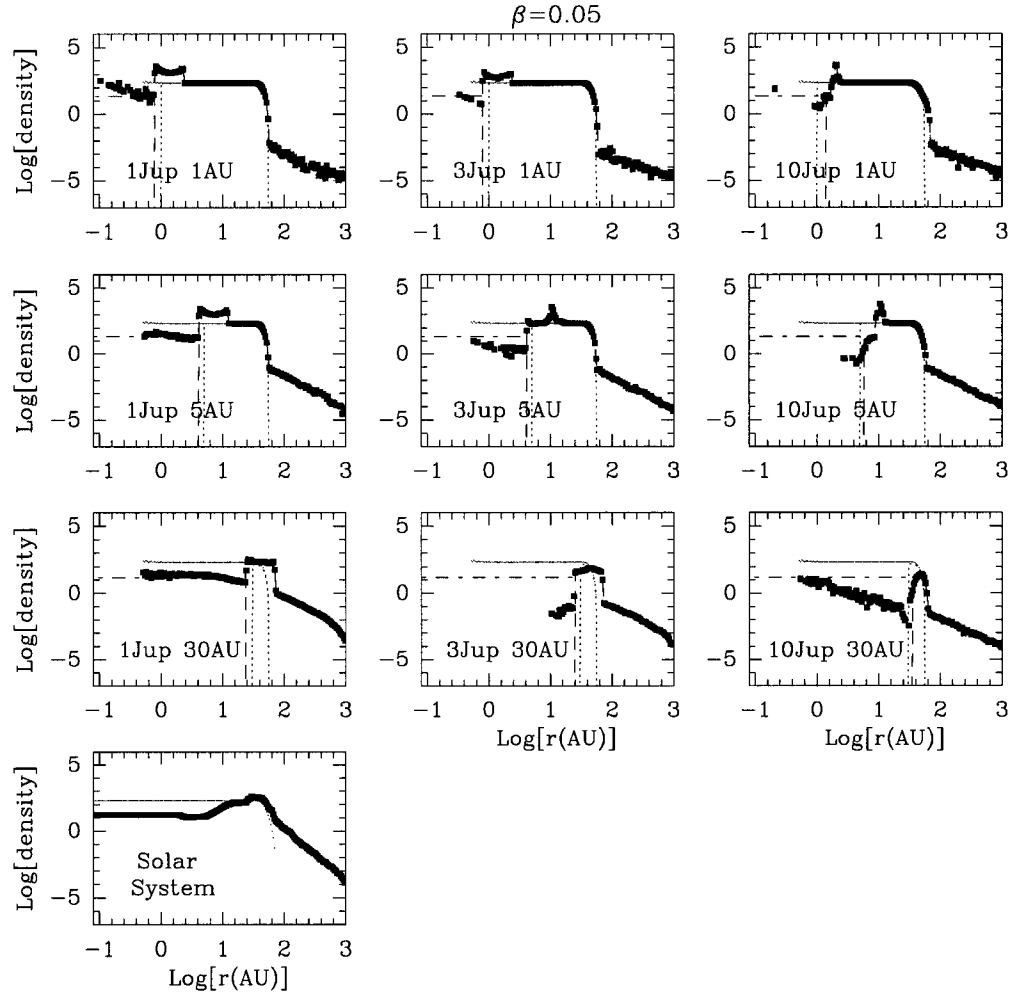
Figure 5.2: Surface density distribution (in arbitrary units) of dust particles with nine different β values (indicated at the top of the figure), for different planetary systems (indicated in the individual panels). *Large dots*: results from the dynamical simulations when the gravitational perturbation of the planet is taken into account. *Dashed line*: surface density distribution with “empty gap”. *Dashed – dotted line*: surface density distribution with “partial gap”. *Small dots* (or continuous line): results from the dynamical simulations when no planets are present. *Dotted line*: “analytical” surface density distribution with gap at the planet’s position.

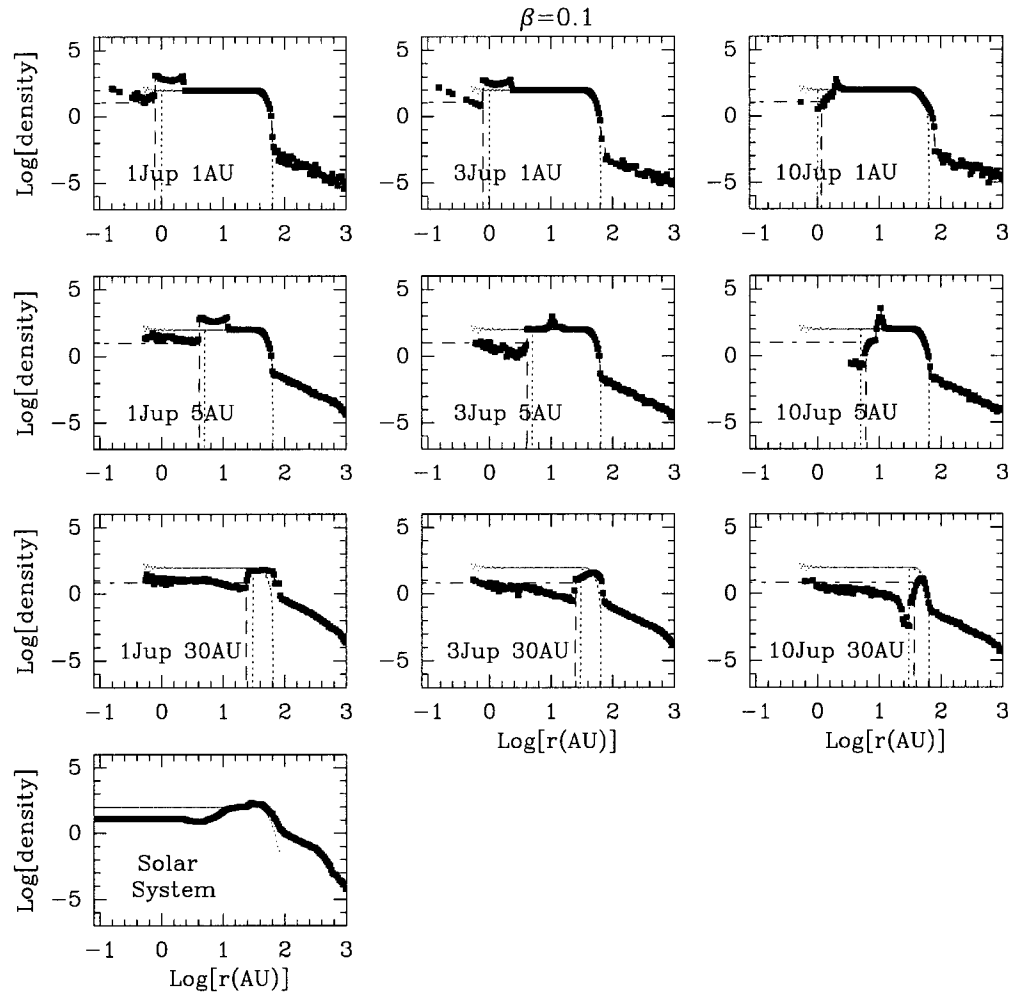


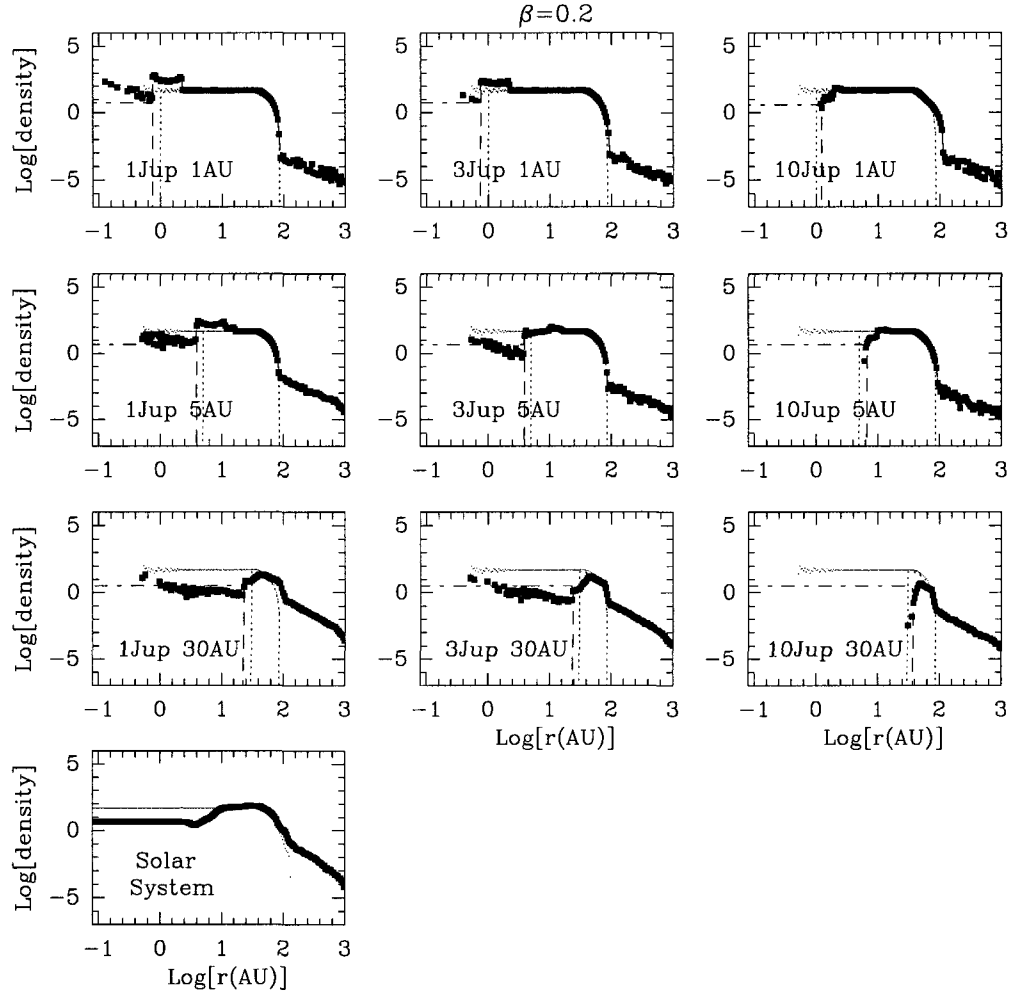


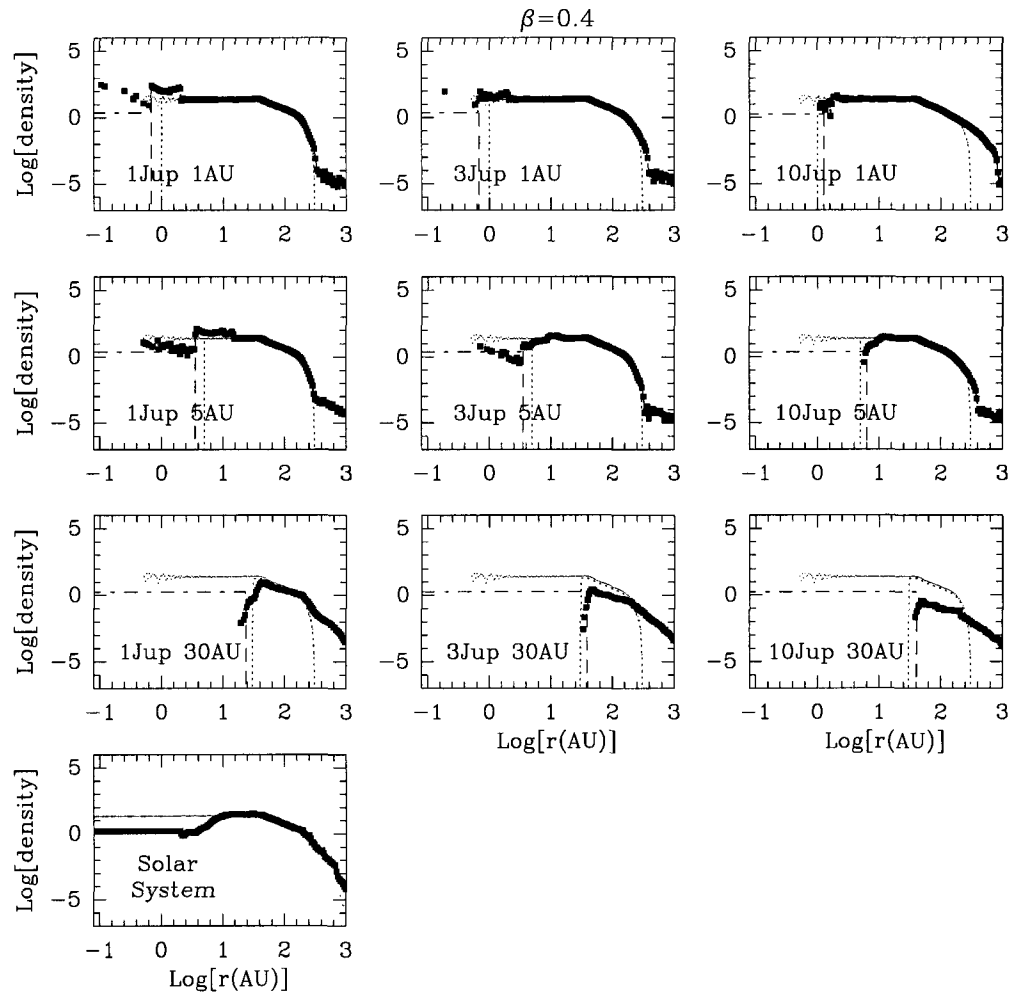












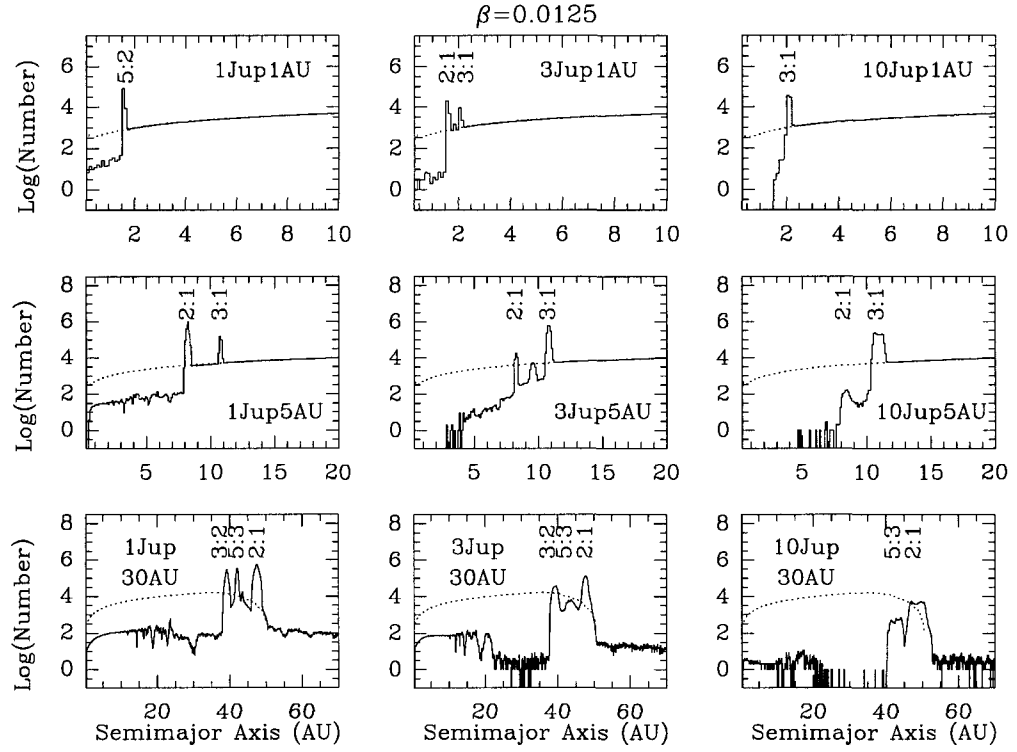


Figure 5.3: “Equilibrium” semimajor axis distributions in logarithmic scale of the dust particles with $\beta=0.0125$, in different single-planet systems (indicated in the individual panels; *solid line*). The *dotted line* correspond to a system without planets. The trapping of particles in the exterior MMRs with the planet, and the depletion of particles inside the planet’s orbit are the most prominent features in the figure.

Table 5.1: Final fate of Kuiper Belt dust grains - Estimate of uncertainties.

a: Planet of last encounter.

b: Parent bodies distributed between $a=35\text{--}50$ AU; $q=35\text{--}50$ AU and $i=0\text{--}17^\circ$.

c: Parent bodies with $a=45$ AU; $e=0.1$ AU and $i=10^\circ$. For $\beta=0.1$, 3 different sets of 100 particles each were run.

d: Results from Liou et al. (1996); parent bodies with $a=45$ AU; $e=0.1$ AU and $i=10^\circ$.

Result	Model	$\beta=0.01$	$\beta=0.05$	$\beta=0.1$	$\beta=0.2$	$\beta=0.4$
Ejected ^a :						
Jupiter	Models II-A ^b	32	38	44	40	20
	Models I-A ^c	39	47	40,38,36	31	30
	LZD96 ^d		45	35	35	45
Saturn	Models II-A ^b	37	28	23	31	32
	Models I-A ^c	35	26	20,27,27	34	36
	LZD96 ^d		30	40	40	35
Uranus	Models II-A ^b	5	8	6	6	13
	Models I-A ^c	3	4	2,4,7	5	9
	LZD96 ^d		0	0	0	0
Neptune	Models II-A ^b	13	4	3	8	21
	Models I-A ^c	17	2	9,6,7	8	18
	LZD96 ^d		0	5	5	5
Drift in	Models II-A ^b	11	19	21	15	11
	Models I-A ^c	6	21	29,19,21	22	7
	LZD96 ^d		25	20	20	15

Table 5.2: Final Fate of Dust Grains.

n_{1000} : number of particles that reach 1000 AU.

n_{rmin} : number of particles that reach r_{min} (0.5 AU when the planet is at 5 and 30 AU, or 0.1 AU when the planet is at 1 AU).

n_{drift} : number of particles that reach r_{min} with aphelion outside the planet's orbit ($a_{pl} - 3.5 \times r_{Hill}$).

n_{col} : number of particles that collide with the planet.

Parent bodies with $a=35\text{--}50$ AU, $e=0\text{--}0.05$ and $i=0\text{--}0.05$ radians.

M_{planet} (M_{Jup})	a	β	n_{1000}	n_{rmin}	n_{drift}	n_{col}
1	1	0.00156	88	6	1	6
3	1		80	19	0	1
10	1		95	5	0	0
1	5.2		85	15	1	0
3	5.2		90	10	0	0
10	5.2		96	4	0	0
1	30		69	1	1	0
3	30		69	0	0	1
10	30		68	0	0	2
1	1	0.00312	85	10	5	5
3	1		91	8	0	1
10	1		98	1	0	1
1	5.2		88	12	3	0
3	5.2		81	17	0	2
10	5.2		98	2	0	0
1	30		68	2	2	0
3	30		68	0	0	2
10	30		68	0	0	2
1	1	0.00625	83	9	5	8
3	1		80	14	3	6
10	1		93	7	0	0
1	5.2		80	19	8	1
3	5.2		88	12	0	0
10	5.2		93	7	0	0
1	30		62	8	8	0
3	30		68	1	1	1
10	30		67	0	0	3

M_{planet} (M_{Jup})	a	β	n_{1000}	n_{rmin}	n_{drift}	n_{col}
1	1	0.0125	81	17	16	2
3	1		87	5	5	8
10	1		95	5	0	0
1	5.2		86	14	10	0
3	5.2		92	8	0	0
10	5.2		97	3	0	0
1	30		66	4	4	0
3	30		65	5	5	0
10	30		67	1	1	2
1	1	0.025	76	23	23	1
3	1		83	7	2	10
10	1		93	7	0	0
1	5.2		83	17	17	0
3	5.2		83	14	0	3
10	5.2		91	9	0	0
1	30		59	11	11	0
3	30		67	2	2	1
10	30		65	1	1	4
1	1	0.044	58	39	39	3
3	1		91	7	7	2
10	1		89	11	0	0
1	5.2		75	25	25	0
3	5.2		88	12	2	0
10	5.2		95	5	0	0
1	30		58	11	11	1
3	30		68	0	0	2
10	30		67	2	2	1

M_{planet} (M_{Jup})	a	β	n_{1000}	n_{rmin}	n_{drift}	n_{col}
1	1	0.1	55	43	43	2
3	1		77	18	18	5
10	1		94	5	2	1
1	5.2		61	38	38	1
3	5.2		84	14	13	2
10	5.2		90	10	0	0
1	30		57	11	11	2
3	30		67	3	3	0
10	30		66	2	2	2
1	1	0.2	50	47	47	3
3	1		80	17	17	3
10	1		91	0	0	9
1	5.2		67	32	32	1
3	5.2		91	8	8	1
10	5.2		95	0	0	5
1	30		66	3	3	1
3	30		68	2	2	1
10	30		70	0	0	0
1	1	0.4	56	39	39	5
3	1		88	7	7	5
10	1		93	0	0	7
1	5.2		75	24	24	1
3	5.2		95	5	5	0
10	5.2		95	0	0	5
1	30		70	0	0	0
3	30		70	0	0	0
10	30		70	0	0	0

surface density from the numerical results decreases by more than 90%. Outside the gap, the surface density distribution follows the results from the dynamical models (large dots).

2. *Partial Gap* models: same as above but with the inner hole being 90% depleted in dust with respect to the disk without planets (instead of being totally empty). In this case, we are extrapolating the surface density of dust from a distance near the planet's orbit down to 0.01 AU, to account for the sublimation distance of the larger silicate grains. The detailed calculation of the sublimation distance is done by the radiative transfer code, and depends on the grain radius and chemical composition. The extrapolation is done assuming a flat surface density distribution, expected for a collisionless system with grains in circular orbits. The caveat is that when planets are present the dust grains that drift inward may have a non-zero eccentricity, so the surface density will not be exactly flat.
3. *Analytical Gap* models: the surface density distribution consists on a simple square profile, following the flat density distribution of the disk without planets, with an empty gap at the planet's position (i.e. it does not account for particles trapped in the MMRs).

The comparison of the SEDs that arise from the model with an *empty gap* and the model with a *partial gap* can teach us if the dynamical models are *sufficient* to distinguish the presence of planets of masses ranging from 1–10 M_{Jup} and semi-major axis of between 1–30 AU. If we find that the SEDs arising from these two models are significantly different, the number of particles studied ($N \sim 100$) would not be sufficient, as it does not allow us to distinguish between an empty gap and a partial gap with 10% of particles left. The comparison of the SEDs that arise from the *empty gap* and the *analytical gap* models can teach us if the dynamical models are *necessary*, or whether it is adequate to assume a flat surface density distribution

with a clean gap inward of the planet’s location (ignoring the accumulation of dust particles in the MMRs).

The calculation of these radial density distributions is the most CPU demanding step, but it is independent of the rest of the steps outlined in the Introduction because the dynamical models and the resulting radial density profiles depend only on the parameter β . It is only *a posteriori* that we find the relationship between the particle size and composition and the β value, with a single β value corresponding to several combinations of grain size and composition (see Figure 5.4). Because of this degeneracy, our scheme allows enough flexibility to efficiently explore other grain chemistries without the need of recomputing the radial density profiles.

5.3 Correspondence between β and Particle Size

The quantity β is the dimensionless ratio of the radiation pressure force and the gravitational force. For spherical grains and a solar type star, $\beta = 5.7 \times 10^{-5} Q_{pr}/(\rho a)$, where ρ and a are the density and radius of the grain in cgs units (Burns et al., 1979), and Q_{pr} is the radiation pressure coefficient. Before using the radial density distributions as input for the radiative transfer code in WH03, we need to find the correspondence between the value of β and the particle size, and this depends on the grain chemical composition. Based on spectroscopic observations of debris disks and evolved stars, the following chemical compositions were selected: MgSiO_3 and $\text{Mg}_{0.6}\text{Fe}_{0.4}\text{SiO}_3$ (Fe-poor and Fe-rich pyroxene), MgFeSiO_4 and $\text{Mg}_{1.9}\text{Fe}_{0.1}\text{SiO}_4$ (amorphous and crystalline olivine), and C400 and C1000 [400 K carbon modification (graphite-poor) and 1000 K carbon modification (graphite-rich), respectively]. This is a subset of the compositions studied in WH03; we refer to this paper for a justification of this selection and a description of the optical properties of these silicate and carbon species.

For each selected chemistry, using Mie scattering theory and assuming that the grains are homogeneous spheres, we compute the grain optical parameters, needed to calculate dust absorption, reemission and scattering of radiation. We obtain Q_{pr} as a function of wavelength for a large number of particle sizes. The quantity Q_{pr} is a function of the grain complex refractive indexes (n, k), the grain radius, and the wavelength of the incoming radiation. The refractive index for the silicates and carbonaceous materials are taken from Dorschner et al. (1995) and Jäger et al. (1998), respectively². We then obtain the average of Q_{pr} integrated over the solar spectrum (Labs and Neckel, 1968). This average is used to calculate the value of β , for each particular dust chemistry under consideration, and for a large number of particle sizes (see Figure 5.4). Finally, we select the particle size whose β is closer to the β -value adopted in the dynamical models. One important feature to notice from Figure 5.4 is that, for a given particle size, the value of β corresponding to carbonaceous and Fe-rich silicate grains is larger than that of Fe-poor silicates, because the former have a very high absorptive efficiency in the wavelength range on which the star emits. This is important because a small change in the abundance of carbonaceous and Fe-rich silicate material can make a very significant change in the level of the continuum emission.

The parameter study in WH03 showed that the shape of the SED is affected by the relative number of small grains, which is determined by the minimum (a_{min}) and maximum (a_{max}) grain size, and by the index (q) of the power law size distribution ($n(a)da = n_0 a^{-q}$): an increase of net flux and the prominent emission features occur when a_{min} is decreased and q is increased. For β Pic, MIR observations indicate that there is a substantial amount of grains $< 10 \mu\text{m}$ inside 20 AU (Weinberger et al., 2003), while others suggest $a_{min} \approx 0.1 \mu\text{m}$ (Pantin et al., 1997). For Fomalhaut, submillimeter observations indicate $a_{min} \approx 0.7 \mu\text{m}$. In this chapter $a_{min} = 0.5\text{--}1.3 \mu\text{m}$ (depending on composition), and is determined by the

²The complex refractive indexes are available at <http://www.astro.uni-jena.de/Laboratory/Database/odata.html>.

condition $\beta=0.5$, corresponding to particles that are forced into hyperbolic orbits as soon as they are released from their parent bodies. If the parent bodies' orbits have eccentricity e , ejection occurs for $\beta > 0.5(1-e)$ and $\beta > 0.5(1+e)$ for particle release at periastron and apoastron, respectively. We are therefore implicitly assuming that radiation pressure is the only process responsible for the minimum grain size, but in practice a_{min} is also affected by collisional processes. The maximum grain size in our simulations is limited by the CPU time, as particles with very small β s (0.00156 is our minimum value) have a very slow dynamical evolution. Depending on the chemical composition chosen, $a_{max}=53\text{--}244\text{ }\mu\text{m}$. Debris disks certainly contain larger “dust” particles, up to planetesimal size, but in the wavelength range considered grains larger than $\sim 1\text{ mm}$ will not contribute significantly to the SED, and the missing grains in the $53\text{--}240\text{ }\mu\text{m}$ to 1 mm range only add an almost featureless continuum, as indicated in the study by WH03.

5.4 Spectral Energy Distributions

Once the particle size is known for each β value and selected chemical composition, we use the surface density distributions as input for a radiative transfer code that calculates the emitted dust SED (plus the stellar scattered light). As in WH03, we assume that the disk is optically thin: only scattering, absorption and reemission of stellar radiation by dust grains are taken into account, neglecting multiple scattering and radiation and dust heating due to dust reemission. The dynamical models are only valid in a density regime that corresponds to optically thin disks. For the central star we use the solar SED published by Labs and Neckel (1968), $0.2\text{--}100\text{ }\mu\text{m}$, extended by a blackbody SED ($T=5800\text{ K}$) beyond $100\text{ }\mu\text{m}$. The dust reemission and scattering are calculated at 500 logarithmically equidistantly distributed wavelengths between $5\text{--}340\text{ }\mu\text{m}$ (which includes the wavelengths covered by *Spitzer*). We assume a disk mass of $10^{-10}M_{\odot}$ and a distance of 50 pc . Note that

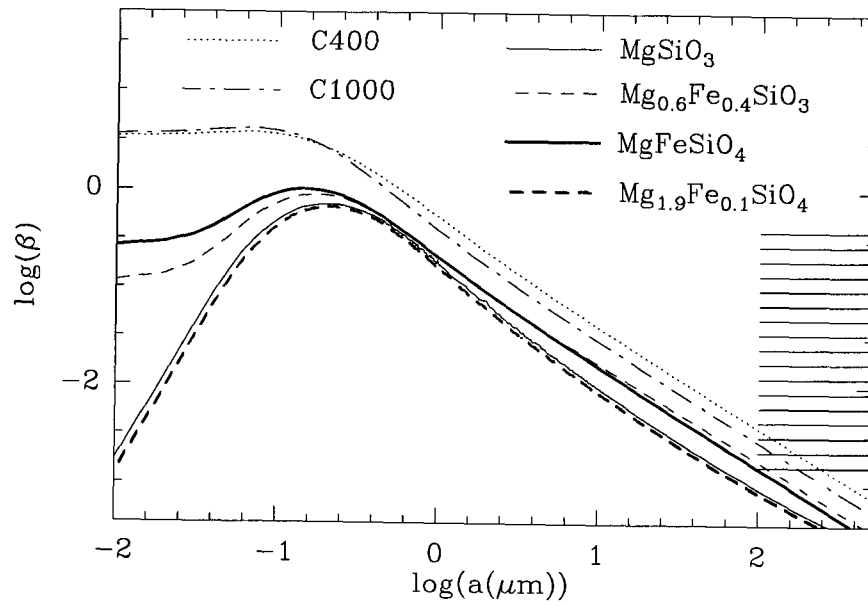


Figure 5.4: Correspondence between β and particle radius for the grain chemical compositions under consideration. The horizontal lines at the far right indicate the values of β used in the dynamical models.

Table 5.3: β -particle radius (μm) relation.

NOTE.—Grain densities, assuming homogeneous spheres are: 2.71 (MgSiO_3), 3.1 ($\text{Mg}_{0.6}\text{Fe}_{0.4}\text{SiO}_3$), 3.71 (MgFeSiO_4), 3.3 ($\text{Mg}_{1.9}\text{Fe}_{0.1}\text{SiO}_4$), 1.435 (C 400) and 1.988 (C1000) g cm^{-3} . Grain radii are given in μm for different values of β and chemical compositions of the dust grains.

a:Crystalline Olivine.

b: β values used for the single-planet models.

β	MgSiO_3	$\text{Mg}_{0.6}\text{Fe}_{0.4}\text{SiO}_3$	MgFeSiO_4	$\text{Mg}_{1.9}\text{Fe}_{0.1}\text{SiO}_4^a$	C 400	C 1000
0.4 ^b	0.53	0.59	0.58	0.50	1.3	0.99
0.2828	0.73	0.78	0.78	0.67	1.7	1.3
0.2 ^b	0.93	1.0	1.1	0.86	2.3	1.8
0.1414	1.2	1.4	1.4	1.1	3.2	2.4
0.1 ^b	1.5	1.8	1.8	1.3	4.3	3.2
0.0707	2.0	2.5	2.5	1.8	6.0	4.4
0.05 ^b	2.5	3.4	3.4	2.3	8.2	6.1
0.03535	3.4	4.8	4.7	3.0	11.4	8.4
0.025 ^b	4.4	6.7	6.4	4.0	15.9	11.7
0.01767	5.8	9.6	8.9	5.4	22.3	16.3
0.0125 ^b	8.0	13.7	12.4	7.1	31.2	22.7
0.008838	10.7	19.5	17.4	9.7	43.8	31.9
0.00625 ^b	14.8	27.8	24.3	13.3	61.6	44.8
0.00442	20.4	39.6	34.2	18.4	86.8	63.0
0.00312 ^b	28.6	54.8	48.1	25.7	122.7	89.0
0.00221	40.3	80.0	67.6	36.1	172.8	125.3
0.00156 ^b	57.3	113.5	95.5	51.4	244.5	177.2

our models (with and without planets) contain the same amount of disk mass. We are interested in studying how the structure created by the planets affects the shape of the SED, independent of the dust production rate. However, planetary perturbations can affect the dust production rate, possibly leading to more massive dust disks. This effect is not taken into account in our models, but will be considered in the future.

Figure 5.5 shows the SEDs that result from the Solar System models. Each of the nine panels corresponds to the SEDs that arise from single particle size disks (of one particular β value, indicated at the bottom of each panel. We only show nine β values of the 17 computed). Each set of nine panels corresponds to a particular grain chemical composition (indicated in the upper left panel). In Figure 5.6 we compare the emission arising from the different compositions (keeping the particle size approximately constant). In agreement with WH03, the most important features shown in these figures are:

1. Emission is stronger for Fe-rich silicates ($\text{Mg}_{0.6}\text{Fe}_{0.4}\text{SiO}_3$ and MgFeSiO_4) compared to Fe-poor (MgSiO_3 and $\text{Mg}_{1.9}\text{Fe}_{0.1}\text{SiO}_4$). This is due to the strong dependence of the UV-to-NIR absorption efficiency on the Fe content, which leads to higher grain temperatures at a given distance from the star as the Fe content increases.
2. Similarly to Fe-rich silicates, carbonaceous grains also lead to stronger but featureless emission (mainly adding a continuum).
3. The emission peak shifts to longer wavelengths as the particle size increases (or β decreases). This is due to the fact that the turnover point beyond which the absorption efficiency decreases continuously increases with grain size.
4. The clearing of dust from the inner 10 AU results in a loss of warm dust and is responsible for the decrease in the NIR/MIR region (compared to the case

when no planets are present). The slight shift in the emission peaks indicate that some of this NIR/MIR emission is radiated at longer wavelengths, but this is a very small effect because once the particles are set on hyperbolic orbits after their last gravitational encounter with the giant planet, they leave the system very quickly without contributing significantly to the emission. The net flux decreases because a larger fraction of the grains are further away from the star, so the fraction of stellar photons that the grains can absorb and later re-emit is diminished.

Similarly, but not shown here, we have calculated single particle size and single composition SEDs for the other planetary systems studied (i.e. the nine single-planet models and the system without planets). These SEDs show features similar to those described above for the Solar System.

As Figure 5.2 shows, the structure of the dust disk is significantly different depending on the particle size under consideration. The structure is more pronounced for larger particle sizes because the trapping in resonances is more efficient when the drag forces are small. However, it is expected that the dust production processes will favor the generation of small particles. The modeling of debris disk structure and SED should therefore take into consideration an appropriate range of particle sizes that can later be weighted and combined to emulate a particle size distribution. In Chapter 3 we estimated the radial distribution of KB dust from our dynamical models and the KB dust production rate estimates from Landgraf et al. (2002). We showed that the dust particle size distribution in space is significantly changed from its distribution at production, due to the combined effects of radiation forces and the perturbations of the planets. With these results in mind, the single particle size and single composition SEDs for each planetary system (like those shown in Figure 5.5 for the Solar System) are weighted and combined in such a way that the particle size distribution follows power laws of indexes $q=2.5$, 3.0 and 3.5 . [Note that when collisional processes are considered in detail, the particle

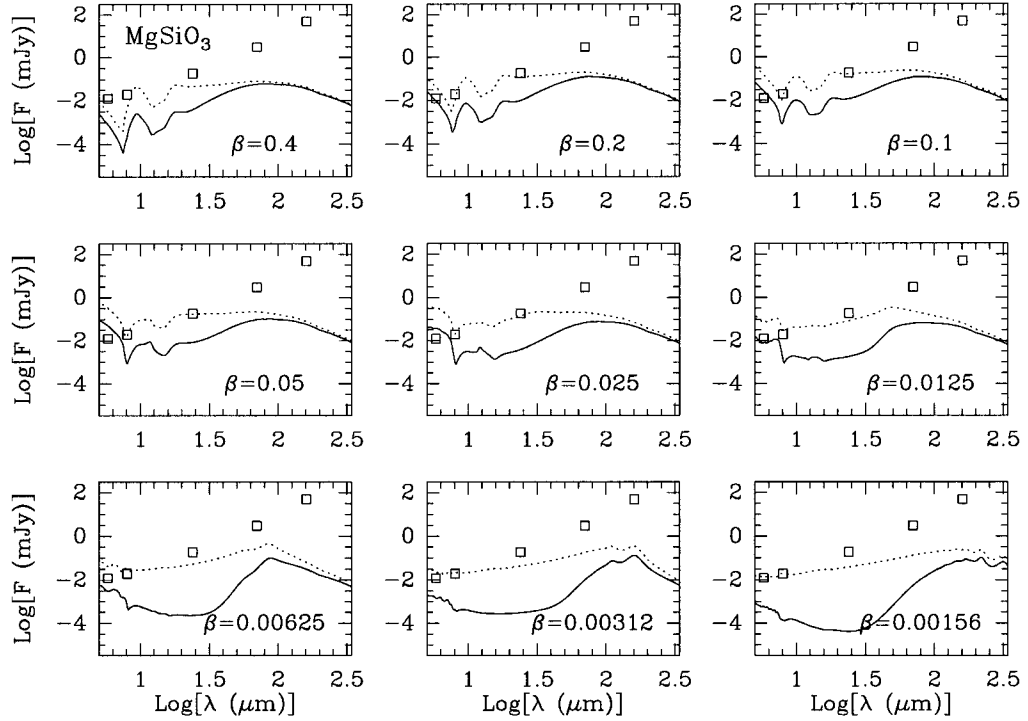
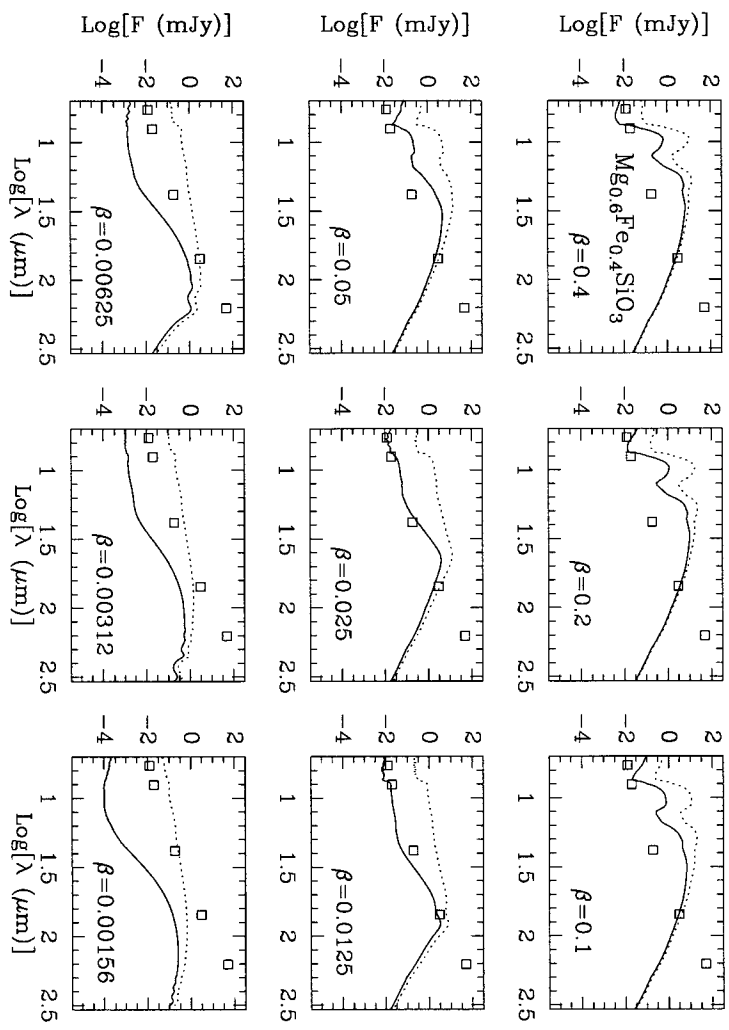
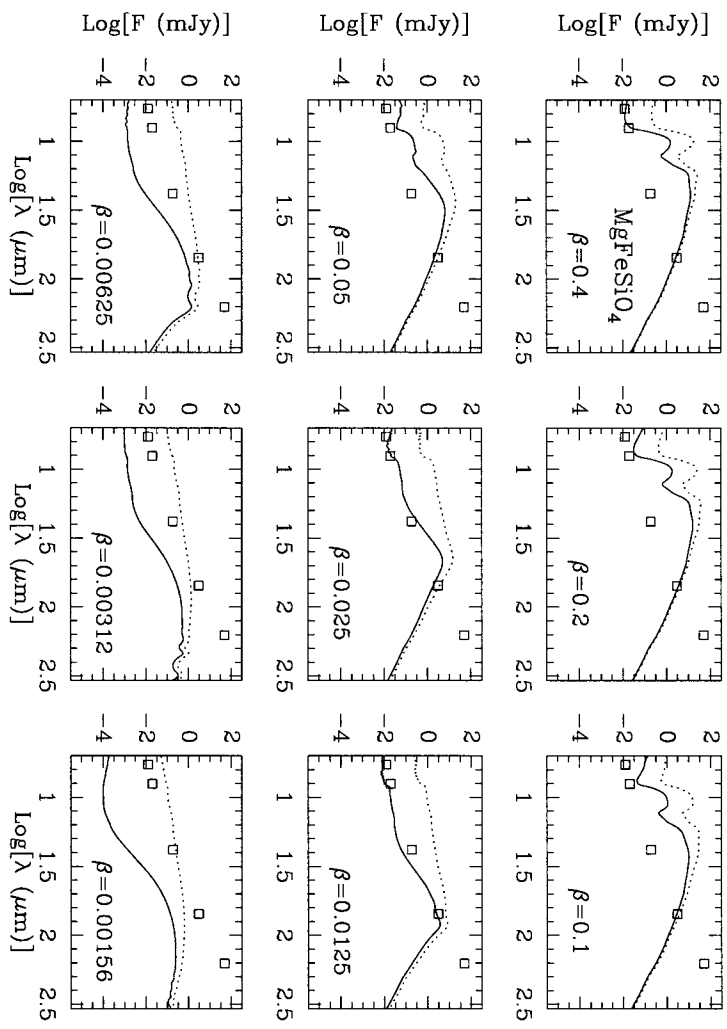
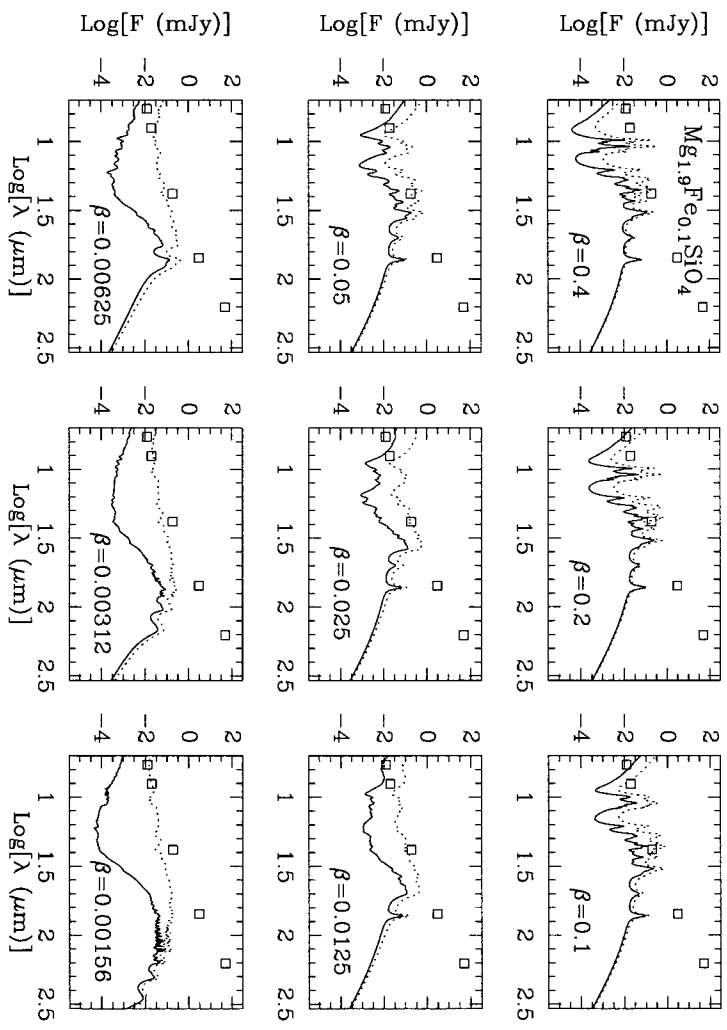
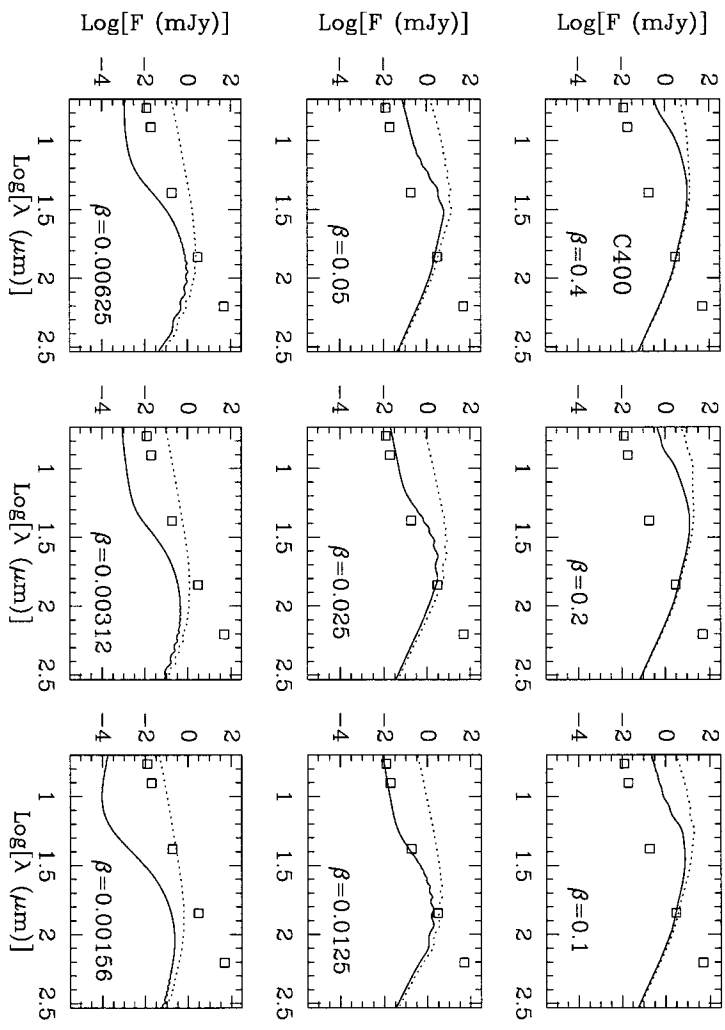


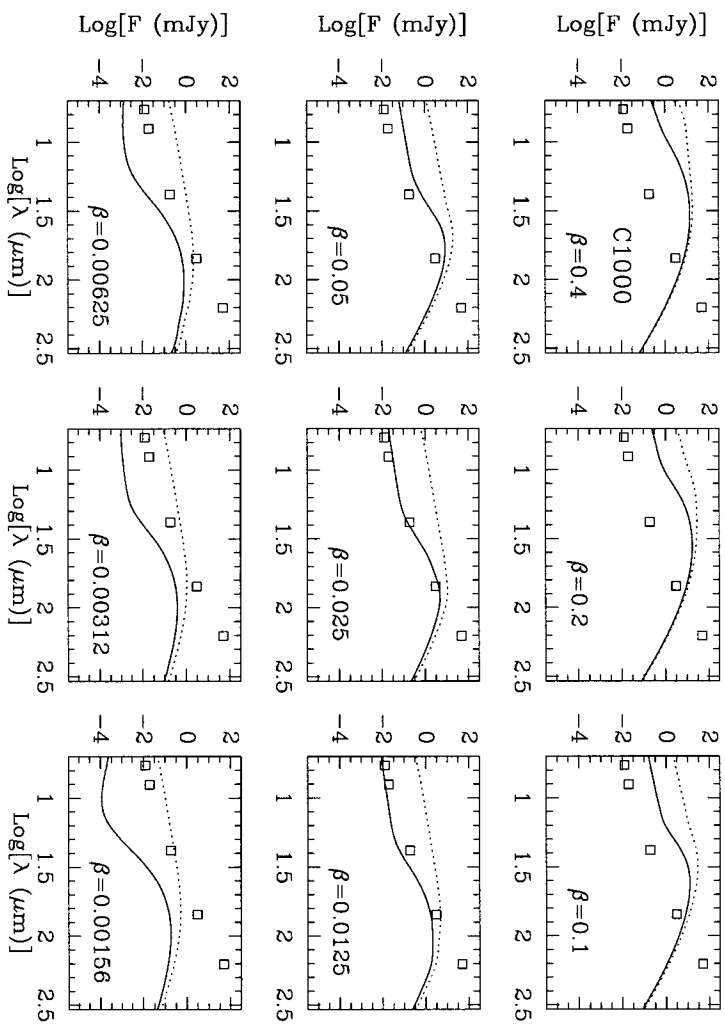
Figure 5.5: SEDs of single particle size disks from the Solar System models. Each panel corresponds to one particular β value, indicated in the figure. Each set of nine panels corresponds to a particular grain chemical composition (indicated in the upper left panel): The *Solid* line is for a system with 7 planets; the *dotted* line is for a system without planets. In all cases the disk is assumed to be at distance of 50 pc and has a mass of $10^{-10}M_{\odot}$. The squares indicate *Spitzer* 5- σ detection limits.











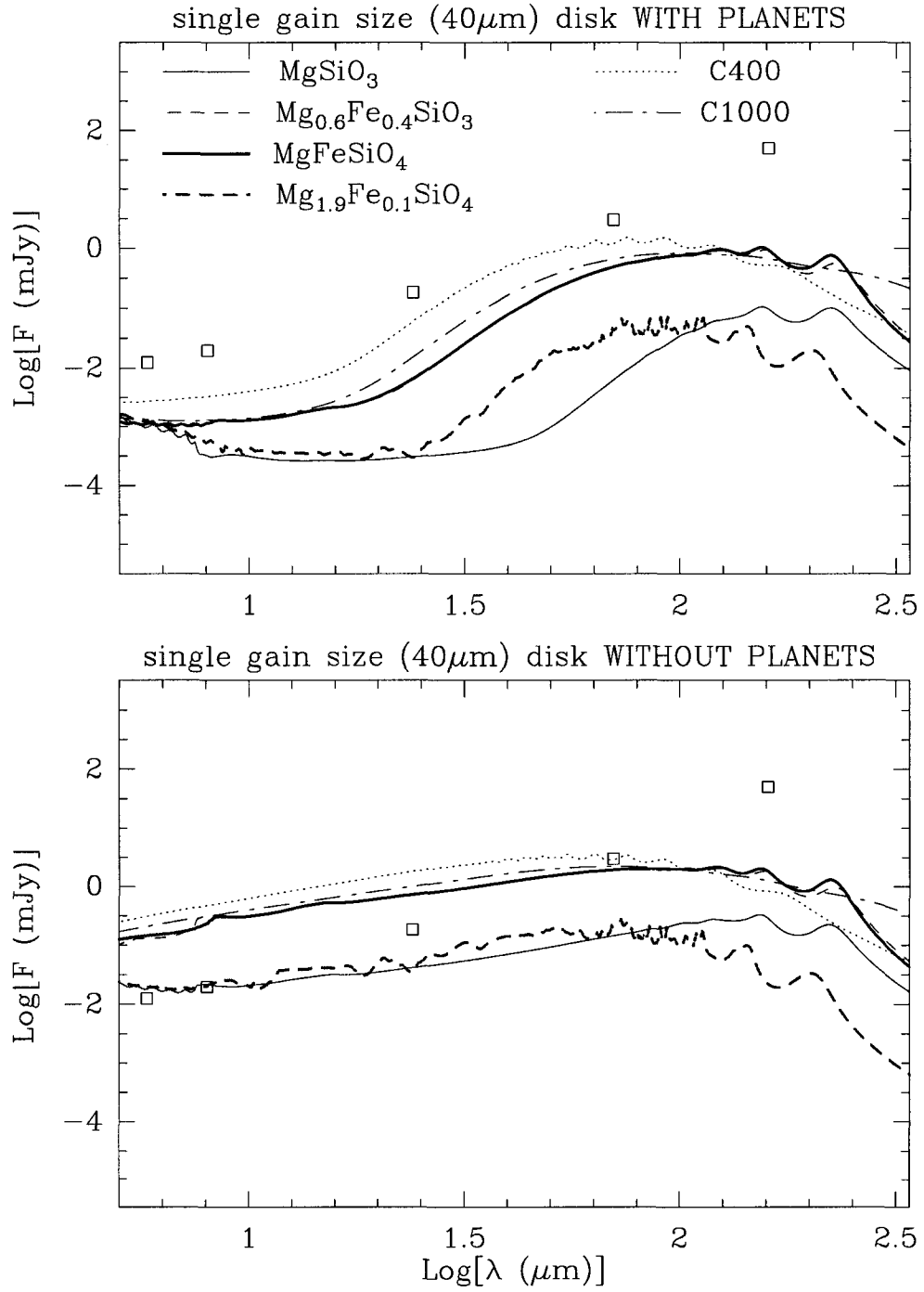
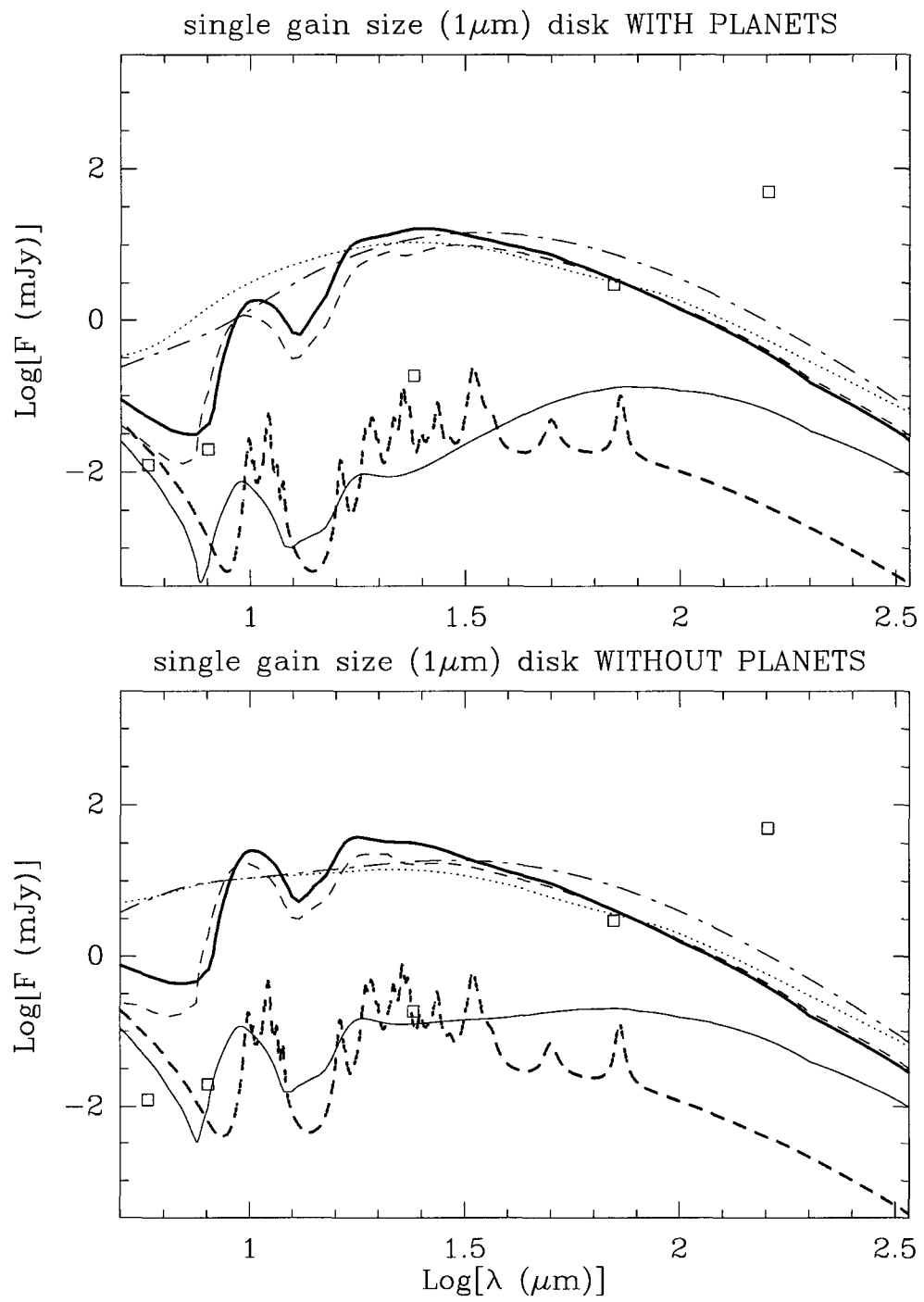


Figure 5.6: SEDs of disks composed of $1 \mu\text{m}$ and $40 \mu\text{m}$ grains, from the Solar System models, and with different grain chemical compositions.



strengths are size-dependent, leading to a size-dependent q ; and because the particle growth/collision processes depends on the radial distance from the star, q will also be a function of radius. Here, we will ignore these effects and consider a single power law to describe the particle size distribution at all distances from the star and for all particle sizes.] The top panel of Figure 5.7 shows that the flux is higher, specially in the NIR/MIR range, and the spectral features are more pronounced when the particle size distribution is steeper (i.e. there is a larger fraction of smaller grains). This is because small grains achieve higher temperatures. In WH03 it was found that because of this effect, the presence of a gap, and consequently the removal of warm grains, lead to a more pronounced decrease of flux in the NIR/MIR range when a larger fraction of smaller grains were present (steeper power law). Figure 5.7 (bottom) suggest exactly the opposite trend, as the ratio of the SEDs that arise from a system with a planet (using the empty gap models) to that from a system without a planet (i.e. without a “gap”) is smaller for smaller power law indexes. The discrepancy between this result and the one in WH03 arises from the difference between the analytic density distributions used in WH03, and the density distributions used here; the latter showing a large difference between the system with planets and the system without planets, which is more pronounced for larger grains (smaller β) than for smaller grains (larger β ; see Figure 5.2). This means that the difference between the mean disk temperatures in the system with planets and that of the system without planets is more pronounced when large particles are dominant, leading to more distinct differences in their corresponding SEDs. This illustrates the importance of combining numerical tools for the simulation of debris disk structure with a detailed radiative transfer code for the calculation of their emergent SEDs.

The SEDs that result after combining the different grain sizes are shown in Figure 5.8 to 5.17 (left) and correspond to a single grain chemical composition (indicated in each panel) but allow for a distribution of particle sizes (with each line

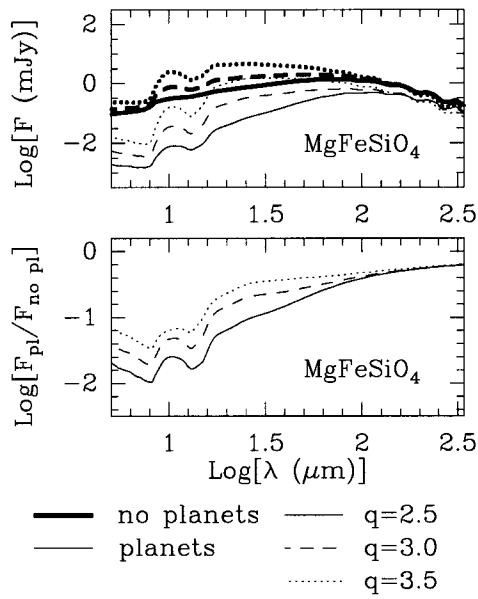


Figure 5.7: (*Top panel*) SEDs of dust disks composed of MgFeSiO_4 grains, for three particle size distribution: $n(b)db = n_0 b^{-q}$, with $q=2.5$ (*solid line*), 3.0 (*dashed line*) and 3.5 (*dotted line*). *Thick line*: system without planets; *Thin line*: system with Solar System-like planets. The system is at a distance of 50 pc and has a total disk mass of $10^{-10} M_{\odot}$. (*Bottom panel*) Ratio of the composed SED arising from a system with planets to that of a system with no planets.

type corresponding to a different power law index for the particle size distribution). Each figure corresponds to a different planetary system (indicated at the top). The thin lines in Figures 5.8 to 5.17 (right) show the ratios of the SEDs that arise from a system with a planet (using the empty gap models) to that from a system without a planet (i.e. without a “gap”). In the following, we refer to this ratio as $F_{planet}/F_{no\ planet}$, where F is the flux arising from the dust disk. Similarly, we show $F_{partial\ gap}/F_{empty\ gap}$ and $F_{empty\ gap}/F_{analytical\ gap}$ (solid and dashed lines, respectively).

The SED depends on the grain chemical composition. For example, Figure 5.8 shows that for carbonaceous and Fe-rich silicates grains, the minimum in the SED of a dust disk with Solar System-like planets is at $\lambda < 8\ \mu\text{m}$, while for Fe-poor silicate grains the minimum shifts to longer wavelengths, $\lambda = 10\text{--}25\ \mu\text{m}$. A similar effect is also found for the other single-planet systems studied. Similarly, the minimum of $F_{planet}/F_{no\ planet}$ occurs at $\lambda < 10\ \mu\text{m}$ for carbonaceous and Fe-rich silicates grains, and $\sim 15\ \mu\text{m}$ for Fe-poor silicate grains, i.e., the wavelength range where the difference between the SED arising from a disk with Solar System-like planets and that of a disk without planets is the largest depends on the chemical composition of the grains. As it can be seen from Figures 5.8 to 5.17 (right), in many cases the largest difference between F_{planet} and $F_{no\ planet}$ occurs at wavelengths where the photospheric emission from the star dominates, making the photospheric subtraction critical in the analysis of observed SEDs in terms of planetary architectures.

Figures 5.8 to 5.17 (right) show that for a planet at 1 AU, the differences between the “empty gap” and the “analytical gap” models are large, with $F_{empty\ gap}/F_{analytical\ gap}$ up to 100 for $1M_{Jup}$, and 30 for $10M_{Jup}$ (dashed lines). This is due the fact that the “analytical gap” models follow a square profile, while the dynamical models contain a large number of particles accumulated in the MMRs with the planet (see Figure 5.2 and note that scale is logarithmic). These particles, being at small astrometric distances, are hot and contribute very significantly to the

SED. We can conclude that dynamical simulations are necessary to model the SEDs of debris disks in the presence of planets at small semimajor axis (hot Jupiters), because the enhancement of particles at the MMRs dominates the emission. A consequence of this is that it should be possible to distinguish observationally between a simple square profile for the surface density of the dust disk, as that created by a stellar wind or by the interaction of the dust grains with ambient gas, from the surface density created by the dynamical interactions with a massive planet.

Figures 5.8 to 5.17 (right) also show that for a planet at 1 AU, the ratio $F_{planet}/F_{no\ planet}$ (solid lines) is greater than 1 for $\lambda=8\text{--}60\ \mu\text{m}$ for carbonaceous and Fe-rich silicate grains, and $\lambda=20\text{--}80\ \mu\text{m}$ for Fe-poor silicate grains. Even though the disk with a planet has an inner hole, it can be up to 3 times brighter than the disk without a planet. This is because the particles accumulated in the MMRs contribute importantly to the SED. The system with $10M_{Jup}$ at 1 AU, however, is not significantly brighter than the system without planet. This does not mean that the analytical square profiles are sufficient for $10M_{Jup}$ at 1 AU, because as we saw above, $F_{empty\ gap}/F_{analytical\ gap} \sim 30$. The ratio $F_{planet}/F_{no\ planet}$ is very close to 1, for $\lambda > 80\ \mu\text{m}$ for $1M_{Jup}$ at 1 AU, and $\lambda > 24\ \mu\text{m}$ for $10M_{Jup}$ at 1 AU. In this wavelengths ranges, either the effect of the particles accumulated in the resonances is not important, or their effect on the SED is balanced by the depletion of hot grains close to the star.

The “partial gap” and “empty gap” models are very similar for $1M_{Jup}$ at 1 AU ($F_{partial\ gap}/F_{empty\ gap} \sim 1$; dotted lines). For a $10M_{Jup}$ planet at 1 AU, $F_{partial\ gap}/F_{empty\ gap} \sim 3$, for $\lambda < 20\ \mu\text{m}$. But in this case, our models indicate that the number of particles that drift inward is probably 0, with an uncertainty smaller than 10%, which means that $F_{partial\ gap}/F_{empty\ gap}$ is probably overestimating the uncertainties in the prediction of the SED. We conclude from the small $F_{partial\ gap}/F_{empty\ gap}$ values that the uncertainties in our dynamical simulations, due to the small number of particles studied, do not affect the modeling of the

SEDs arising from dust disks with a planet at 1 AU. In other words, the number of particles in our simulations ($N \sim 100$) is sufficient to model these systems with close-in planets.

As we saw before, for $1M_{Jup}$ at 1 AU the accumulation of dust grains in the MMRs with the planet can increase the flux up to a factor of 100 compared to the flux arising from a disk with a simple square profile. For $1M_{Jup}$ at 5 AU, the maximum $F_{empty\ gap}/F_{analytical\ gap}$ decreases from ~ 100 to ~ 30 , and therefore the accumulation into the MMRs is not as important as at 1 AU (the particles are colder and their contribution is less dominant). But the difference between the “partial gap” and “empty gap” models is more pronounced at 5 AU ($F_{partial\ gap}/F_{empty\ gap} \sim 3-10$ for $1M_{Jup}$ and $10-30$ for $10M_{Jup}$) than at 1 AU ($F_{partial\ gap}/F_{empty\ gap} \sim 1$ for $1M_{Jup}$ and 3 for $10M_{Jup}$). [The number of particles that drift inward for $10M_{Jup}$ at 5 AU is probably 0 and not subject to the 10% uncertainty, so the factor of 10–30 is probably overestimated.] We conclude that the dynamical models are necessary to study the SEDs arising from systems with planets of $1-10M_{Jup}$ at 5 AU, because by not considering the particles accumulated in the MMRs, the SED can be underestimated by a factor of 30. But unlike the 1 AU models, the number of particles that we have used in our simulations ($N \sim 100$) is not sufficient because a 10% uncertainty in depletion factor yields to a factor of 3–10 and 10–30 (overestimated) in flux for 1 and $10M_{Jup}$, respectively.

The models at 30 AU represent a system with a narrow ring of dust producing planetesimals just outside the planet’s orbit. If a fraction of the dust particles drift inward, even if it is small, the shape of the SED is similar to the one arising from a system without planets. This is because like in the models without planets, there is no structure for a wide range of astrocentric distances. If the particles are held back (by trapping in resonances and gravitational scattering), the SED shows a large deficit in the mid-IR flux (whose wavelength depend on the location of the ring) that makes it very distinct from the SED from a system without planets (see

large minimum for $F_{planet}/F_{no\ planet}$ in Figures 5.8 to 5.17).

The “empty gap” and “analytical gap” models are very similar when the planet is at 30 AU, i.e. the accumulation of particles in the MMRs do not dominate the shape of the SED for planets at this distance. However, the “partial gap” models are very different from the “empty gap” models, with the 10% uncertainty in the number of particles that drift inward leading to a factor of 100–3000 difference in flux ($F_{partial\ gap}/F_{empty\ gap} \sim 100$, for $1M_{Jup}$ and $F_{partial\ gap}/F_{empty\ gap} \sim 1000\text{--}3000$, for $10M_{Jup}$). Because the SED is very sensitive to the number of particles that drift inward, this number needs to be determined precisely by dynamical models; the large factors indicate that the number of particles in our simulations ($N \sim 100$) is not sufficient to study systems with planets of $1\text{--}10M_{Jup}$ at 30 AU.

The ratio $F_{planet}/F_{no\ planet}$ can reach 0.3 for $1M_{Jup}$ at 1 AU, and 0.1 for $10M_{Jup}$ at 1 AU. This decrease is due to the fact that for the more massive planet the gap is larger ($r_{gap} \sim 0.8$ AU for $1M_{Jup}$, and ~ 1.6 AU for $10M_{Jup}$; see Figure 5.2), and more empty (larger number of particles are ejected). The different depletion factors explain why a disk with $1M_{Jup}$ at 1 AU (5 AU) is brighter than a disk with $10M_{Jup}$ at 1 AU (5 AU) by a factor of 3–10 (for $\lambda < 10\ \mu\text{m}$ for carbonaceous and Fe-rich silicate grains; and λ between 10–24 μm for Fe-poor silicate grains). The different gap radius makes the disk with a $1M_{Jup}$ at 1 AU be 100 (3000) times brighter than a disk with $1M_{Jup}$ at 5 AU (30 AU) (for $\lambda < 24\ \mu\text{m}$, if the grains have carbonaceous and Fe-rich silicate composition; and $\lambda < 50\ \mu\text{m}$, if they have Fe-poor silicate composition).

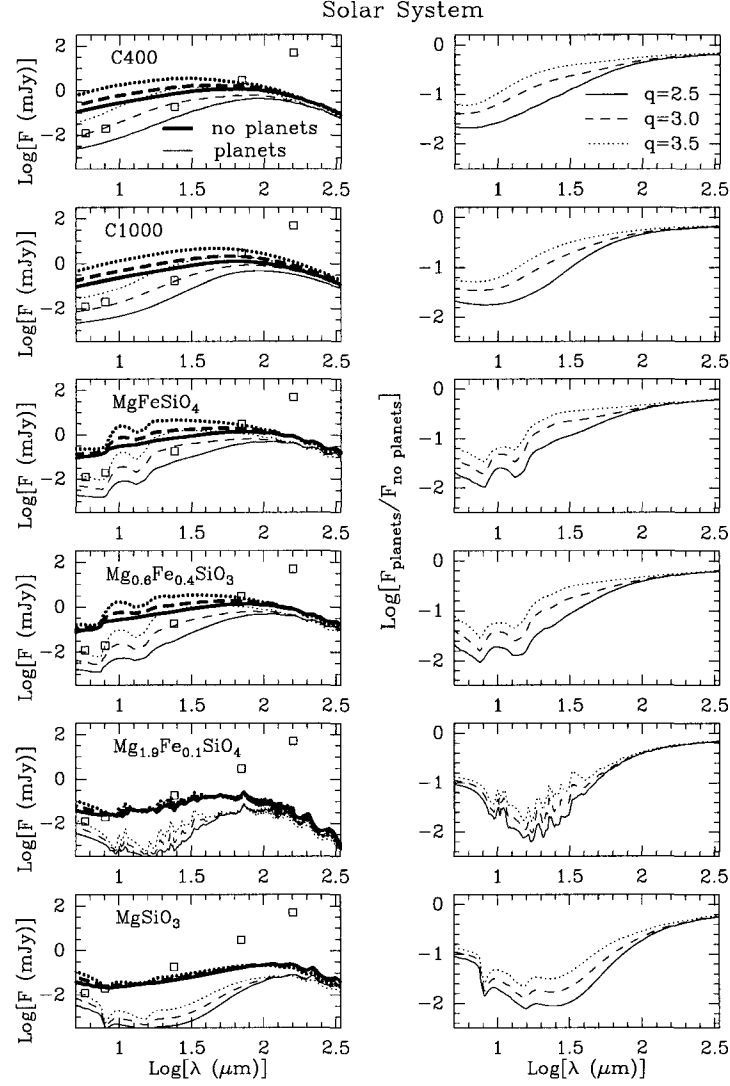


Figure 5.8: (*left*) SEDs of dust disks with and without Solar System-like planets, for six grain chemical compositions and three particle size distribution: $n(b)db = n_0 b^{-q}$, with $q=2.5$ (*solid*), 3.0 (*dashed*) and 3.5 (*dotted*). *Thick* line is for a system without planets; *thin* line is for a system with planets. In all cases the system is at a distance of 50 pc and has a total disk mass of $10^{-10}M_{\odot}$. The squares indicate *Spitzer* 5- σ detection limits. (*right*) Ratio of the composed SED arising from a system with planets to that of a system with no planets ($F_{planet}/F_{no\ planet}$). Note that in all panels the scale is logarithmic.

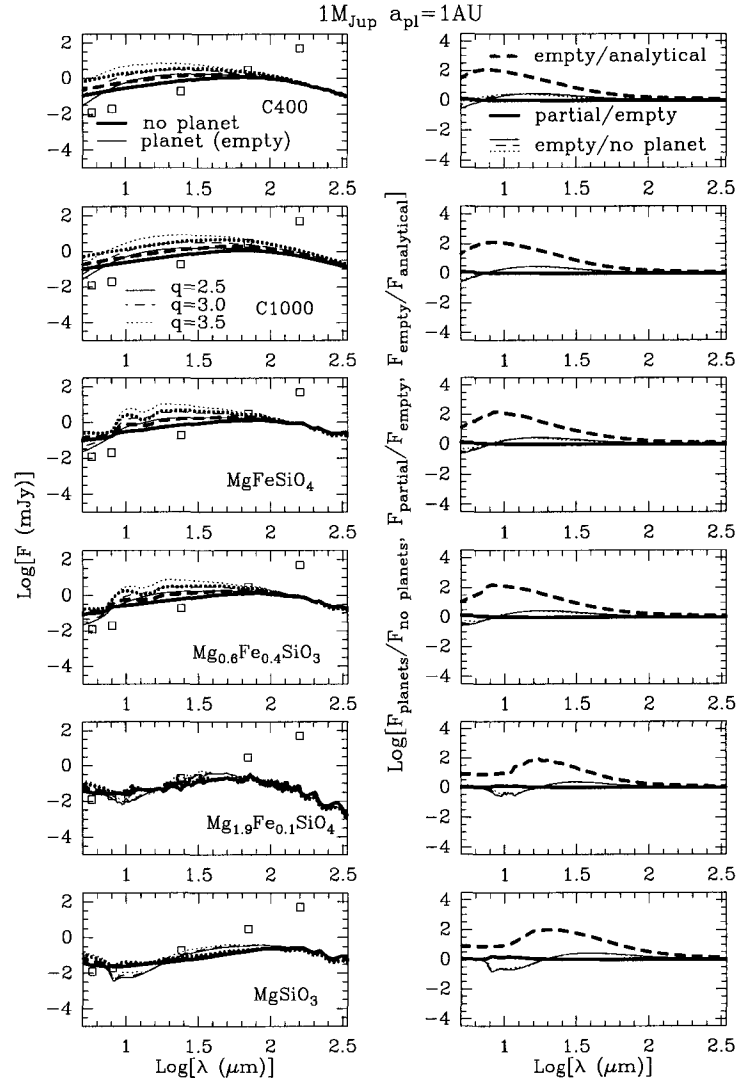


Figure 5.9: (left) Same as Figure 5.8 but with a $1M_{Jup}$ planet in a circular orbit at 1 AU. (right) The *thin* lines correspond to $F_{\text{planet}}/F_{\text{no planet}}$, and the *thick* lines to $F_{\text{partial gap}}/F_{\text{empty gap}}$ (solid) and $F_{\text{empty gap}}/F_{\text{analytical gap}}$ (dashed).

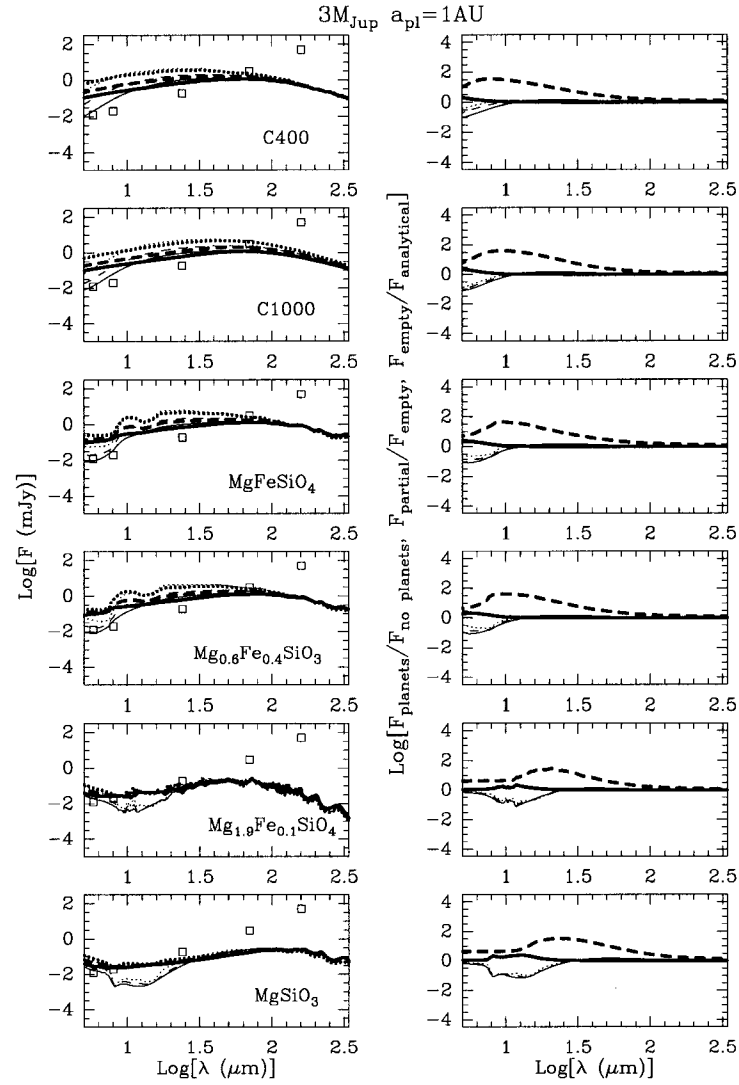


Figure 5.10: (*left*) Same as Figure 5.9 but with a $3M_{Jup}$ planet at 1 AU.

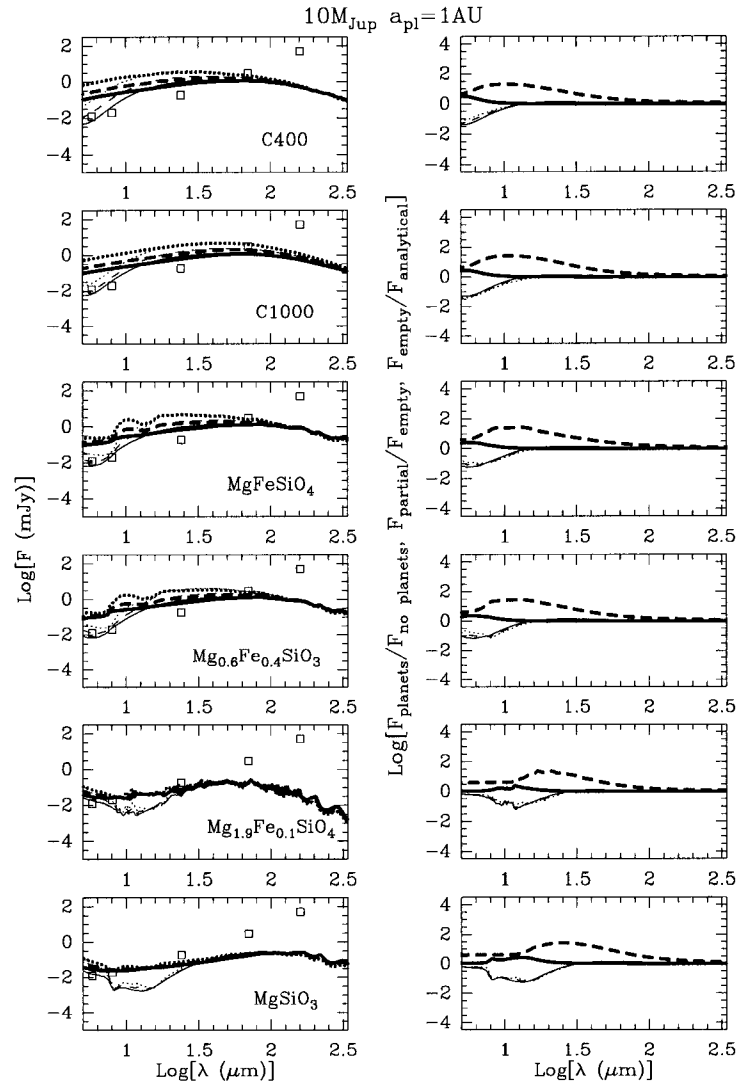


Figure 5.11: (*left*) Same as Figure 5.9 but with a $3M_{\text{Jup}}$ planet at 1 AU.

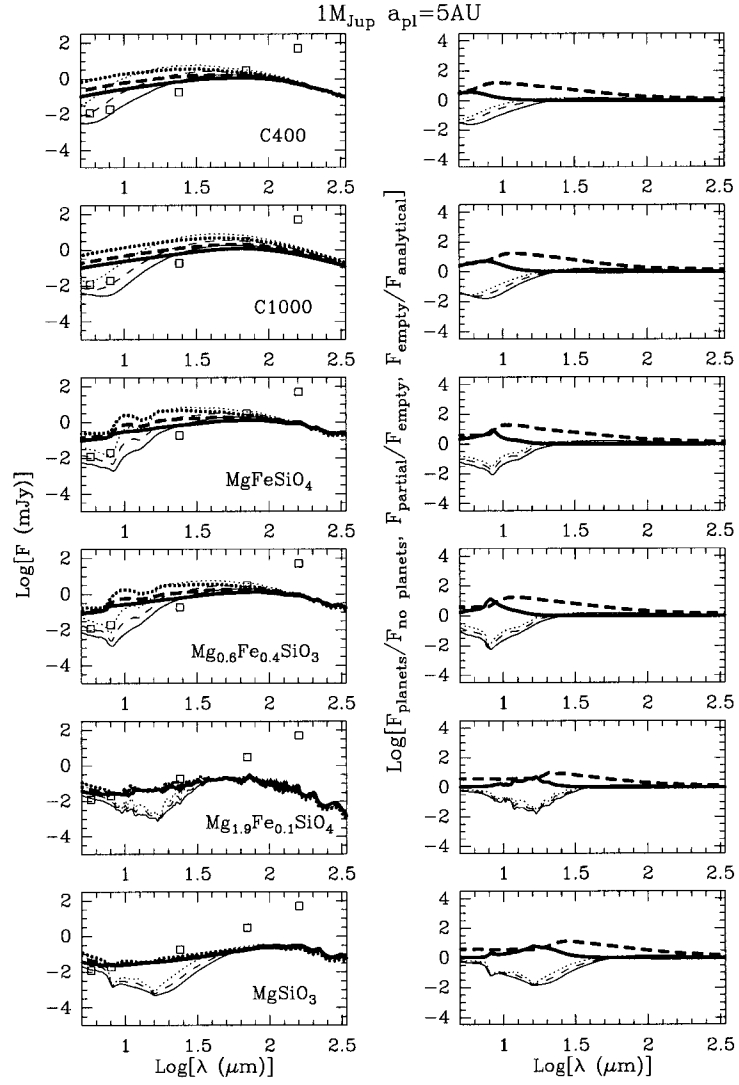


Figure 5.12: (*left*) Same as Figure 5.9 but with a $3M_{Jup}$ planet at 1 AU.

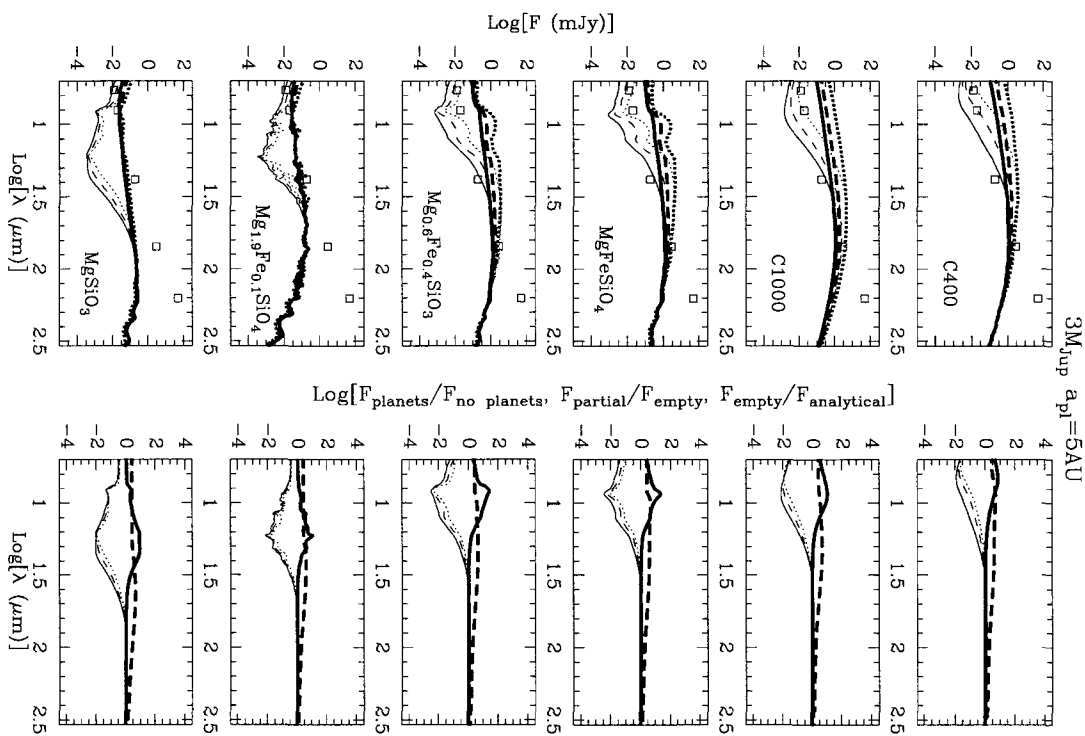


Figure 5.13: (*left*) Same as Figure 5.9 but with a $3M_{\text{Jup}}$ planet at 1 AU.

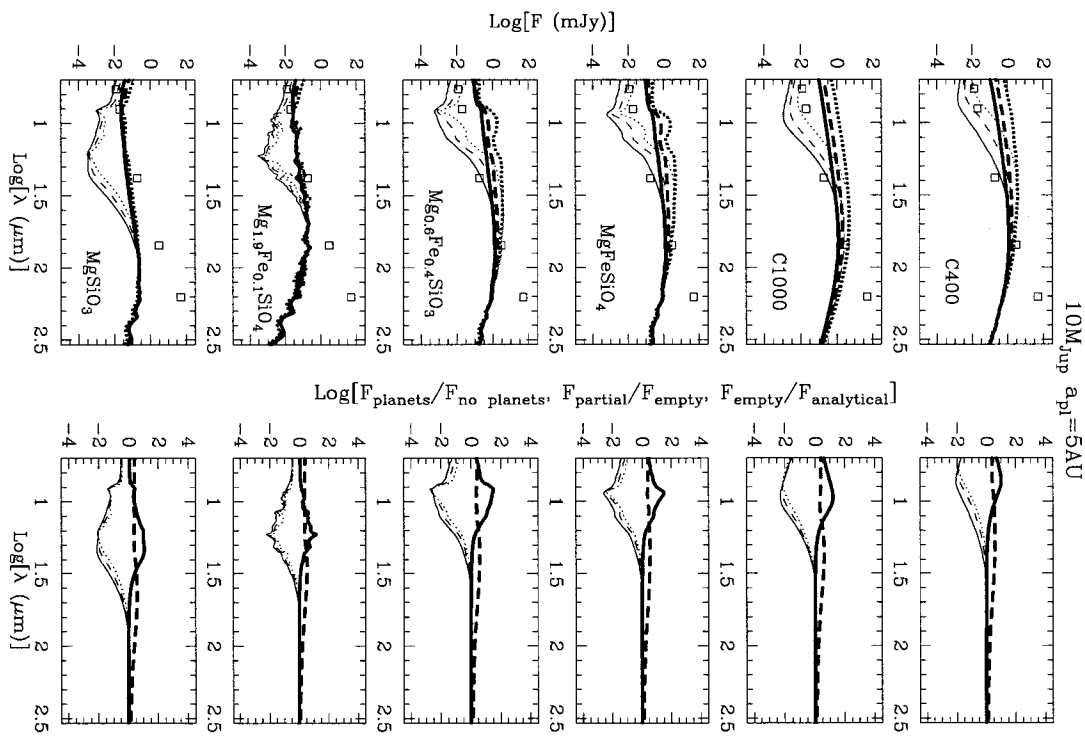


Figure 5.14: (*left*) Same as Figure 5.9 but with a $3 M_{\text{Jup}}$ planet at 1 AU.

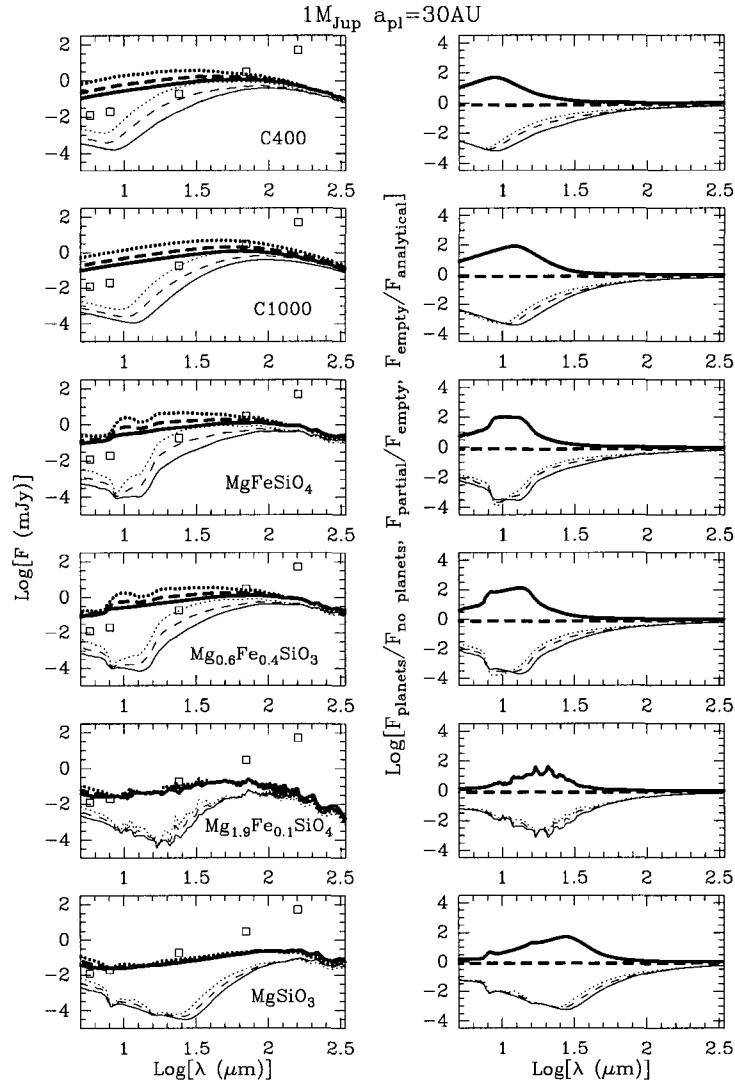


Figure 5.15: (*left*) Same as Figure 5.9 but with a $3M_{\text{Jup}}$ planet at 1 AU.

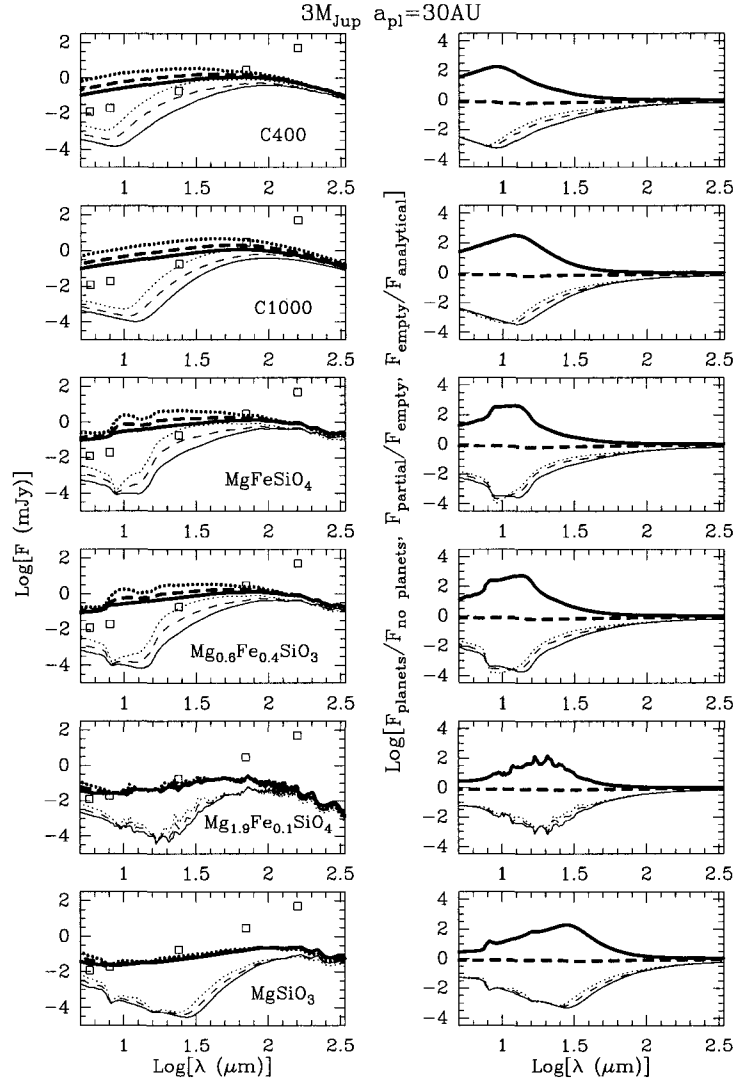


Figure 5.16: (left) Same as Figure 5.9 but with a $3M_{\text{Jup}}$ planet at 1 AU.

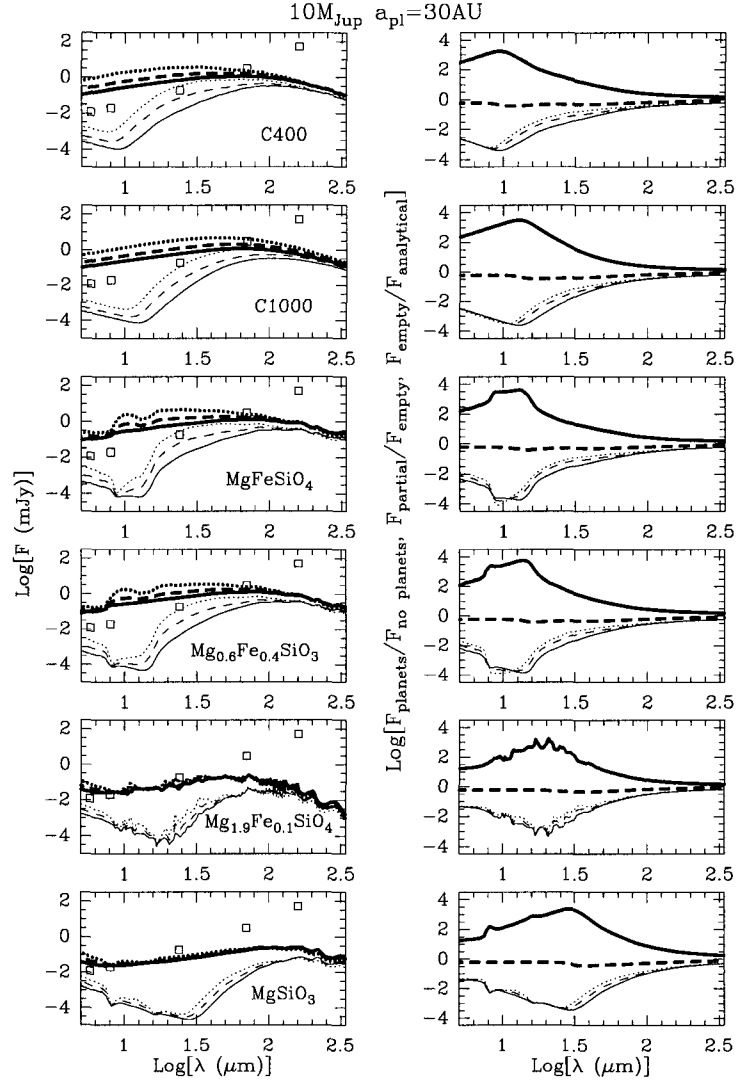


Figure 5.17: (left) Same as Figure 5.9 but with a $3M_{\text{Jup}}$ planet at 1 AU.

5.5 Predicted *Spitzer* Broadband Colors

We have calculated expected *Spitzer* broadband colors. In principle, the SEDs in Figures 5.8 to 5.17 should contain all the information given by the color-color diagrams. However, the advantage of these diagrams is that one can compare easily the results arising from many different models, allowing to explore more efficiently the parameter degeneracies in the model SEDs. In particular, we are interested in exploring the effects of planet mass and location, particle size distribution and composition, and the depletion factor inside the gap cleared by the planet.

The central bandpass wavelengths are $4.51\ \mu\text{m}$ and $7.98\ \mu\text{m}$ (IRAC), and $23.68\ \mu\text{m}$, $71.42\ \mu\text{m}$ and $155.9\ \mu\text{m}$ (MIPS)³. In addition, we have integrated the SEDs using square profiles centered at $13.2\ \mu\text{m}$ and $32.5\ \mu\text{m}$, with widths of $1.6\ \mu\text{m}$ and $5.0\ \mu\text{m}$ (for the IRS observations). These widths are chosen to avoid the bad segments of the IRS instrument and the long-wavelength tail of the $10\ \mu\text{m}$ SiO feature. Figure 5.18 shows five different combinations of color-color diagrams. Each panel corresponds to a different grain chemical composition (6 in total). The upper 6 panels are for “empty gap” models, while the lower 6 panels correspond to “partial gap” models. The q value indicated at the top of the panels is the index of the power law size distribution of the grains. We present results for $q=2.5$ and $q=3.5$. The different symbols correspond to different planetary systems.

The types of planetary systems that can be distinguishable from one another based on their *Spitzer* colors are listed in Table 5.4. The main results are the following:

1. The colors considered here can be used to diagnose the location of the planet (in the 1–30 AU range) and the absence/presence of planets.

³Spectral responses are available at http://ssc.spitzer.caltech.edu/irac/spectral_response.html and http://ssc.spitzer.caltech.edu/mips/spectral_response.html.

2. Except for one particular case, in general it is not possible to diagnose the mass of the planet (in the $1\text{--}10M_{Jup}$ range) based on these colors.
3. If the disks are composed of carbonaceous grains (C400 and C1000), the different planetary systems considered have indistinguishable *Spitzer* colors, i.e. the higher the carbonaceous content the more difficult it is to diagnose planetary systems from their colors.
4. If instead of “empty gap” models we consider “partial gap” models, where 10% of the particles drift inward, most of the planetary systems in Table 5.4 become indistinguishable from one another. It is important to keep this in mind when looking at the results in Table 5.4 involving planets at 5 or 30 AU, as in these cases our dynamical models do not contain enough particles to determine precisely how many of them drift inward (so we are subject to a $\sim 10\%$ uncertainty).
5. In some cases (see Table 5.4), two planetary systems that are distinguishable for one index of the power law for the grain size distribution, are not distinguishable when using a different index ($q=2.5$ versus $q=3.5$). This, together with the fact that different compositions yield different results (see e.g. how different are the colors for MgSiO_3 grains compared to the other compositions), complicates the analysis of the colors, as the particle size distribution and chemical composition are not known.
6. $24\mu\text{m}/32\mu\text{m}$ and $70\mu\text{m}/160\mu\text{m}$ colors are not useful to distinguish among the planetary systems considered in this study ($1\text{--}10M_{Jup}$ at $1\text{--}30\text{AU}$).

5.6 Conclusions

In anticipation of future observations of unresolved debris disks with *Spitzer*, we are interested in studying how the structure carved by planets affects the shape of

Table 5.4: List of planetary systems with distinct *Spitzer* colors. Notation: “1,5AU—30AU” means that the models with the planet at 1 or 5 AU are distinguishable from the models with the planet at 30 AU. 1Jup1 is a $1M_{Jup}$ planet at 1 AU. All results refer to “empty gap” models.

a: only valid for $q=2.5$

b: only valid for $q=3.5$

Composition	$4\mu\text{m}/8\mu\text{m}$	$8\mu\text{m}/13\mu\text{m}$	$8\mu\text{m}/24\mu\text{m}$
MgSiO ₃	1,5,30AU—no pl	1Jup1AU—1Jup30AU ^a 1Jup1AU—1Jup5AU ^a 1AU—30AU 5AU—no pl	30AU—no pl 1,5AU—30AU
Mg _{0.6} Fe _{0.4} SiO ₃	1AU—5AU ^a 1AU—30AU 5AU—no pl ^a 30AU—no pl 1Jup5—10Jup5 ^b	1,5AU, no pl—30AU ^a	
MgFeSiO ₄	1AU—30AU ^b		
Mg _{1.9} Fe _{0.1} SiO ₄ ^a		1AU—5,30AU ^a 5,30AU—no pl ^a	

Composition	13 μ m/24 μ m	24 μ m/70 μ m
MgSiO ₃	1,5AU—30AU 30AU—no pl	1Jup1—1Jup30 ^b
MgFeSiO ₄		1Jup1—1Jup30 ^b

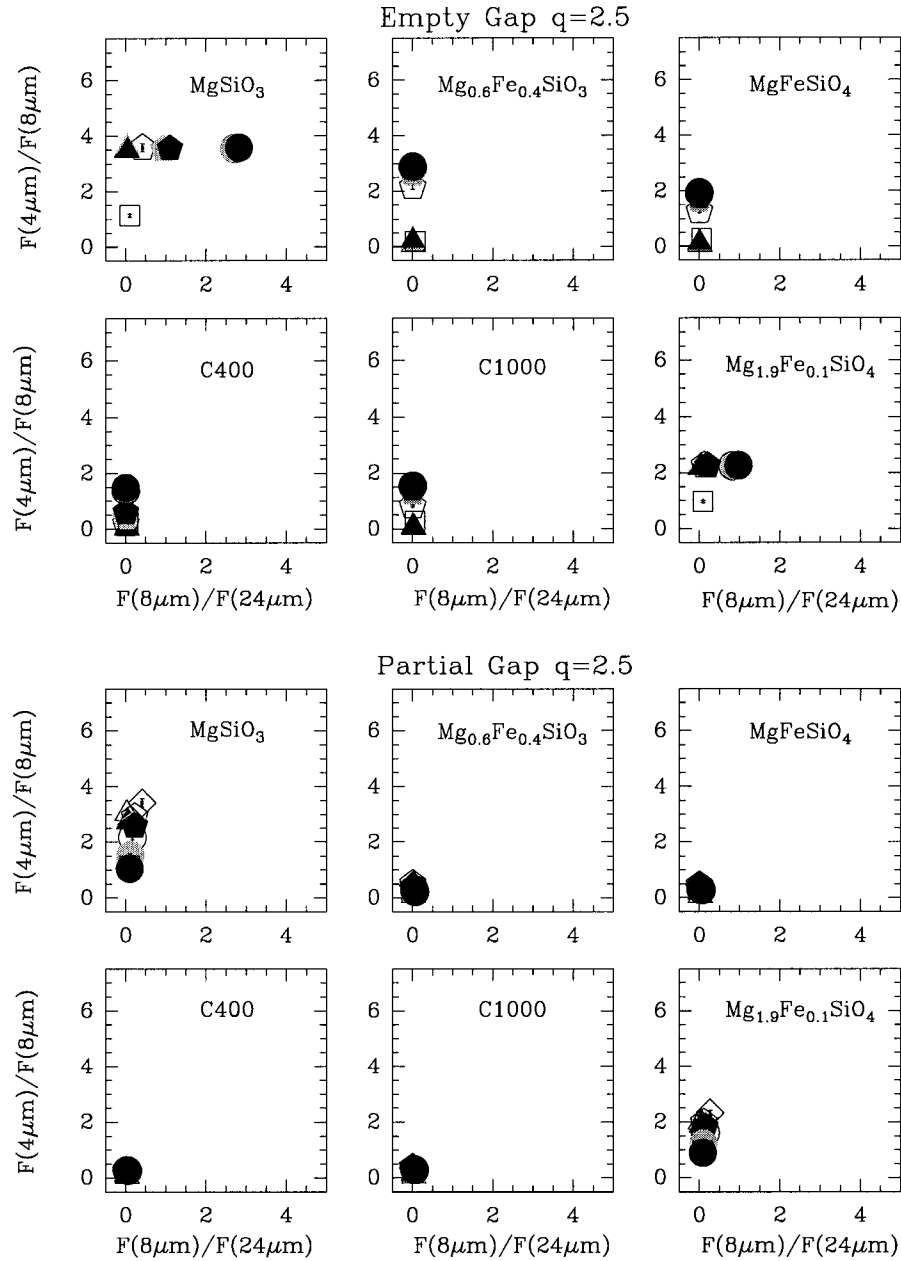
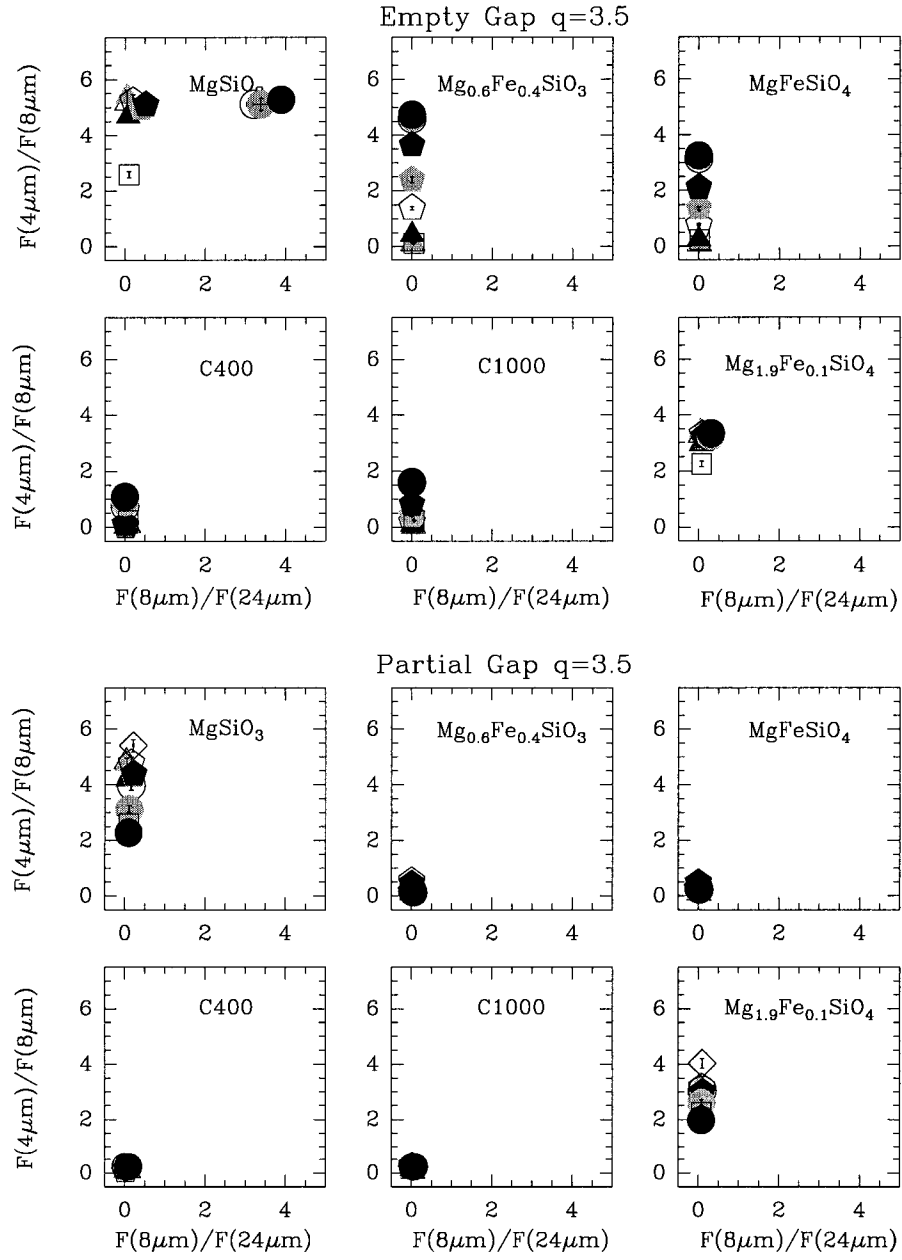
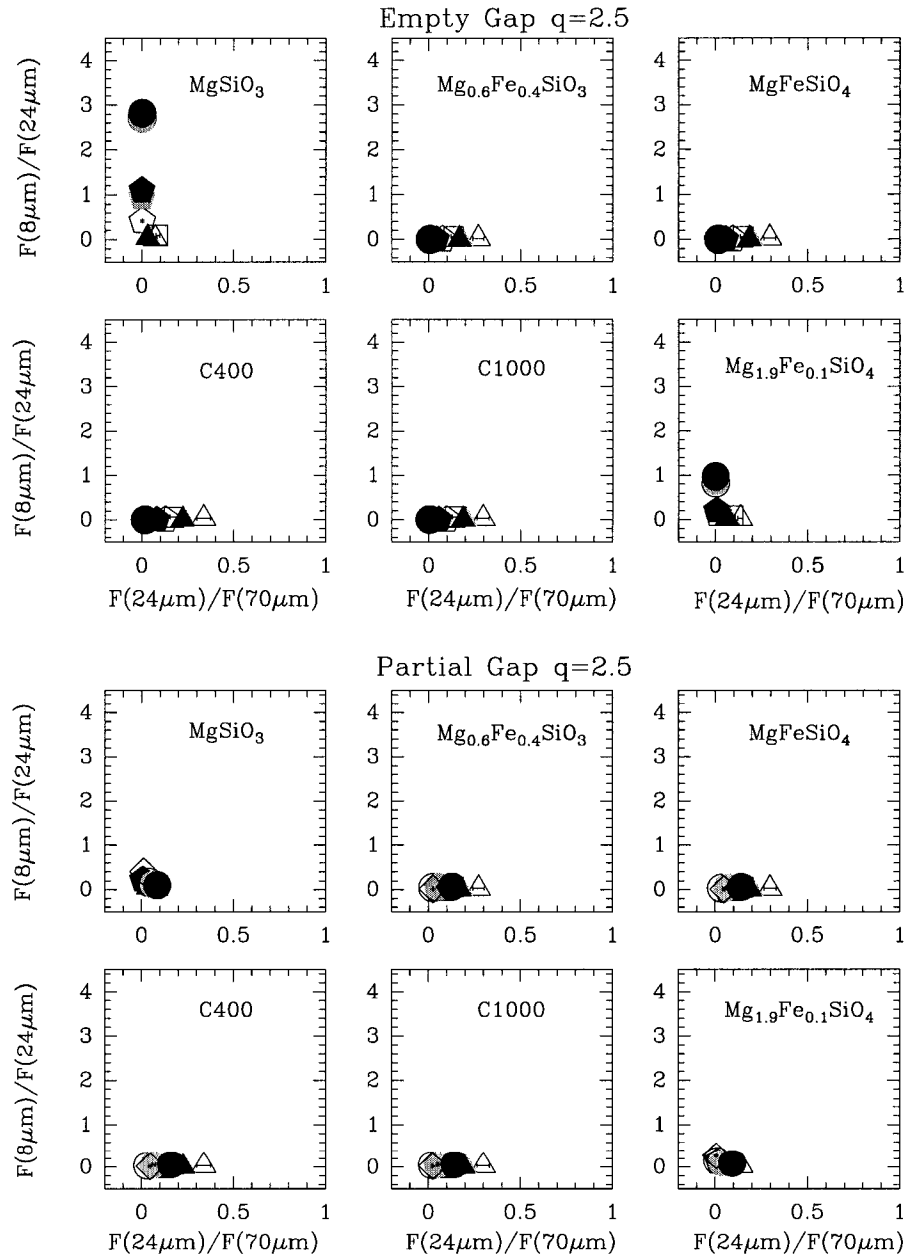
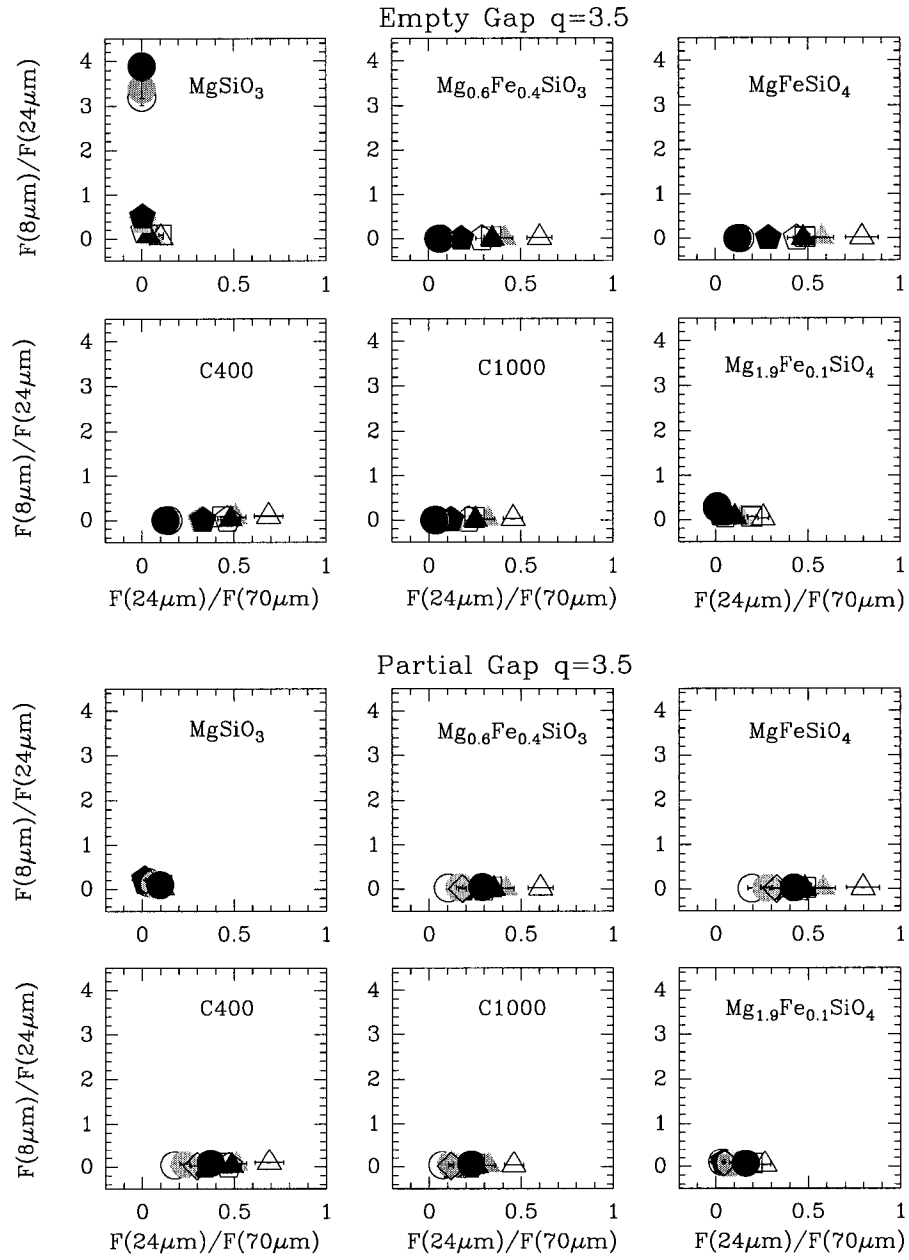
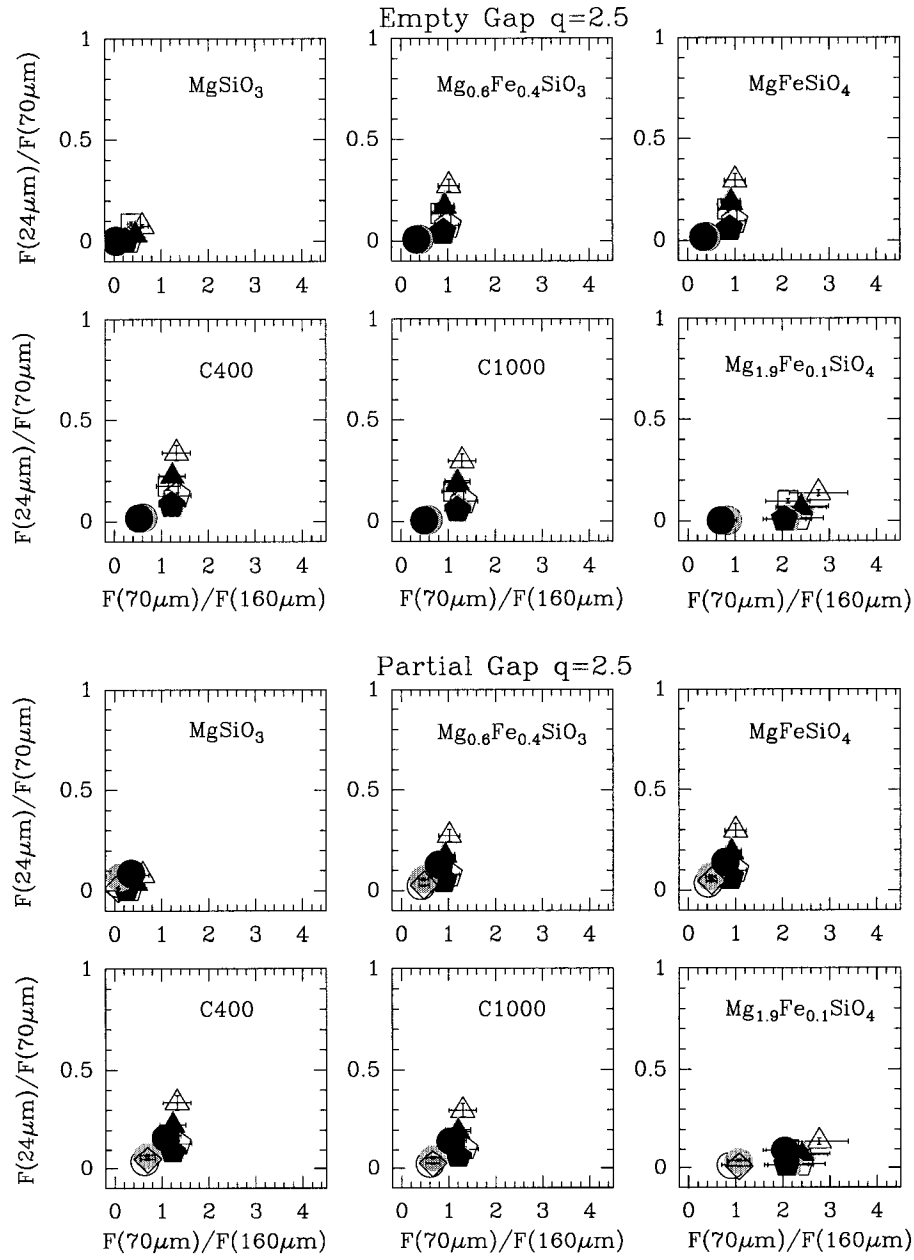


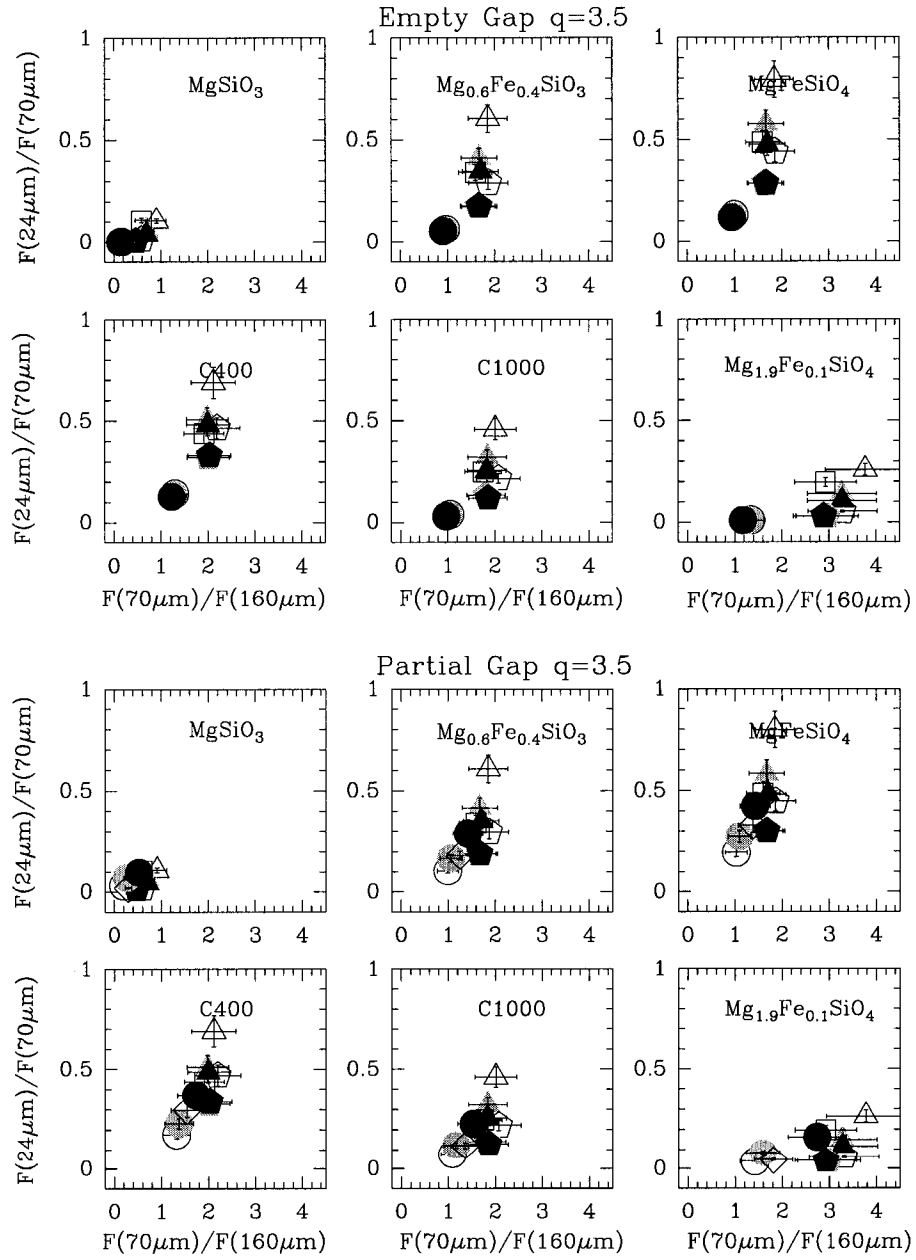
Figure 5.18: Predicted *Spitzer* broadband colors for the SEDs in Figure 5.8 to 5.17. The different symbols correspond to different planetary systems; *triangle*: models with planet at 1 AU; *pentagon*: models with planet at 5 AU; *circle*: models with planet at 30 AU; *square*: model without planets; *diamond*: Solar System models; *white*: $1M_{Jup}$ planet; *grey*: $3M_{Jup}$ planet; *black*: $10M_{Jup}$ planet. The error bars indicate (optimistic) *Spitzer* calibration uncertainties.

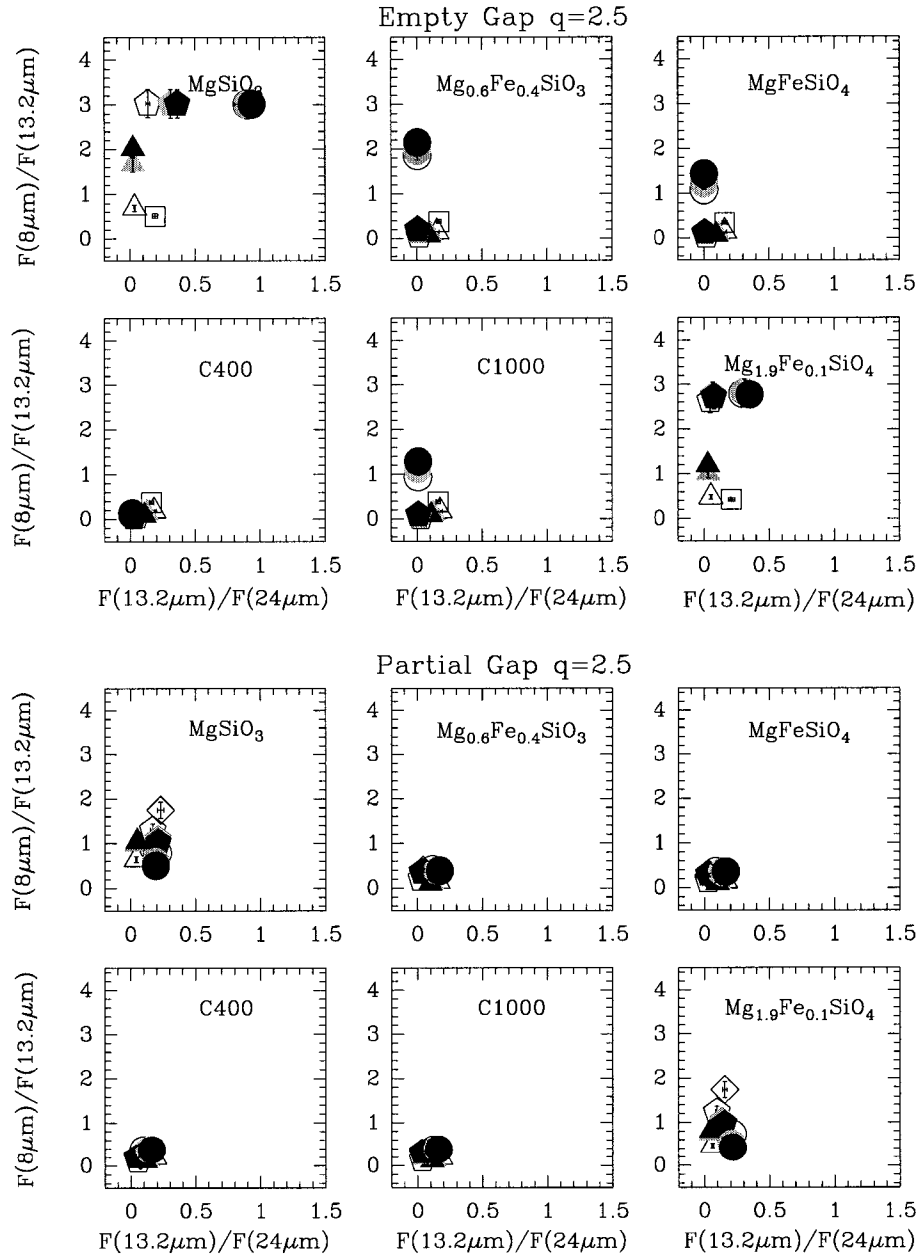


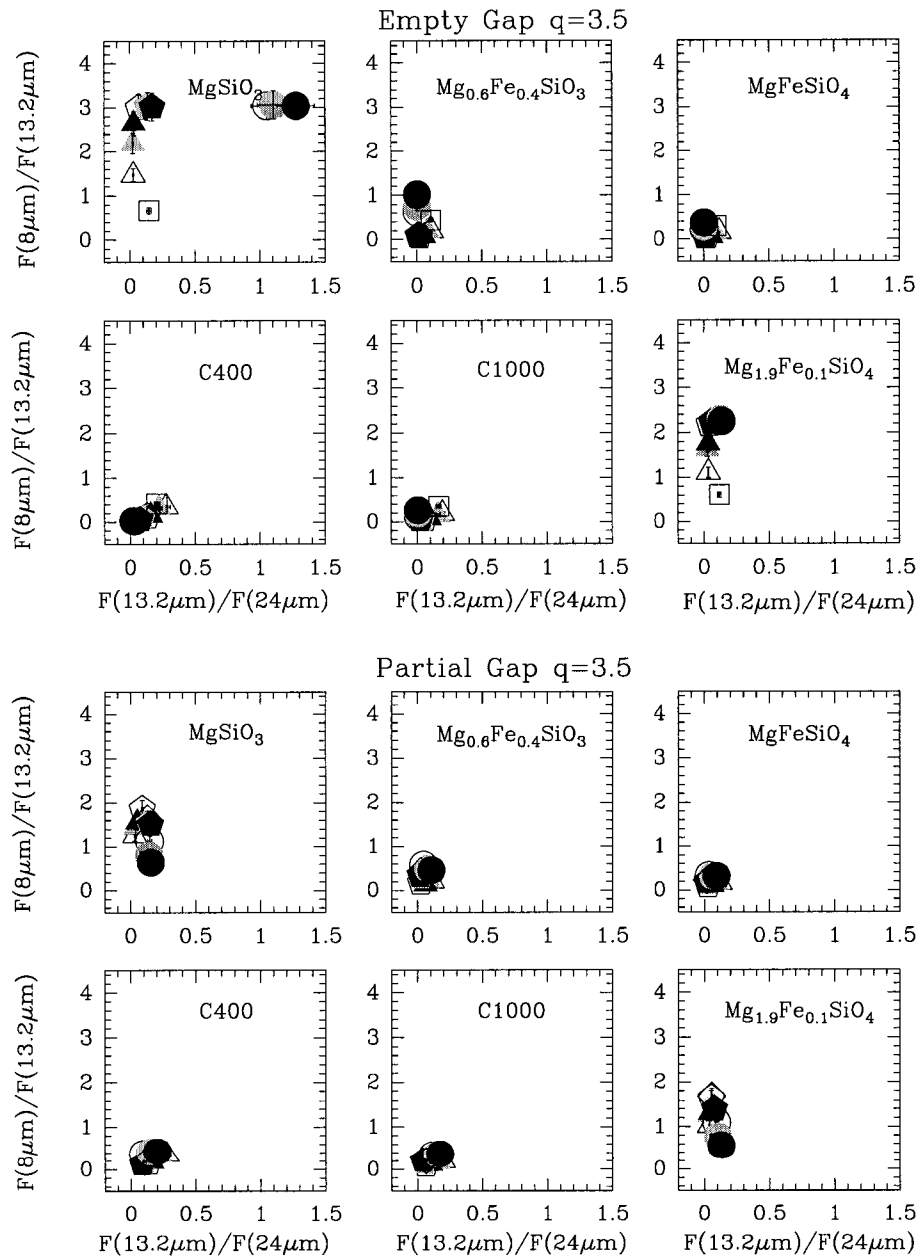


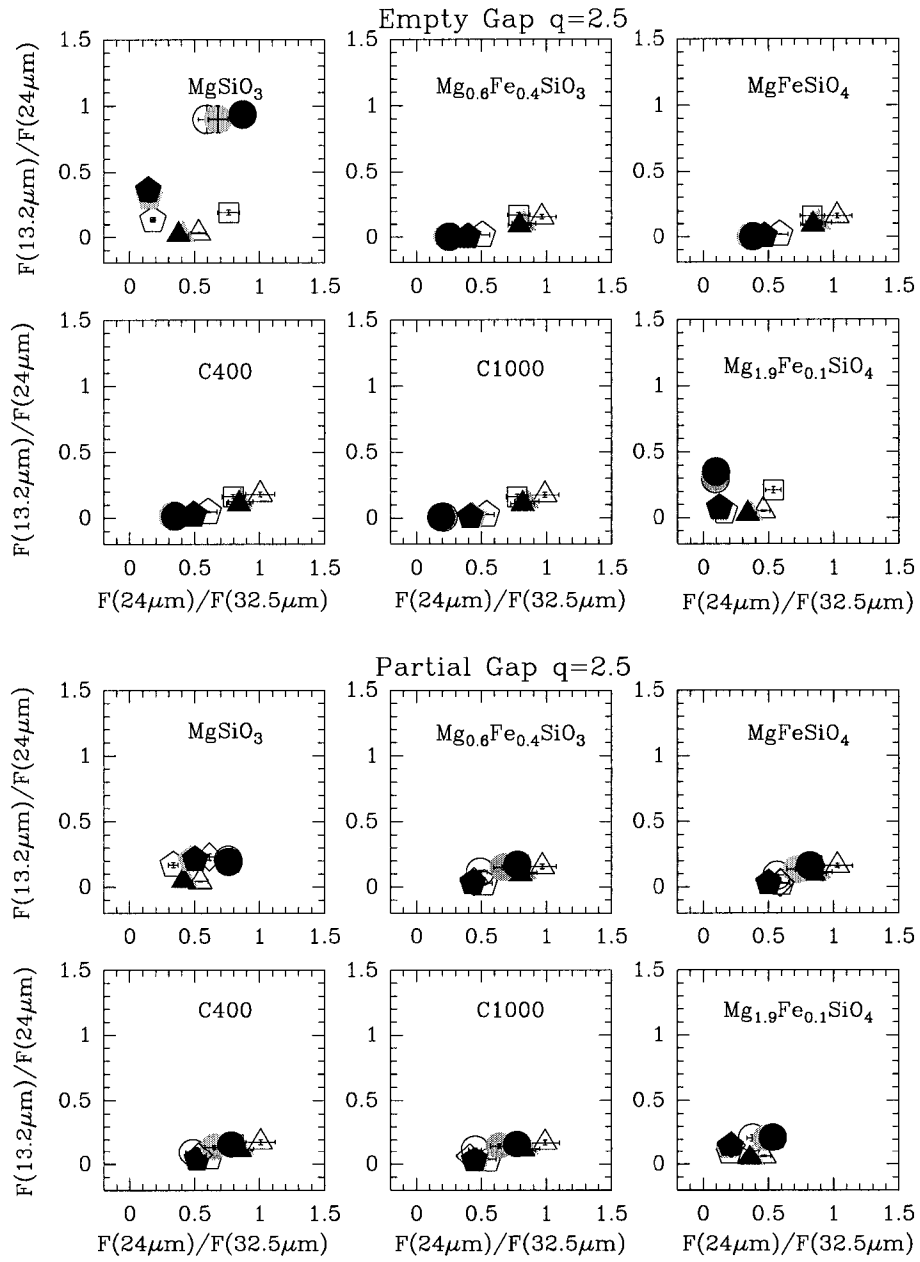


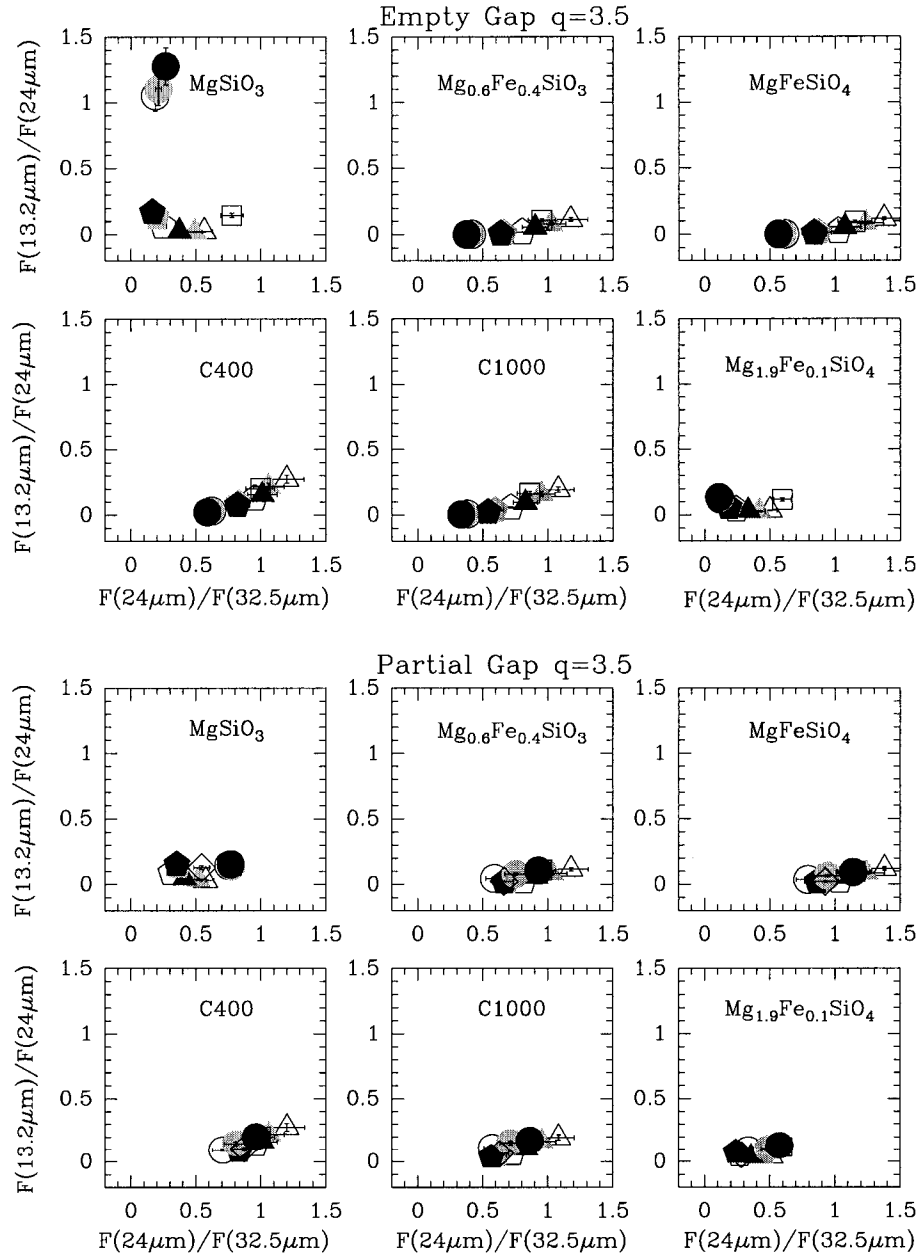












the disk’s SED, and consequently if the SED can be used to infer the presence of planets. We numerically calculate the equilibrium spatial density distributions of dust disks composed of different grain sizes, originated by a belt of planetesimals similar to the KB and in the presence of interior giant planets in different planetary configurations. A radiative transfer code is used to generate their corresponding SED for a representative sample of grain chemical compositions. The goal is to find the main parameter degeneracies in the model SEDs and the distinguishing characteristics between the SEDs of different planetary configurations.

In practice, the modeling of an observed SED is done by using simple analytical surface density distributions defined by parameters that can be varied to fit the observations. However, these parameters cannot be chosen arbitrarily, independently from the SED of the embedded star or the dust grain properties. A self-consistent combination of numerical models for the simulation of debris disk dust density distributions (that take into account the interplay between the central star SED, the grain properties and the dust dynamics), and a radiative transfer code is needed for the calculation of the dust disk SED. Our models indicate that for close-in planets (1AU), an important parameter to consider is the enhancement factor in a ring-like structure located outside the planet’s orbit, and related to the number of particles accumulated in the MMRs. Hot Jupiters can trap dust particles in MMRs at small astrocetric distances. These particles are hot and can have an important contribution to the SED. Trapping in resonances can therefore make the disk to look brighter, facilitating its detection, but it also makes a disk with an inner planet less distinguishable from a disk without planet, as the clearing of hot dust inside the planet’s orbit (and its corresponding decrease of the near-mid-IR flux) is compensated by the trapping of particles in MMRs. For planets at larger semimajor axis (5 AU and 30 AU), the important parameter to consider is the density drop interior to the planet’s orbit, related to the fraction of particles that are able to drift inward. These two parameters, describing the density enhancement

and the density drop, depend on the mass and location of the planet, and can only be estimated using dynamical simulations. We conclude that: (1) dynamical models are necessary to study the SEDs arising from debris disk systems with embedded planets of $1\text{--}10M_{Jup}$ at $1\text{--}30\text{AU}$; and (2) the number of particles in the dynamical simulations presented here ($N\sim 100$) is sufficient to study systems with planets at 1 AU, but for the study of planets at 5 AU and 30 AU we need to increase the number of particles in our simulations in order to improve the statistical uncertainty in the number of particles that drift inward to better than 10%.

The SED of the dust disk depends on the grain properties (chemical composition, density and size distribution) and the mass and location of the perturbing planet. The SED of a debris disk with interior giant planets is fundamentally different from that of a disk without planets, the former showing a significant decrease of the near/mid-IR flux due to the clearing of dust inside the planet's orbit. The SED is particularly sensitive to the location of the planet, i.e. to the area interior to the planet's orbit that is depleted in dust. However, there are some degeneracies that can complicate the interpretation of the SED in terms of planet location. For example, the SED of a dust disk dominated by Fe-poor silicate grains has its minimum at wavelengths longer than those of a disk dominated by carbonaceous and Fe-rich silicate grains. Because the SED minimum also shifts to longer wavelengths when the gap radius increases (owing to a decrease in the mean temperature of the disk), we note that there might be a degeneracy between the dust grain chemical composition and the semimajor axis of the planet clearing the gap. For an example, notice the similarities in the shape of the SEDs arising from a dust disk with a $3 M_{Jup}$ planet at 1 AU and dominated by MgSiO_3 grains, and a disk with a $3 M_{Jup}$ planet at 30 AU and dominated by MgFeSiO_4 grains (see Figure 5.19). This illustrates the importance of obtaining spectroscopy observations able to constrain the grain chemical composition.

We saw that for planets at 5 and 30 AU, the difference in the SED arising

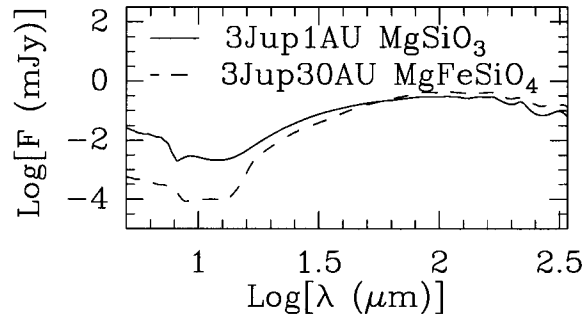


Figure 5.19: Possible degeneracy between the grain chemical composition and the location of the planet clearing the gap. *Solid line*: SED of dust disk composed of MgSiO_3 grains with a $3M_{Jup}$ planet at 1 AU; *dashed line*: same for MgFeSiO_4 grains with a $3M_{Jup}$ planet at 30 AU. In both cases $q=2.5$.

from a disk with an empty gap interior to the planet’s orbit, and a disk with an inner hole that is 90% depleted, is large. This means that the SED is very sensitive to the depletion factor inside the gap. Because this depletion factor depends largely on the planet mass, in principle one should be able to use SEDs to diagnose masses of planets at large astrometric distances. To do that we would need to increase the number of particles in our dynamical simulations. Based on the depletion factors obtained from our models, we expect that the planetary masses that one would be able to study with this method would range from $>1M_{Nep}$ to $3M_{Jup}$. Anything larger than $3M_{Jup}$ would create an almost empty gap, being indistinguishable from one another. A $1M_{Nep}$ planet at 30 AU ejects $<10\%$ of the particles, so the effect of a less massive planet would probably be difficult to detect. At 1 AU, the SED of the disk seems to be more insensitive to the depletion factor (because as mentioned above, its effect on the SED is balanced by the particles in the MMRs). This means that it would be difficult to diagnose the mass of a close-in planet based on the SED of the dust disk.

The gaps and azimuthal asymmetries observed in high resolution images of debris disks suggest that giant planets may be present in these systems. Because debris disk structure is sensitive to a wide range of planet semimajor axis, complementing a parameter space not covered by radial velocity and transit surveys (sensitive only to close-in planets), the study of the disk structure can help us learn about the diversity of planetary systems. Even when spatially resolved images of the disk are not available, we have seen that its SED may contain the signatures of the underlying planets. The SED can therefore be a valuable tool for detecting and even constraining the mass and location of the planet.

CHAPTER 6

Future Work

In the near future I would like to generate a grid of models to explore, over a wide range of planetary architectures, how planets affect the structure and evolution of debris disks. For each planetary system in the grid I will calculate: (1) scattered light and thermal emission images that will be useful to map the debris disk structure observed by high-sensitivity and high-spatial resolution telescopes (like *HST*, *KeckIF*, *LBT*, *JWST*, *SOFIA* and *ALMA*) to the parameters of the unseen planetary perturbers; (2) SEDs that will be useful in identifying the signatures of planets in the SEDs of unresolved debris disks soon to be observed by *Spitzer*. I also plan to carry out detailed calculations for particular cases where the disk is observed and is spatially resolved, and whose SED indicates that planets may be present. This will allow me to compare the information derived from the SED alone to that derived from the resolved image, important for understanding the limitations of the characterization of planetary architectures based on unresolved debris disks only. Finally, I will study the dynamics of dust in younger disks (10-100 Myr), estimating how much gas a disk needs to have in order to destroy the structure created by the planets.

6.1 Study of Debris Disk Structure over a Wide Range of Planetary Architectures.

I propose to create a grid of models to carry out a more exhaustive and unbiased study on how the presence of giant planets, over a wide range of planetary architectures, affects the structure and evolution of debris disks. By exploring the parameter space, I will be able to discern how the spatial structure and particle size distribution of the dust particles depend on the orbital parameters and dust production rates of the planetesimals, and the orbital parameters and masses of the perturbing planetary bodies. A self-consistent approach will involve the following steps:

- *Select a representative set of planetary architectures* (determined by the orbital elements and masses of the planet/s, and orbital elements of the dust-producing planetesimals). We will start with single planet systems, with semi major axis in the range 1–30 AU, eccentricities 0–0.7, and planet masses 0.1–10 M_{Jup} . For each of these cases, three types of planetesimals will be considered: inner and outer belts, analogous to the asteroid and Kuiper belts in our Solar System, and a “trojan” population in 1:1 resonance with the planet. [It is estimated that in the Solar System the total mass in the trojan asteroids may be similar to the mass in the rest of the asteroid population]. The inner and outer edges of the belts will be determined using dynamical analytical considerations and numerical models to ensure that the planetesimals are on stable orbits. Their distribution of eccentricities and inclinations will be chosen to take into account the mutual gravitational interaction of the swarm of planetesimals, and the gravitational perturbation by the planet.
- *Derive the steady state spatial distribution of dust for a wide range of particle sizes.* Using the same approach as in the previous chapters I will follow numerically the evolution of several hundred of dust particles originating in the

planetesimal populations defined above, under the combined effects of stellar gravity, stellar radiation pressure, Poynting-Robertson (P-R) and stellar wind drag, and the gravitational forces of the planet/s. This will allow me to derive the steady-state distribution of dust grains of different particle sizes.

- *Normalization to “true” dust production rates.* The number density distributions derived above for each particle size and planetary architecture need to be scaled using realistic dust production rates. We will produce dust production rates as a function of distance from the central star, that are consistent with the dynamics of the planetary system under consideration (i.e. the distribution of eccentricities and inclinations of the planetesimals and the mass and orbital parameters of the planet).
- *From dust spatial distribution to scattered light and thermal emission images.* For each planetary architecture, I will combine different particle sizes to produce scattered light and thermal emission images. Of particular interest are the longer wavelengths, where observations can constrain the amount of material further away from planet, and where the emission of the larger dust particles, the ones that show more prominent structure, dominate. These modeled images will be useful to map the debris disk structure observed by high-sensitivity and high-spatial resolution telescopes like *HST*, *KeckIF*, *LBT*, *JWST*, *SOFIA* and *ALMA*, to the parameters of the unseen planetary perturbers.

6.2 SEDs: Looking for Planets in Spatially Unresolved Debris Disks.

Preliminary studies, like the ones shown in Chapter 5, show that, for a representative sample of grain compositions, the SED of a dust disk with embedded planets is fundamentally different from that of a disk without planets, the former showing a significant decrease of the mid IR flux due to the clearing on dust inside the

planet's orbit by gravitational scattering with the planet. In anticipation of future observations of unresolved debris disks with *Spitzer*, we are interested in studying how the structure carved by the planets affects the shape of the disk's SED, and consequently if the SED can be used to infer the presence of planets. The radial distribution of dust derived for each planetary architecture and particle size in the grid, will be used as input for a detailed radiative transfer code that takes into account scattering, absorption and reemission of the stellar radiation by the dust grains. The resulting SEDs will be combined to allow for a distribution of grain sizes and compositions. These SEDs will serve as templates to which one can compare the dust distributions derived from the *Spitzer* observations for their interpretation in terms of planetary architectures. This grid of SEDs will help us: (1) investigate how the presence of planets affects the debris disk's SEDs by comparing systems with planets and without planets; (2) determine what information could be derived from an observed SED in terms of planetary and planetesimal orbital elements, dust composition and particle size distribution; and (3) evaluate the degeneracy of the problem by determining what types of systems yield distinguishable SEDs, as it is expected that in some cases different planetary architectures will result in similar SEDs.

6.3 Detailed Modeling of Individual Spatially Resolved Disks.

By comparison with the grid of images and SEDs, observers will be able to discern quickly whether or not massive planets may be present in their data, giving a range of possible parameters. But a unique dynamical calculation for each particular case will be needed to get precise estimates of the planet mass and orbit. I plan to carry out these detailed calculations for few particular cases where: (1) the disk is observed by *Spitzer* and its SED indicates that giant planets may be present; and (2) the disk is observed and is spatially resolved (with e.g. *HST* or LBT in scattered

light and/or thermal emission at (sub)millimeter wavelengths). The modeling of these observations will allow me to: (1) compare the information derived from the SED alone to that derived from the resolved image, important for understanding the limitations of the characterization of planetary architectures based on unresolved debris disks only; and (2) break the degeneracy expected from the analysis of the disk SED by obtaining resolved images in one or more wavelength.

6.4 Intermediate Age Disks: Effect of Gas Drag.

The models described above are focused on the study of mature debris disk systems, where most of the mass is locked in planets that are in stable orbits and therefore are not themselves a source of dust by collisions. In these systems, gas drag and mutual grain collisions do not play an important role in the dynamical evolution and consequently the spatial distribution of dust particles. However, intermediate-age systems (10-100 Myrs) are very interesting because the mass is not excessively concentrated in large bodies, implying that lots of collisional activity could be present in an epoch where terrestrial planet formation may be taking place. These middle-aged disks have gone undetected so far, but it is expected that *Spitzer*, with its unprecedented sensitivity, will be able to observe them. I plan to study the dynamics of dust particles in these disks, where gas drag and mutual grain collisions play an important role in the shaping of the disk's structure. It is estimated that when only 1% of the primordial nebula is left, grains of size 1 cm or less are affected by gas drag. If the gas content decreases by another four orders of magnitude, grains of 1 μm size or smaller are still affected. Detailed modeling of these disks would require dealing with gas hydrodynamics and dust dynamics simultaneously. A much simpler approach in which we do not follow the gas, would be to introduce its effect by means of a drag parameter that depends on the gas density. Using this approach I will estimate how much gas a disk needs to have in order to destroy the structure

created by massive planets. This will be important for interpreting correctly the SEDs of unresolved debris disks which show signatures of a massive planet (e.g. by a significant decrease of the mid IR flux) but for which H_2 lines are also present. One needs to keep in mind, however, that the modeling of these systems may be very complex, as collisional dust-production events may be stochastic, so a steady-state approach (as the one taken for mature systems) is not appropriate. Furthermore, the SED of such disks may depend strongly on where the dust production is taking place, and not so much on where the large perturbing bodies are.

REFERENCES

- Allen, R. L., G. M. Bernstein, and R. Malhotra (2001). The Edge of the Solar System. *ApJL* **549**, 241.
- Altobelli, N., S. Kempf, R. Srama, E. Grun, M. Stubig, and M. Landgraf (2003). Dust measurements at 1 AU with Cassini-CDA. *Astrophysics of Dust, Estes Park, Colorado (eds A.N. Witt)*, .
- Aumann, H., C. Beichman, F. Gillett, T. de Jong, J. Houck, F. Low, G. Neugebauer, R. Walker, and P. Wesselius (1984). Discovery of a shell around Alpha Lyrae. *ApJL* **278**, 23.
- Backman, D. (2002). Personal communication. , .
- Backman, D. (2003). Personal communication. , .
- Backman, D., A. Dasgupta, and R. Stencel (1995). Model of a Kuiper Belt Small Grain Population and Resulting Far-Infrared Emission. *ApJL* **450**, 35.
- Backman, D. and F. Paresce (1993). Main-sequence stars with circumstellar solid material - The VEGA phenomenon. *Protostars and Planets III (ed. E.H. Levy & J.I. Lunine, Tucson: Univ. of Arizona Press)*, 1253–1304.
- Baggaley, W. (2000). Advanced Meteor Orbit Radar observations of interstellar meteoroids. *J.Geophys.Res.* **105**, 10353.
- Balogh, A. (1996). The Heliospheric Magnetic Field. *Space Sci. Rev.* **78**, 15.
- Briggs, R. (1962). Symposium: Astrometry I: The steady-state space distribution of meteoric particles under the operation of the Poynting-Robertson Effect. *AJ* **67**, 710.
- Brown, M. (2001). The Inclination Distribution of the Kuiper Belt. *AJ* **121**, 2804–2814.
- Brownlee, D., D. Joswiak, and S. Love (1994). Identification and Analysis of Cometary IDPs. *LPI* **25**, 185.
- Burns, J., P. Lamy, and S. Soter (1979). Radiation forces on small particles in the solar system. *Icarus* **40**, 1.
- Chiang, E. I. and M. E. Brown (1999). Keck Pencil-Beam Survey for Faint Kuiper Belt Objects. *AJ* **118**, 1411.

- Consolmagno, G. (1979). Lorentz scattering of inte. *Icarus* **38**, 398.
- Dent, W., H. Walker, W. Holland, and J. Greaves (2000). Models of the dust structures around Vega-excess stars. *MNRAS* **314**, 702.
- Dermott, S., D. Durda, B. Gustafson, S. Jayaraman, J.-C. Liou, and Y. Xu (1994). Modern sources of dust in the solar system. *IAU Symp. 160, Asteroids, Comets and Meteors* (ed. A. Milani, M. di Martino, & A. Cellino; Dordrecht: Kluwer), 127.
- Dermott, S., D. Durda, B. Gustafson, S. Jayaraman, Y. Xu, R. Gomes, and P. Nicholson (1992). . *Asteroids, Comets and Meteors 1991*, 153.
- Dohnanyi, J. (1969). Collisional models of asteroids and their debris. *J. Geophys. Res.* **74**, 2531.
- Dorschner, J., B. Begemann, T. Henning, C. Jäger, and H. Mutschke (1995). Steps toward interstellar silicate mineralogy. II. Study of Mg-Fe-silicate glasses of variable composition. *Astron. Astrophys.* **300**, 503.
- Duncan, M., H. Levison, and M. Lee (1998). A Multiple Time Step Symplectic Algorithm for Integrating Close Encounters. *AJ* **116**, 2067.
- Fahr, H.-J., K. Scherer, and M. Banaszkiewicz (1995). The evolution of the zodiacal dust cloud under plasma drag and Lorentz forces in the latitudinally asymmetric solar wind. *Planet. Space Sci.* **43**, 301.
- Flavill, R., W. Carey, J. McDonnell, D. Ashworth, and R. Allison (1980). Progress in defining the solar wind sputter rate on protoplanets and interplanetary matter. *Planet. Space Sci.* **28**, 511.
- Flynn, G. (1995). Interplanetary Dust - Changes in the Zodiacal Cloud. *Nature* **376**, 114.
- Frisch, P., J. Dorschner, J. Geiss, J. Greenberg, E. Grun, M. Landgraf, P. Hoppe, A. Jones, W. Katschmer, T. Linde, G. Morfill, W. Reach, J. Slavin, J. Svestka, A. Witt, and G. Zank (1999). Dust in the Local Interstellar Wind. *ApJ* **525**, 492.
- Gorlova et al., N. (2004). New debris disks candidates: 24 micron excess at 100 Myr, in preparation. pp. .
- Greaves, J., W. Holland, R. Jayawardhana, M. Wyatt, and W. Dent (2004). A search for debris disks around stars with giant planets. *Mon.Not.R.Astron.Soc.* **348**, 1097.
- Greaves, J., W. S. Holland, G. Moriarty-Schieven, and T. Jenness (1998). A Dust Ring around epsilon Eridani: Analog to the Young Solar System. *ApJ* **506**, 133.

- Greaves, J., V. Mannings, and W. Holland (2000). The Dust and Gas Content of a Disk around the Young Star HR 4796A. *Icarus* **143**, 155.
- Greaves, J. and M. Wyatt (2003). Some anomalies in the occurrence of debris discs around main-sequence A and G stars. *Mon.Not.R.Astron.Soc.* **345**, 1212.
- Grun, E., B. Gustafson, I. Mann, M. Baguhl, G. Morfill, P. Staubach, A. Taylor, and H. Zook (1994). Interstellar dust in the heliosphere. *Astron. Astrophys.* **286**, 915.
- Grun, E. and J. Svestka (1996). Physics of Interplanetary and Interstellar Dust. *Space Sci. Rev.* **78**, 347.
- Grun, E., H. Zook, M. Baguhl, A. Balogh, S. Bame, H. Fechtig, R. Forsyth, M. Hanner, M. Horanyi, J. Kissel, B. Lindblad, D. Linkert, G. Linkert, I. Mann, J. McDonnell, G. Morfill, J. Phillips, C. Polanskey, G. Schwehm, N. Siddique, P. Staubach, J. Svestka, and A. Taylor (1993). Discovery of Jovian dust streams and interstellar grains by the ULYSSES spacecraft. *Nature* **362**, 428.
- Grun, E., H. Zook, H. Fechtig, and R. H. Giese (1985). Collisional balance of the meteoritic complex. *Icarus* **62**, 244.
- Gurnett, D., J. Ansher, W. Kurth, and L. Granroth (1997). Micron-sized dust particles detected in the outer solar system by Voyager 1 and 2 plasma wave instruments. *Geophys. Res. Lett.* **24**, 3125.
- Gustafson, B. (1994). Physics of zodiacal cloud. *Annu. Rev. Earth Planet Sci.* **22**, 553.
- Habing, H., C. Dominik, M. Jourdain de Muizon, R. Laureijs, M. Kessler, K. Leech, L. Metcalfe, A. Salama, R. Siebenmorgen, N. Trams, and P. Bouchet (2001). Incidence and survival of remnant disks around main-sequence stars. *A&A* **365**, 545.
- Hartmann, L. (2000). *Accretion Processes in Star Formation*, Cambridge University Press. , .
- Holland, W., J. Greaves, W. Dent, M. Wyatt, B. Zuckerman, R. Webb, C. McCarthy, I. Coulson, E. Robson, and W. Gear (2003). Submillimeter Observations of an Asymmetric Dust Disk around Fomalhaut. *ApJ* **582**, 1141.
- Jäger, C., H. Mutschke, and T. Henning (1998). Optical properties of carbonaceous dust analogues. *Astron. Astrophys.* **332**, 291.
- Jewitt, D. and J. Luu (1995). The solar system beyond Neptune. *AJ* **109**, 1867.
- Jewitt, D. and J. Luu (2000). . *Protostars and Planets IV (eds Mannings, V., Boss, A.P., Russell, S. S., Tucson: Univ. of Arizona Press)*, 1201.

- Johnson, R. (1990). . *Energetic Charged Particle Interaction with Atmospheres and Surfaces* (Berlin: Springer Verlag), .
- Johnson, R. and R. Baragiola (1991). Lunar surface - Sputtering and secondary ion mass spectrometry . *Geophys. Res. Lett.* **18**, 2169.
- Johnson, R. and L. Lanzerotti (1986). Ion bombardment of interplanetary dust. *Icarus* **66**, 619.
- Jokipii, J. and P. Coleman (1968). . *J.Geophys.Res.* **73**, 5495.
- Joswiak, D., D. Brownlee, R. Pepin, and D. Schlutter (2000). Characteristics of Asteroidal and Cometary IDPs Obtained from Stratospheric Collectors: Summary of Measured He Release Temperatures, Velocities and Descriptive Mineralogy. *LPI* **31**, 1500.
- Kalas, P. and D. Jewitt (1995). Asymmetries in the Beta Pictoris Dust Dis. *AJ* **110**, 794.
- Kerridge, J. F. (1991). A reevaluation of the solar-wind sputtering rate on the lunar surface. *Lunar and Planetary Science XXI (Houston: Lunar Planet. Inst.)*, 301.
- Kessler, D. J. (1981). Derivation of the collision probability between orbiting objects The lifetimes of Jupiter's outer moons. *Icarus* **48**, 39.
- Knacke, R., S. Fajardo-Acosta, C. Telesco, J. Hackwell, D. Lynch, and R. Russell (1993). The Silicates in the Disk of beta Pictoris. *ApJ* **418**, 440.
- Kortenkamp, S. and S. Dermott (1998). Accretion of Interplanetary Dust Particles by the Earth. *Icarus* **135**, 469.
- Kuchner, M. and M. Holman (2003). The Geometry of Resonant Signatures in Debris Disks with Planets. *ApJ* **588**, 110.
- Labs, D. and H. Neckel (1968). The Radiation of the Solar Photosphere from 2000 Å to 100 μm . *ZA* **69**, 1.
- Lagrange, A., D. Backman, and P. Artymowicz (2000). . *Protostars and Planets IV* (eds Mannings, V., Boss, A.P., Russell, S. S., Tucson: Univ. of Arizona Press), 639.
- Landgraf, M., J.-C. Liou, H. Zook, and E. Grun (2002). Origins of Solar System Dust beyond Jupiter. *AJ* **123**, 2857.
- Liou, J., S. Dermott, and Y. Xu (1995). The contribution of cometary dust to the zodiacal cloud. *Planetary and Space Science* **43**, 717.
- Liou, J. and H. Zook (1997). Evolution of Interplanetary Dust Particles in Mean Motion Resonances with Planets. *Icarus* **128**, 354.

- Liou, J. and H. Zook (1999). Signatures of the Giant Planets Imprinted on the Edgeworth-Kuiper Belt Dust Disk . *AJ* **118**, 580.
- Liou, J., H. Zook, and S. Dermott (1996). Kuiper Belt Dust Grains as a Source of Interplanetary Dust Particles. *Icarus* **124**, 429.
- Liou, J., H. Zook, and A. Jackson (1999). Orbital Evolution of Retrograde Interplanetary Dust Particles and Their Distribution in the Solar System. *Icarus* **141**, 13.
- Love, S. and D. Brownlee (1993). A Direct Measurement of the Terrestrial Mass Accretion Rate of Cosmic Dust. *Science* **262**, 550.
- Malhotra, R., M. Duncan, and H. Levison (2000). . *Protostars and Planets IV* (eds Mannings, V., Boss, A.P., Russell, S. S., Tucson: Univ. of Arizona Press), 1231.
- Marcy, G. (2003). Personal communication. , .
- Marcy, G., R. Butler, D. Fischer, and S. Vogt (2003). . *Scientific Frontiers in Research on Extrasolar Planets* (eds Deming & Seager) *ASP Conference Series* **294**, .
- McCaughrean, M. and C. O'Dell (1996). Direct Imaging of Circumstellar Disks in the Orion Nebula. *AJ* **111**, 1977.
- McDonnell, J., D. Ashworth, R. Flavill, W. Carey, D. Bateman, and R. Jennison (1977). The characterization of lunar surface impact erosion and solar wind sputter processes on the lunar surface. *Phil. Trans. R. Soc. Lond. A*. **285**, 303.
- McDonnell, J. and R. Flavill (1974). Sputter Erosion on the Lunar Surface: Measurements and Features Under Simulated Solar He+ Bombardment. *Lunar and Planetary Science V* (Houston: Lunar Planet. Inst.), 478.
- Morfill, G. and E. Grun (1979). The motion of charged dust particles in interplanetary space. I - The zodiacal dust cloud. II - Interstellar grains. *Planet. Space Sci.* **27**, 1269.
- Moro-Martín, A. and R. Malhotra (2002). A Study of the Dynamics of Dust from the Kuiper Belt: Spatial Distribution and Spectral Energy Distribution. *AJ* **124**, 2305.
- Moro-Martín, A. and R. Malhotra (2003). Dynamical Models of Kuiper Belt Dust in the Inner and Outer Solar System. *AJ* **125**, 2255.
- Mouillet, D., J. Larwood, J. Papaloizou, and A. Lagrange (1997). A planet on an inclined orbit as an explanation of the warp in the Beta Pictoris disc. *MNRAS* **292**, 896.

- Mukai, T. (1985). Small grains from comets. *Astron. Astrophys.* **153**, 213.
- Mukai, T. (1986). Analysis of a dirty water-ice model for cometary dust. *Astron. Astrophys.* **164**, 397.
- Mukai, T., J. Blum, A. Nakamura, R. Johnson, and Havnes (2001). . *Interplanetary Dust* (ed. E. Grün, B. Å. S. Gustafson, S. F. Dermott, & H. Fechtig (Berlin: Springer), 445.
- Mukai, T. and G. Schwehm (1981). Interaction of grains with the solar energetic particles. *Astron. Astrophys.* **95**, 373.
- Murray, N., J. Weingartner, and P. Capobianco (2003). . *astro-ph/0309805*, .
- Ozernoy, L., N. Gorkavyi, J. Mather, and T. Taidakova (2000). Signatures of Exosolar Planets in Dust Debris Disks. *ApJ* **537**, 147.
- Pantin, E., P. Lagage, and P. Artymowicz (1997). Mid-infrared images and models of the beta Pictoris dust disk. *Astron. Astrophys.* **327**, 1123.
- Parker, E. (1963). . *Interplanetary Dynamical Processes* (New York: John Wiley), 138.
- Parker, E. (1964). The Perturbation of Interplanetary Dust Grains by the Solar Wind. *ApJ* **139**, 951.
- Quillen, A. and S. Thorndike (2002). Structure in the ϵ Eridani Dusty Disk Caused by Mean Motion Resonances with a 0.3 Eccentricity Planet at Periastron. *ApJL* **578**, 149.
- Rieke, G. (2003). Personal communication. , .
- Rieke et al., G. (2004). in preparation. pp. .
- Roques, F., H. Scholl, B. Sicardy, and B. Smith (1994). Is there a planet around beta Pictoris? Perturbations of a planet on a circumstellar dust disk. 1: The numerical model. *Icarus* **108**, 37.
- Schneider, G., B. Smith, E. Becklin, D. Koerner, R. Meier, D. Hines, P. Lowrance, R. Terrile, R. Thompson, and M. Rieke (1999). NICMOS Imaging of the HR 4796A Circumstellar Disk. *ApJ* **513**, 127.
- Spangler, C., A. Sargent, M. Silverstone, E. Becklin, and B. Zuckerman (2001). Dusty Debris around Solar-Type Stars: Temporal Disk Evolution. *ApJ* **555**, 932.
- Stern, S. (1996). Signatures of collisions in the Kuiper Disk. *Astron. Astrophys.* **310**, 999.

- Taylor, A., W. Baggaley, and D. Steel (1996). Discovery of interstellar dust entering the Earth's atmosphere. *Nature* **380**, 323.
- Trujillo, C. and M. Brown (2001). The Radial Distribution of the Kuiper Belt. *ApJL* **554**, 95.
- Weidenschilling, S. (2003). Personal communication. , .
- Weinberger, A., E. Becklin, G. Schneider, B. Smith, P. Lowrance, M. Silverstone, B. Zuckerman, and R. Terrile (1999). The Circumstellar Disk of HD 141569 Imaged with NICMOS. *ApJ* **525**, 53.
- Weinberger, A., E. Becklin, and B. Zuckerman (2003). The First Spatially Resolved Mid-Infrared Spectroscopy of β Pictoris. *ApJL* **584**, 33.
- Wilner, D., M. Holman, M. Kuchner, and P. Ho (2002). Structure in the Dusty Debris around Vega. *ApJL* **569**, 115.
- Wisdom, J. and M. Holman (1991). Symplectic maps for the n-body problem. *AJ* **102**, 1528.
- Wolf, S. and L. Hillenbrand (2003). Model Spectral Energy Distributions of Circumstellar Debris Disks. I. Analytic Disk Density Distributions. *ApJ* **596**, 603.
- Wyatt, M., S. Dermott, and C. Telesco (1999). How Observations of Circumstellar Disk Asymmetries Can Reveal Hidden Planets: Pericenter Glow and Its Application to the HR 4796 Disk. *ApJ* **527**, 918.
- Wyatt, S. and F. Whipple (1950). The Poynting-Robertson effect on meteor orbits. *ApJ* **111**, 134.
- Yamamoto, S. and T. Mukai (1998). Dust production by impacts of interstellar dust on Edgeworth-Kuiper Belt objects. *Astron. Astrophys.* **329**, 785.
- Zook, H. and O. Berg (1975). A source for hyperbolic cosmic dust particles. *Space Sci.* **23**, 183.
- Zuckerman, B. (2001). Dusty Circumstellar Disks. *ARA&A* **39**, 549.